Binder Jetting and Heat Treatment of Ferrous Alloys

by

Issa Rishmawi

A thesis
presented to the University of Waterloo
in fulfillment of the
thesis requirement for the degree of
Master of Applied Science
in
Mechanical & Mechatronics Engineering

Waterloo, Ontario, Canada, 2019

© Issa Rishmawi 2019

Declaration Page

This thesis consists of material all of which I authored or co-authored: see Statement of Contributions included in the thesis. This is a true copy of the thesis, including any required final revisions, as accepted by my examiners.

I understand that my thesis may be made electronically available to the public.

Statement of Contributions

Chapter 3 of this thesis, titled, "Binder Jetting and Sintering of Fe," consists of results, figures and information that were part of a paper that was co-authored by myself, then-post-doctoral fellow Dr. Mehrnaz Salarian, and my advisor Dr. Mihaela Vlasea. Dr. Merhnaz Salarian developed, implemented and documented the method for CT imaging and analysis, as well as discussions on debinding. I developed, implemented and documented the methods and results for the rest of the paper. Dr. Mihaela Vlasea provided valuable insight and recommendations as my direct supervisor. The paper is cited in Chapter 1 and referenced in the References.

Abstract

Binder Jetting (BJ) is a manufacturing process that involves iterative and layer-wise deposition of powder material and an adhesive binder to construct geometrical features. It can be used to construct freeform and complex objects out of metal or ceramic powders. Printed BJ products typically must undergo sintering at high temperatures to fuse together the powder particles and create a dense structure. BJ is a relatively new technology that requires more research and development to promote its adoption into the industrial space. It is attractive because of its comparatively low cost yet high customizability and scalability. This is especially the case for metal part production.

In this thesis, process development was undertaken for BJ and heat treatment of ferrous metal powders. Iron (Fe) and silicon-iron (Fe-Si) powders were studied as materials of interest. The goals of this work were to establish process maps for BJ and sintering to achieve respectively high densities, as well as to better understand the significance of the relevant parameters. In the BJ process, studies to tailor the parameters and then to optimize for green density were conducted. The effect of powder morphology was discussed. Statistical significance of parameters and their interactions was noted. Regression analysis formed the basis of the optimization. Expressions for green density and powder packing behavior were derived in terms of the parameters. Green densities of 49.7% were achieved for the irregular Fe powder and 71.3% for the spherical Fe-Si powder.

Beyond green density optimization, the importance of debinding temperature and duration was explored. Sintering was investigated in two different modes: in the solid state for Fe and in the liquid phase for Fe-Si. Sintered densities of 91.3% were achieved for Fe and 94.7% for Fe-Si. For the Fe dataset, it was found that sintering at high temperatures diminished local variability in green density. Observations of sinter necks and the density values indicated that sintering occurred in the intermediate-final stages. For the Fe-Si dataset, rapid densification was achieved within minutes of reaching the liquid phase. The influence of sintering hold duration was found to be small, which is consistent with the theoretical understanding. Sinter necks were observed to be in the form of a Si-rich liquid and appeared well-progressed. The Si segregation phenomenon seemed to be amplified by temperature and more importantly by the presence of surface oxides. The work done on BJ

and sintering of Fe and Fe-Si forms the basis for further studies on densification. Master Sinter Curves (MSCs) and Master Sinter Surfaces (MSSs) are planned as future work that will increase the utility of BJ in industrial applications to produce high and predictable densities.

Acknowledgements

First and foremost, I am indebted to my advisor, Dr. Mihaela Vlasea, for her continuous guidance throughout my degree. Mihaela, it has been a great pleasure to work under your supervision. Thank you for all the technical advice and the professional guidance, and for providing a supportive environment for growth. You have been a fantastic mentor in all respects. In the past two years, I feel that I have gained more experience, skills and knowledge than I had imagined I would when I started my degree. At the backbone of all of that was your constant encouragement.

I have many people to thank at the Multi-Scale Additive Manufacturing laboratory. Dr. Allan Rogalsky has given me valuable suggestions on experimental design, statistical analysis and thermal analysis. I am grateful for the help and friendship of Dr. Mehrnaz Salarian. Her help with CT images and discussions on debinding were valued. Dr. Ehsan Marzbanrad trained me to run DSC-TG measurements and kindly offered to sit with me while I ran my first few sintering trials. I also want to thank Dr. Hamed Asgari, Henry Ma, Pablo Enrique, Brian Jeong and Chia-Pei Wang for their help and kind advice. Our lab technicians, Jerry, Karl and Grace, were amazingly helpful with equipment maintenance and kept a cheerful atmosphere in the lab.

The many friends and lab mates in East Campus 4 made my Master's journey a bright and light-hearted experience. I am glad to have had Brian as a friend and a close lab mate. Our many conversations and coffee trips were always refreshing. Larry, thanks for all the lunch conversations and also for dragging me to join the music and dance clubs on campus. I am thankful for all my other friends and lab mates at EC4. Above all else, I am forever grateful to my family for their continued love and encouragement. Thank you for putting up with me spending many weekends away at the lab or attached to my computer. Your support has been monumental.

Dedication

To my parents, Nassim and Rita,
whose unchanging, endless support knows no bounds.

Table of Contents

List of Tables xi

List of Figures xiii

1 Introduction 1

1.1 Motivation . . . 2

1.2 Objectives . . . 3

1.3 Thesis Structure . . . 3

2 Background & Literature Review 5

2.1 Introduction to Binder Jetting . . . 5

2.2 Review of Binder Jetting Process Development . . . 11

2.2.1 Studies on Pre-process Parameters . . . 12

2.2.2 Studies on Process Parameters . . . 14

2.2.3 Studies on Post-process Parameters . . . 17

2.3 Sintering Theory . . . 20

2.3.1 Solid State Sintering . . . 20

2.3.2 Liquid Phase Sintering . . . 23

2.4 Master Sinter Curves 28
2.4.1 The Master Sinter Curve Concept 28
2.4.2 Linearization of the Master Sinter Curve 30
2.4.3 Master Sinter Curve for Liquid Phase Sintering 32
2.4.4 Master Sinter Surfaces 33

3 Binder Jetting and Sintering of Fe **35**
3.1 Motivation 35
3.2 Experimental Methods 36
3.2.1 Material System 36
3.2.2 Green Sample Fabrication 37
3.2.3 Density Estimations 38
3.2.4 Debinding and Sintering 39
3.3 Results 41
3.3.1 Metal Powder Characteristics 41
3.3.2 Effects of Process Parameters on Green Density 42
3.3.3 Debinding Analysis 48
3.3.4 Solid State Sintering 51
3.4 Summary and Outcomes 62

4 Binder Jetting and Sintering of Fe-Si **64**
4.1 Motivation 64
4.2 Experimental Methods 65
4.2.1 Metal Powder Material 65
4.2.2 Green Density Optimization Experimental Design 65

4.2.3 CT Analytics for Green Samples . . . 68
4.2.4 Microscopy Analysis for Sintered Samples . . . 69
4.2.5 Debinding . . . 70
4.2.6 Sintering . . . 71
4.2.7 Dilatometry and the MSC . . . 74
4.3 Results . . . 75
4.3.1 Metal Powder Characteristics . . . 75
4.3.2 Green Density Optimization . . . 76
4.3.3 Debinding Analysis and Debinding of the Final Samples . . . 82
4.3.4 Liquid Phase Sintering . . . 84
4.4 Summary and Outcomes . . . 94

5 Conclusions & Future Directions **97**
5.1 Green Density Optimization . . . 97
5.2 Debinding and Sintering . . . 98

References **100**

APPENDICES **112**

A Table of Parameters **113**

B Green Sample Analytics **115**

C Sintered Sample Images **124**

List of Tables

3.1 The process parameters used for the Fe study. 38

3.2 Green densities obtained for the various builds for Fe. 44

3.3 Debinding duration requirement for different samples; the differences indicated effects of process parameters on debinding duration. 50

3.4 Sintered density values of the sample with the highest green density (sample A), under the various sintering conditions; 1390°C corresponds to 90% of the powder melting point and 1490°C corresponds to 97%. 51

4.1 Half-factorial with two center points design of experiments for optimization. The process parameter values are displayed in parentheses. 67

4.2 Liquid phase sintering schedules, showing sintering temperatures, isotherm durations, heating rates and atmospheres used. Two isotherm durations were studied: 15 min and 1 hour. 73

4.3 Dilatometry schedule for liquid phase sintering of the Fe-Si samples. 74

4.4 Green densities obtained for the different builds for Fe-Si. 76

4.5 Density values of sintered samples from build 7 at two different isotherm durations. 84

B.1 ANOVA table for the effects of process parameters on green density; L: layer thickness; B: binder volume; C: compaction. 115

B.2 OLS regression table for the process parameters and green density values; L: layer thickness; B: binder volume; C: compaction. 116

B.3 ANOVA table for the effects of process parameters on green density; l: normalized layer thickness; v: spreading speed; w: compaction speed; s: binder saturation. 120

B.4 OLS regression table for the process parameters and green density values; l: normalized layer thickness; v: spreading speed; w: compaction speed; s: binder saturation. 121

List of Figures

2.1 An illustration of a typical BJ manufacturing process, showing the main steps: (1) the build bed lowers through piston mechanism, (2) a fresh layer of powder is deposited through a powder recoater, (3) the powder layer is uniformly spread and compacted through a counter-rotating roller, and (4) the binder is jetted through a printhead to produce the geometry. 6

2.2 Example of a green part produced using BJ. 7

2.3 The different sintering stages, showing the progression of sinter neck formation; adapted from [1]. 22

2.4 Schematic of three particles in contact and various mass transport mechanisms that drive necking in solid state sintering; adapted from [2]. 23

2.5 An illustration of two particles undergoing LPS, showing the geometry used to calculate the capillary force; adapted from [3]. 24

2.6 Illustration of wetting behavior of a liquid against a solid, relevant to liquid phase sintering. Smaller contact angles improve densification as grains are pulled together well; adapted from [3]. 25

2.7 Illustration of supersolidus LPS in a pre-alloyed powder; adapted from German [4]. (a) Initial packed powder particles, (b) start of liquid formation with insufficient grain boundary wetting for densification, (c) and (d) continued densification into the final stage with pores closing. 27

2.8 Examples of MSCs for (left) alumina [5] and (right) a tungsten-heavy alloy [6]. 31

2.9 Example of a master sinter curve for liquid phase sintering for 316L stainless steel; adapted from [7]. The onset of the liquid phase is evident in the steep slope of the curve. 33

2.10 Example of a sinter surface that expresses densification behavior against time-temperature and pressure profiles; adapted from [8]. 34

3.1 CT images of green and sintered samples were captured and reconstructed for analysis. This visual illustrates the (left) green and (right) sintered sample A in a 3D visualization. 40

3.2 SEM images of the Fe powder showing irregular particle morphology at a magnification 200×. 42

3.3 CT images were segmented for density calculation; (left) unsegmented and (right) segmented images in the xy plane of sample A in the green state. . 43

3.4 Plots of green density against (left) layer thickness and (right) binder volume. 45

3.5 An appropriate debinding temperature was determined based on the mass loss curve of the sold-liquid binder mixture used in the Fe study. 49

3.6 Effect of process parameters on debinding; the curves show sample mass loss against (left) temperature and (right) time, due to debinding starting from ambient temperature until the end of the 300°C isotherm. 50

3.7 Sinter neck formation and different stages of sintering for the different conditions: (a) 1390°C, 2 hours; (b) 1390°C, 6 hours; (c) 1490°C, 2 hours; (d) 1490°C, 6 hours. 53

3.8 (a) Comparison of relative density profiles along sample height across green and sintered (1490°C, 6 hours) sample A; (b) minimum intensity projection of the CT scan showing pore distribution for the green and (c) sintered sample; (d) a region of interest (ROI) 2 mm in length; (e) minimum intensity projection of the ROI for the green and (f) sintered sample. 55

3.9 Relative density profile comparison across sintering schedules (average density value shown in dotted lines). 57

3.10 Histograms of pore count against (a) pore volume, and (b) pore sphericity for green and sintered (91.3% density), evaluated via CT image processing. Pore volumes greater than 1×10^{11} μm^3 indicated an interconnected pore network that was detected only in the green sample. 58

3.11 Three-dimensional rendering of μCT scans of sintered sample A (1490°C, 6 h) showing the distributions of (a) pore volume and (b) pore sphericity. . . 59

3.12 Dimensional shrinkage due to sintering. Sample A in (a) green state, and sintered at (b) 1390°C, 2 hours, (c) 1390°C, 6 hours, (d) 1490°C, 2 hours and (e) 1490°C, 6 hours. The extent of dimensional shrinkage correlated with density. 60

3.13 Shrinkage due to sintering with respect to (a) temperature, (b) duration and (c) density for sample A. 61

4.1 A reduced-size build volume insert was used in the ExOne system during green sample production. The insert was used only to reduce powder consumption and did not affect the build quality or sequence. 68

4.2 Phase diagram of the Fe-Si alloy [9]. 71

4.3 DSC and DDSC curves for the Fe-Si BJ sample; the melting signature was used to determine the appropriate temperature for liquid phase sintering. . 72

4.4 SEM image of the Fe-Si powder at 200× magnification, showing its generally spherical particle shape. 75

4.5 Segmentation of CT images density calculation; (left) unsegmented and (right) segmented images in the xy plane of sample 7 as a green sample. . . 77

4.6 Green density behavior with respect to (left) normalized layer thickness and binder saturation, and (right) spreading and compaction speeds. 78

4.7 TG curve of the ExOne binder showed an acceptable debinding temperature of 400°C. 83

4.8 TG curve showing the debinding profile of Fe-Si (build 7) printed with the ExOne binder. 83

4.9 Debound samples in preparation for sintering. 84

4.10 Laser confocal microscopy images of the sintered samples. 85

4.11 Optical and laser confocal images of sectioned samples sintered for 15 min and 1 hour; by using laser height mapping, pores could be clearly differentiated from the solid darker regions. Examples of sinter necks are annotated where it appeared liquid formation occurred and connected particles together. 87

4.12 Scanning electron microscopy images of the sintered samples, showing sinter necks formed in the alloy matrix. A curvature in the regions of sinter necks is visible, which was indicative of sintered powder particles. 88

4.13 Energy dispersive spectroscopy results for the sintered samples. The analysis showed that a Si-rich constituent separated from the main Fe matrix upon liquid phase sintering. 89

4.14 Schematic of the hypothesized diffusion of Si during sintering: (a) at high temperatures below the peak, solid state sinter necks slowly began to form; (b) at the peak temperature, Si diffused out of the particles; O was present on the surface of particles due to surface oxidation; (c) Si formed sinter necks in the liquid phase; (d) sinter necks grew wider and the larger Fe matrix softened, deformed and connected. 90

4.15 Laser confocal microscopy and scanning electron microscopy of the sample sintered at 1482°C. The sample did not experience shape distortion and the micrographs show progression of liquid phase sintering. A higher abundance of the darker Si region was observed, which could indicate that Si segregation could be amplified by temperature. 92

4.16 Laser confocal microscopy and energy dispersive spectroscopy images of an outlier sample sintered at 1470°C. The sample showed severe Si segregation, which was most likely caused by excessive oxidation before sintering. . . . 94

B.1 Residuals plot of the regression model for Fe. 117

B.2 Q-Q plot of the regression model for Fe. 117

B.3 Individual plots of green density against printing parameters for Fe-Si. . . 118
B.4 Density profiles in the z-direction of green samples from various builds for Fe-Si. 119
B.5 Residuals plot of the regression model for Fe-Si. 122
B.6 Q-Q plot of the regression model for Fe-Si. 122

C.1 SEM images of Fe sample A, taken at the sample surface, sintered at 1390°C for 2 hours. 125
C.2 SEM images of Fe sample A, taken at the sample surface, sintered at 1390°C for 6 hours. 125
C.3 SEM images of Fe sample A, taken at the sample surface, sintered at 1490°C for 2 hours. 126
C.4 SEM images of Fe sample A, taken at the sample surface, sintered at 1490°C for 6 hours. 126
C.5 LCM images of a Fe-Si sample from build 7, sintered at 1470°C for 15 minutes. 128
C.6 LCM images of a Fe-Si sample from build 7, sintered at 1470°C for 1 hour. 128
C.7 LCM images of a Fe-Si sample from build 7, sintered at 1482°C for 1 hour. 129
C.8 LCM images of a Fe-Si "anomaly" sample with severe Si segregation, sintered at 1470°C for 1 hour. 129
C.9 CT images in the xy plane of the Fe-Si "anomaly" sample from build 7 before and after sintering; the sintered sample showed severe Si segregation. 131
C.10 CT images in the xy plane of the Fe-Si "anomaly" sintered sample from build 7, showing various slices from the reconstructed volume. 132
C.11 CT images in the xy plane of the Fe-Si "anomaly" sample from build 7 with image segmentation to corresponding to the three intensity peaks: the Fe segment, the Si segment and the pores segment. Later analysis revealed inaccuracies in the Si and pores intensity peaks. 133

C.12 SEM images of a Fe-Si sample from build 7, sintered at 1470°C for 15 minutes. 135
C.13 SEM images of a Fe-Si sample from build 7, sintered at 1470°C for 1 hour. 135
C.14 SEM images of a Fe-Si sample from build 7, sintered at 1482°C for 1 hour. 136
C.15 SEM images of a Fe-Si "anomaly" sample with severe Si segregation, sintered at 1470°C for 1 hour. 136

Chapter 1

Introduction

Additive Manufacturing (AM) recently emerged as a new class of manufacturing technology. It is still widely in the research and development phase, yet it is beginning to see increased industrial adoption. As the name suggests, AM relies on producing a component by adding material in small increments, only as needed. It is a "freeform" technology that does not require molds or dies. Not only does it make manufacturing less wasteful, it is also arguably a more intuitive means to produce components. Today, many manufacturers of AM machines exist, targeting both the industrial space and the consumer market.

Fundamentally, all types of AM rely on layer-wise deposition of a powdered, extrudable or liquid material to build components. The fusion mechanism can vary immensely: from photo-curable polymers and thermally curable binders to lasers and electron beams. Many of its applications thus far have been structural and mechanically loaded components. There are also many examples in literature and in company portfolios of AM products with different functional properties. The functional properties can be thermal, electrical, chemical or biomedical. In principle, electronic, nano-structural or even biological properties can also be targeted – although AM will have to undergo significant refinement and process control to tackle these latter examples. One of the benefits of adopting AM is gaining more freedom in functional design of products. Another is the capacity to reduce product weight or cost.

The target of this thesis is one type of AM technology known as Binder Jetting (BJ).

In this technology, a binder is selectively added onto a bed of powdered material. The binder is most commonly in an aqueous form, hence the use of a nozzle to jet it onto the powder material. This results in a geometrically accurate printed component. However, binders are usually mechanically weak and not otherwise functional. The printed or "green" components are additionally very porous. For this reason, the components are usually heat-treated at elevated temperatures to fuse and densify the powder in a process known as "sintering." Sintering is an already existing process that has been employed in manufacturing for many years. Process development for BJ therefore entails both the printing and the heat treatment of the component.

1.1 Motivation

Generally, process development for BJ is not a well-established procedure. The main reason is that interest in BJ only recently started to increase. BJ machine manufacturers started to enable the production of complex components for a comparatively low cost. Targeting metal components also helped to garner interest, as other dominant AM technologies for metals such as laser or electron beam processes are more expensive.

BJ involves a large number of process variables. Overall, the interaction of the variables is not well understood, most likely due to the lack of fundamental physics models that capture the powder and powder-binder interactions. Sintering, by contrast, is more well-understood and supported by years of adoption in the manufacturing community. However, sintering characteristics are heavily dependent on the powder and green part characteristics. The sintering characteristics can be difficult to predict in some cases. The primary drawbacks of BJ are the high porosity found in printed components and the difficulty in achieving fully dense components after sintering. These are perhaps the major obstacles that have slowed down BJ adoption.

This thesis aims to contribute to BJ process development for metals by tackling challenges in both printing and heat treatment. The purpose is to achieve comparatively high green densities, as well as high densities after sintering. The work lays the foundation for future measurements of sample densification in response to temperature and time. This

will culminate in an empirical model that can be thought of as the end point in the process development. However, development of the model is beyond the scope of the thesis. The specific target is ferrous metal powders such as pure iron (Fe) and silicon-iron (Fe-Si). Both materials make this work relevant to the industrial adoption of BJ, since Fe and Fe-Si are directly used in soft magnetic applications.

1.2 Objectives

The focus of this thesis is on developing a work flow for printing and heat treatment of ferrous metal powders for BJ. The objectives can be summarized as follows:

1. Establish BJ process maps for Fe and Fe-Si to print green samples with high densities;
2. Optimize key BJ process parameters to maximize green densities and to better understand process parameter behavior; and
3. Establish heat treatment schedules that produce high final densities, and further the understanding of solid state and liquid phase sintering in BJ.

1.3 Thesis Structure

The thesis is comprised of five chapters. This first chapter is the introductory chapter. Chapter 2 is concerned with providing background information and literature review relevant to the discussion in subsequent chapters. Specific emphasis is placed on BJ process parameters, existing optimization efforts and the impact of the parameters on green density. The theoretical groundwork for sintering is presented as well as relevant information on sintering and densification of BJ parts. The thesis is centered on two studies that individually explored BJ and heat treatment. Chapter 3 is the study of BJ of commercially pure Fe powder and tailoring of process parameters, binder removal and sintering parameters. This chapter contains results and figures that were published in the Journal of Additive Manufacturing in October of 2018 [10]. Chapter 4 is the study of BJ of Fe-Si powder and

involves optimization of four key process parameters to maximize green density. Empirical expressions for green density and powder packing are derived based on regression analysis. The chapter is also concerned with sintering of the Fe-Si samples, which progresses in a different sintering mode than that of the Fe powder because of its alloyed nature. Chapter 5 is the final chapter that summarizes the thesis, its conclusions and future steps.

Chapter 2

Background & Literature Review

2.1 Introduction to Binder Jetting

In 1993, a group of pioneering researchers from the Massachusetts Institute of Technology (MIT) invented a technique to selectively jet a binding liquid onto successive layers of powder to produce a part geometry [11]. The technique was originally known as "three-dimensional printing (3DP)" before the term became associated with all AM technologies. The technique was licensed to the ExOne Company – then known as the Extrude Hone Corporation – in 1996 to produce sand molds, cores and eventually direct metal parts and tooling [12]. Today, the technique is known as Binder Jetting, and is being used by companies and researchers.

BJ is one of the seven main types of AM technologies. The process involves layer-wise fabrication of a three-dimensional (3D) part by binding together loose powder in the desired geometry. The fabrication procedure starts with a computer-aided design (CAD) of the part to be fabricated. The digital design geometry is horizontally discretized into thin "slices" that are typically 30-200 μm in thickness. Each slice constitutes a "layer" in the manufacturing process. Most commercial BJ machines use their own slicing software.

A typical fabrication cycle in the machine is usually comprised of four steps: (1) the powder build bed lowers through a piston mechanism, (2) on the flat bed of powder, a

fresh layer of powder is deposited through a powder recoater, (3) the powder layer is uniformly spread and compacted through a counter-rotating roller, and (4) the printhead jets a binder onto the powder layer, where the binder permeates into the powder and forms the geometry; and then the cycle repeats until the part is complete. In many machines, heat is applied to the jetted surface to dry the binder and assist in layer adhesion. Strictly speaking, the drying step is not always necessary, depending on the binder material and the printhead. A pictorial representation of a BJ process is shown in Figure 2.1.

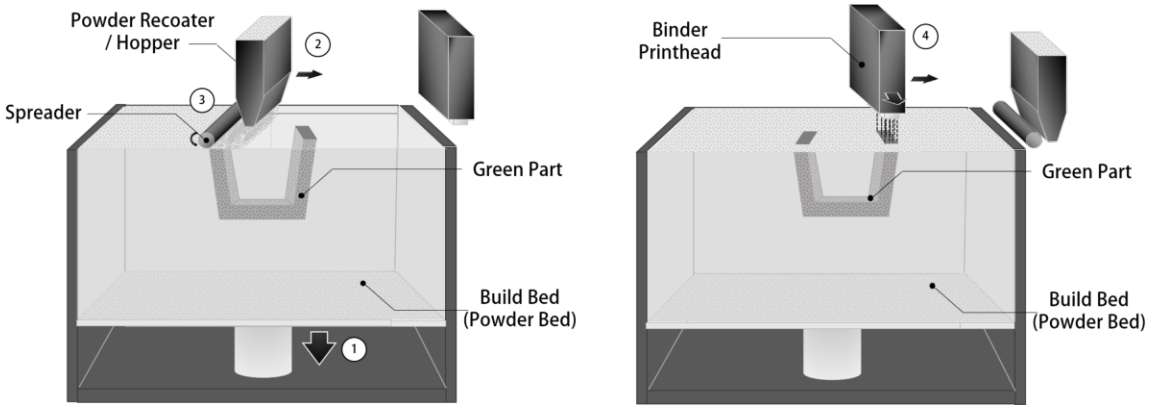


Figure 2.1: An illustration of a typical BJ manufacturing process, showing the main steps: (1) the build bed lowers through piston mechanism, (2) a fresh layer of powder is deposited through a powder recoater, (3) the powder layer is uniformly spread and compacted through a counter-rotating roller, and (4) the binder is jetted through a printhead to produce the geometry.

There are variations in the above steps across different BJ machines. The method of powder deposition is one such variation. While some machines rely on a hopper to dose powder on top of the build bed, others rely on a piston feed mechanism to supply powder, which is then spread from the feed bed to the build bed. Some machines spread powder in only one direction every layer, whereas others spread in both directions to increase manufacturing speed. The size range of the powder used also varies among machines from below 10 μm to above 150 μm, depending on the target application. Another variation is the type of binder used, where depending on the chemistry and physical properties, different requirements for curing are imposed. Some BJ machines use aqueous or organic



Figure 2.2: Example of a green part produced using BJ.

binders, and some solid binders may be used in the powder bed itself to add to the binding strength of the liquid binder [13]. There have also been efforts to use binders made of the same material as the powder, which can be advantageous for part density [14].

When a part is fabricated and removed from the machine, it is in a so-called "green" state. Figure 2.2 shows a standard green part produced using BJ. The term "green part" has been used in Powder Metallurgy (PM) to describe porous powder compacts long before the invention of BJ. The technical definition for green part density in the context of BJ is "the ratio of metal powder volume to the external volume of the printed part, and is a measure of how tightly packed the powder particles in the printed part are" [15]. The green part is in essence loose powder bound together in a specific geometry. As such, it is quite porous and mechanically weak. The part needs to be debound of the binder and subsequently sintered at a high temperature to densify. Sintering is the process of heating a part to above a critical temperature so that powder particles fuse together and the part densifies. Sintering is therefore the post-processing step in which many of the functional properties of a component are usually achieved.

Advantages of Binder Jetting Technologies

There are different advantages and drawbacks to BJ that shape its end applications. The first advantage is that it is inherently a low-cost process in comparison to other AM technologies in the context of high quality metal part production, specifically in contrast to laser and electron beam processes. This is true for a number of reasons. First, the process does not require high temperatures or special atmospheres to run, which reduces operation cost. If the print cycle were optimized for speed, it can lead to fast production of parts without sacrificing part quality. Parts can be stacked vertically in the build chamber without requiring gravity support structures, thereby increasing the number of parts produced in one build. In addition, debinding and sintering of parts can be batched (as is routinely done in PM), driving the cost per part even lower. Further, the process is scalable in production; once a manufacturing cycle is optimized for a material or a part, it becomes easier to produce a larger number of parts for low-to-medium volume production demands. Finally, maintenance of machines and consumables can be in principle more cost-effective.

The second advantage is its applicability to a very wide range of materials. Most materials can be bound together by using an adhesive. Rarely, chemical compatibility between the binder and the powder may arise, but this can be resolved by using a more compatible binder. Metal, ceramic and polymer parts have been fabricated with this process. Specific examples are provided later in this chapter.

BJ parts experience lower residual stresses during manufacturing compared to laser metal AM processes. The BJ process itself requires minimal heat input, while the sintering process is typically conducted in an environment with uniform heat distribution. In addition, careful control of the sintering process can in principle allow precise control over microstructure.

In terms of design, BJ offers good design freedom as an advantage. There is a much smaller need for support structures during manufacturing than with laser processes. Structures with overhangs, sharp angles or thin features in principle experience minimal distortion during manufacturing – although improper selection of powder spreading parameters may lead to part distortion [16]. By contrast, sintering may cause warping of thin or unsupported features, which is usually overcome by surrounding the part with support material

such as ceramic powder during sintering [17]. Design for BJ (or for AM in general) is a new topic that still requires tremendous efforts to standardize.

Another advantage is the capacity to spatially control porosity in a part. This may be accomplished by varying the amount of binder in the part during fabrication, using multi-modal powder sizes, varying print layer orientations or introducing sacrificial materials [18]. This makes BJ ideal for biomedical applications, where intentionally porous and customized parts are desired.

Drawbacks of Binder Jetting Technologies

The process suffers from three main drawbacks. Primarily, it is not very common to fabricate fully dense parts with BJ, even after sintering. Typical final densities range between around 60% and 95%, with recent advances approaching full density by maximizing green part density and optimizing the sintering process [19, 20, 21]. Recently, the ExOne Company started producing fully dense parts through completely unaided sintering. Achieving target densities of 90-95% makes BJ immediately applicable in the automotive industry, which often deploys PM to fabricate parts of this density range.

Second, the requirement for intensive post-processing is in itself a drawback, particularly in comparison to laser AM processes that produce near net-shape parts directly in the build bed. In terms of the BJ process work flow, thermal post-processing usually comprises a significant portion of the science, time and resources needed to produce fully functional parts with the desired geometrical, structural and mechanical properties. The added requirement for having furnaces for sintering is an important consideration, particularly on an industrial scale.

The final disadvantage is poor surface quality [22, 23]. Green parts generally have a surface roughness comparable to the powder material itself (depending on the particle size range and layer thickness range deployed in the process). This is unlike PM compacts, where the compaction force and the use of lubricants can produce smooth green parts with machined-like surfaces. Upon sintering, the surface quality of a BJ part typically improves, but remains much rougher than machined surface quality, often being above 10

μm. Depending on the target application, filing, grinding or polishing are needed to obtain smoother surfaces.

Overall, BJ is a promising technology. Its potentials can be deployed to impart advantages to new products. An example of this is leveraging design complexity and low cost for low-volume production of parts, for instance for automotive applications [24]. Interest in BJ has been slow mainly due to its drawback of low part densities. As higher densities became more commonly achievable, BJ machine manufacturers started to incentivize the low cost advantage.

Applications of Binder Jetting Technologies

There are many industrial applications for which BJ can be used, with notable examples below. Ferrous (Fe) alloys such as steels were studied in BJ for various applications, including: hot forging dies [25], injection molding tooling [26, 27] and sound waveguides [28]. Other researchers such as Lu et al. [29] demonstrated printing of Ti-Ni-Hf shape memory alloys, while Mostafaei et al. [30] fabricated and sintered Ni-Mn-Ga shape memory alloy parts. Fabrication and sintering of Inconel 718 for aerospace applications were also demonstrated [31]. Snelling et al. [32] successfully printed digital molds for casting metal cellular structures for jet engine applications. Azhari et al. [33] demonstrated the fabrication of graphene-based supercapacitor electrodes for electrochemical applications, where the porous structure helped the transport of ions.

There are many examples of biomedical applications as well. The use of porous scaffold materials is preferred in biomedical applications. This includes materials that provide a good opportunity for cellular adhesion and fluid media transfer through the BJ structures [34, 35]. Another example is the work by Lam et al. [36], where the group printed biocompatible scaffolds by using a starch-based polymer. The fabrication of porous, complex bio-scaffolds is a useful achievement in tissue engineering. Hong et al. [37] printed and sintered biodegradable Fe-Mn-Ca/Mg alloys and demonstrated the successful use of the porous parts *in vitro* with desirable degradation rates and good cyto-compatibility. In addition, Liravi & Vlasea [38] demonstrated printing of complex silicon (polysiloxane) parts that might be used for prosthetic devices. Furthermore, BJ has found applications in drug

delivery and pharmaceutical engineering [39]. The use of a liquid binder, varied binder content and sacrificial materials can be advantageous in drug delivery. The use of Fe alloys in BJ in biomedical applications include examples such as: craniofacial bone implants [40], metal-ceramic-matrix materials [41] and hip and knee implants [42].

In much of the literature, BJ was used to demonstrate successful part fabrication for a variety of applications, or as demonstrators in advancing the material science and scope of material adoption in BJ. Some examples of new material adoption and process development include: titanium [43, 44, 45, 46, 47, 48], nickel [19, 20, 49], copper [50, 51], lead [52, 53], zirconium [54], zinc [55], gold [56] magnetic Nd-Fe-B materials [57] and composite metal materials [41, 58, 59, 60]. These examples illustrate the applicability of BJ to many metals, and its prospective impact on metal manufacturing.

2.2 Review of Binder Jetting Process Development

The quality of a BJ part depends on many different parameters. In this work, the parameters are categorized as pre-process, in-process and post-process parameters. The pre-process parameters are such that they cannot be dynamically changed, and are typically fixed at the start of the BJ AM sequence. Examples of pre-process parameters include but are not limited to: powder particle size, morphology, tap density and binder viscosity. In-process or "process" parameters are those that can be changed in the BJ process itself. For a given a set of pre-process parameters, changing the process parameters can impart a range of green part densities, structural properties and mechanical characteristics. Process parameters include but are not limited to: powder spreading parameters, layer thickness, binder amount and part orientation. Post-process parameters relate to the thermal or surface treatment of the green parts. They include but are not limited to: debinding profile, sintering temperature, time schedule and atmosphere. A more complete list of all parameters is presented in Appendix A. This section describes the important parameters, with an emphasis on those that will be tackled in later chapters in this thesis. This section also presents a review of recent efforts to optimize the parameters for target properties such as density or surface finish.

2.2.1 Studies on Pre-process Parameters

The characteristics of the powder material influence green and sintered part quality to a large degree. The morphology of the particles influences powder flow, spreading and compaction behavior in the build bed. Generally, two types of powder morphologies are deployed: spherical and irregular. In the context of metals, spherical powders are generally produced by using gas or plasma atomization [61]. Conversely, irregular powders are generally produced through water atomization [61]. Some manufacturers post-process their atomized powders to vary their properties or composition, for instance through annealing or spray-drying. Chemical reduction is used in special cases as an alternative to atomization. Powders made via chemical synthesis can be either spherical or irregular, and can exhibit special spreading and compaction behavior. Spherical powders are known to produce good powder packing [61] and hence higher green densities, although irregular powders were shown to produce reasonable densities [20].

Powder size distribution (PSD) is also an important characteristic. Narrower PSDs typically result in better powder packing and hence higher green part densities [61] because of a more efficient arrangement of particles during the powder spreading process onto the build bed. A smaller mean particle size was found to improve powder packing [62], particularly if the PSD curve were skewed at the tail toward the fine sizes. The powder morphology and PSD together inform powder flow, compressibility and tap density. Tap density is the ratio of a mass of powder to the volume it occupies after tapping. These characteristics all influence powder spreading and compaction behavior in the build bed.

While most powders are comprised of a single PSD, there are benefits to using multi-modal PSDs, in which finer particles can fill the gaps between coarser particles. Bai et al. [63] investigated the effects of a bi-modal PSD on powder packing and sintering of copper. The finer particles in the bi-modal powder fill the voids among larger particles, thereby reducing the pore fraction, improving powder packing and theoretically assisting sinter bonding. With a bi-modal PSD, Bai was able to increase green part density by up to 9.4% and sintered part density by up to 12.3%. Sensitivity to sintering conditions was reduced, which is a good effect because it relaxes conditions on sintering. Density was not always increased, however, as a large difference in the PSDs hindered sinter bonding [63].

Gregorski [15] used bi-modal PSDs to produce elevated tap densities of 76-79%, and tried to understand the stresses applied on the powder during spreading to design a new spreading mechanism. For typical PSDs in AM, the main obstacles to efficient packing are inter-particle friction and mechanical interlocking in the part itself due to geometrical features [15]. Frictional and interlocking forces increase with packing density, since both relate to the number of existing inter-particle contact points – also referred to as the "coordination number." Maximizing packing density while maintaining good powder flow to ensure a consistent layer spread therefore becomes increasingly more difficult [15].

Extending the mulit-modal PSD idea even further, some efforts have targeted incorporating nanoparticles in the PSD to improve densification. Bailey et al. [51] added copper nanoparticles to stainless steel powder as a sintering aid, which is commonly done in PM. It was found that while the nanoparticles caused increased porosity or "foaming" during part curing, their addition improved densification during sintering. It was hypothesized that nanoparticles blocked the path of escaping binder vapor as it cured. Such a limitation could be improved by tailoring the concentration of nanoparticles in the binder solution.

Another important factor is the binder itself. The adhesion strength of the binder influences the mechanical strength of the green part, whereas the binder viscosity influences its permeability into the powder. In most BJ systems, the binder is a polymer solution; this has been repeatedly demonstrated to work well by companies like ExOne and by many researchers. There is growing interest in creating custom binders specifically tailored to the material and application. Historically, there was an interest in creating chemically reactive binders [64], albeit with limited success. The aims of chemically reactive binders were to ensure particle adhesion by creating a chemical reaction in the powder bed upon contact with the liquid binder, and to improve dimensional accuracy. Other researchers such as Bai & Williams [14] explored the use of a metal-organic-decomposition (MOD) ink for metal parts. They demonstrated the use of a copper MOD ink to print copper parts with a high core density. The parts had a poor shell density, which was attributed to poor binding at the surface of the parts. Future directions in binder development may see an emphasis on tailored binders such as metal suspension binders for metal parts to improve part density and perhaps even reduce the required post-processing.

Some researchers have explored the use of particle coatings to improve inter-particle

binding. This can be either in the green state or during sintering. Although tested with pressed parts instead of BJ parts, Du et al. [65] showed that an amorphous coating produced via a Pechini-type sol-gel process increased sintering densification and compressive strength. The amorphous material was understood to have higher surface energy than that of the base particles, thereby improving sinter bonding.

Studies aimed at tailoring pre-process parameters generally targeted an increase in green density or green strength. Powder chemistry, morphology and particle size range are some of the most influential parameters in the BJ process and have been scientifically studied for various material systems. In an industrial context, changing the powder characteristics to improve the process outcome could be challenging, depending on the cost factors involved. With a fixed set of powder and binder characteristics, the challenge then becomes tailoring the BJ process itself to improve green part characteristics, which is the focus of the following section.

2.2.2 Studies on Process Parameters

Due to the large number of controllable parameters, efforts to optimize the process usually focus on a few parameters at once or for a specific product quality. Several examples of optimization or process tuning exist in the literature. This section reviews studies that revealed important information about the process parameters, irrespective of whether metal or ceramic powder was used.

One of the important parameters in BJ is layer thickness. This has been demonstrated by several studies. Asadi-Eydivand et al. [66] found that layer thickness was an important factor in predicting part porosity in a study targeted toward calcium sulfate prototypes. Doyle et al. [67] found that layer thickness had a significant influence on the tensile strength of steel parts. Hsu & Lai [68] optimized the process parameters for dimensional accuracy for a proprietary ceramic powder. The study found that smaller layer thickness improved dimensional accuracy. Atre et al. [69] also found that lower layer thickness improved part density. Gonzalez et al. [21] similarly found that higher densities were possible after sintering by minimizing layer thickness and using a multi-modal PSD. Chen & Zhao [70] used a Taguchi approach to optimize the process for two objective functions: part surface

roughness and dimensional accuracy; the study found that a medium-low layer thickness resulted in better surface finish and dimensional accuracy. Generally, reducing the layer thickness within specific ranges is beneficial in increasing the green part density.

The amount of binder jetted into a green part also influences both green part density and shape fidelity. A common description of the binder amount is "saturation." The most common definition of saturation S is the ratio of binder volume V_{binder} to the volume of pores V_{pores} in a given part, as expressed in Equation 2.1.

$$S = \frac{V_{binder}}{V_{pores}} \tag{2.1}$$

The expression is further simplified by relating it to the powder packing rate PR and the volume of the whole part V_{solid}. This is shown in Equation 2.2. The powder packing rate is an assumed value that is usually taken as the powder tap density ρ_{tap} normalized by the bulk density ρ_{bulk}.

$$S = \frac{V_{binder}}{(1 - PR)(V_{solid})} \tag{2.2}$$

Several studies showed the importance of binder saturation. Shrestha & Manogharan [71] optimized the process for transverse rupture strength and found that binder saturation was one of the critical parameters. Fluid simulations of binder deposition developed by Miyanaji et al. [72] showed that binder saturation is crucial in predicting part quality. Hsu & Lai [68] found that binder content should be optimized to a middle-ground value for optimal dimensional accuracy. Gaytan et al. [47] tailored binder saturation to increase part density. The study focused on bariaum titanate (BTO) nano-scale powder, and found that lower saturation increased part density. Miyanaji et al. [73] showed that a high amount of binder led to dimensional inaccuracies in the x-y direction. Excess binder appeared to seep outside the defined geometry and cause dimensional errors. The authors also observed that increasing binder saturation by 25% increased green strength by 50% for the commercial ceramic powder used for a dental application. Binder deposition speed also has an effect on part quality. However, it is not a controllable variable in most machines. Fast binder deposition speed was found to reduce dimensional accuracy [74]. Stevens et

al. [75] showed that porosity in the outer shell of a complex part was higher than in the core. The authors suggested that interaction of binder and powder at the part edges led to increased porosity in the outer shell.

Powder spreading speed and compaction influence powder packing and hence part quality. Gregorski [15] demonstrated that compacting the powder in the bed through a compaction mechanism produced higher green densities than without compaction. Haeri et al. [76] showed through discrete element modeling and experiments that a higher spreading speed produced a less effective powder packing, and that a rotating roller as opposed to a blade spreader resulted in a more uniform powder bed. Miyanaji et al. [73] demonstrated through a factorial set of experiments that spreading speed impacted dimensional accuracy in the build direction. Green part strength was found to be higher at lower spreading speeds [73], because of the more effective powder particle arrangement. Nonetheless, depending on the powder characteristics, higher spreading speeds can improve dimensional accuracy [69].

Part orientation has an effect on part strength. Doyle et al. [67] studied the effect of part orientation on the tensile strength of steel parts. It was found that orientation did not have a large influence on sintered density for a given layer thickness. However, Vlasea et al. [77] found that, for ceramic calcium polyphosphate parts, part orientation had a significant influence on compressive strength. The difference in observations between the two studies could be due to the different binder systems used and the nature of the materials.

Efforts in the literature have largely not taken a standardized approach to optimization other than the Taguchi method [68, 70, 71]. An approach to capture fit functions as well as parameter interactions can be beneficial. Because of the variability in BJ machine design, many of the studies optimized parameters that were specific to the machine used. Ideally, optimization should target non-dimensional process parameters such that the conclusions could be generalized to all BJ machines. Conversely, it is not recommended to normalize across different materials [78] due to inherent differences in powder particle characteristics and binder properties. These considerations will be taken into account in the studies conducted as part of this thesis.

2.2.3 Studies on Post-process Parameters

Debinding

Debinding refers to the process of removing the binder from the green part, and is a crucial step in the BJ work flow. It serves as a necessary precursor step to sintering. Different forms of debinding exist, including thermal and chemical debinding. In this work, thermal debinding is the process of focus. Debinding is conventionally used in PM and Metal Injection Molding (MIM). During this step, the binder escapes from all internal pores out through the surface pores in the green part.

The three key aspects of debinding parameters are: the set temperature at which the binder is driven off, the isotherm or hold duration and the atmosphere. Depending on the binder material, different temperatures may be required. Most commonly, the binder material is a polymer, and therefore can be removed by allowing it to burn off, decompose or evaporate. The appropriate temperature is selected based on the removal mechanism (for example, the boiling point). The isotherm duration needs to be sufficiently long to remove all the binder from the part. The debinding atmosphere is chosen based on the debinding mechanism. For binders that burn off, debinding can be performed in an oxidizing atmosphere (most commonly air). For metals, oxidation or decarburization can be problematic, so the use of inert atmospheres is more common. Inert atmospheres such as Ar or N_2 are common for binders that decompose or evaporate. Reducing atmospheres are often used in PM, because the reducing agent in the atmosphere is effective at preventing the formation of oxides. Typical reducing atmosphere blends include H_2-Ar or H_2-N_2 mixes, where the percent content of H_2 ranges from 5-100 %. H_2 acts as the reducing agent by preferentially bonding to O and escaping as water molecules. In some PM applications, vacuum may be desired depending on the metal or the binder.

There are two main pitfalls in the debinding step. First, the binder should be driven off in a slow or gradual manner. This is usually achieved by selecting a low heating rate from ambient temperature to the isotherm temperature. Rates of 0.5-10°C/min are typical. Rapid debinding can cause cracking as the binder builds up pressure inside the part faster than it can escape. The second pitfall is incomplete debinding. Leftover binder may interfere with subsequent sintering and produce unexpected results. For instance, residues

from the binder, particularly carbon, can affect the melting behavior of Fe alloys. This problem can be avoided by ensuring that the debinding isotherm duration is sufficient to drive off all the binder.

There is scarce information available in the open literature on debinding strategies for BJ parts. Nandwana et al. [31] identified debinding as a challenge, in particular due to the unwanted carbon-based residues. Although information from the PM domain is helpful in addressing debinding, much of the work still remains to be tackled for BJ.

Sintering

Sintering, in simple terms, refers to the process of subjecting a part to sufficiently high temperatures to cause powder particles to fuse together. The technical definition refers to sintering as a "thermal treatment for bonding particles into a coherent, predominantly solid structure via diffusion or other mass transport events that occur on the atomic scale" [2]. Sintering is usually done at an elevated temperature below the melting or solidus point of the material, so as to form sinter bonds among the particles but not cause total melting and structural collapse. A sintering schedule can be designed for a part depending on the material and the part geometry, where heat ramps, isotherm temperatures and durations are appropriately selected. The outcome of sintering is primarily a densified part with stronger mechanical properties than those of the green part. Different isotherm temperatures, durations and cooling rates result in different densities and microstructures [19, 20].

Different sintering atmospheres are appropriate for different materials. As with debinding, inert or reducing atmospheres are common, and usually produce parts without oxidation defects. Sintering can be also performed in a vacuum. Vacuum sintering in principle minimizes potential defects that can occur under gas atmospheres, such as trapped gas porosity [79]. Nonetheless, vacuum sintering is usually more expensive than sintering in a gas environment due to the infrastructure required. More detailed information on sintering theory is presented later in this chapter. Observations and discussions on microstructural evolution and control are beyond the focus of this thesis.

High part densities are required for the majority of metal applications, and near-full

density parts are possible with BJ after sintering. As of 2019, the ExOne Company is able to produce nearly fully dense steel parts. Final densities of near 99% were achieved for sintered Ni alloy parts [19, 20, 30]. Mostafaei et al. [20] showed that achieving near full density in sintered BJ parts can give mechanical properties equivalent to or even stronger than cast properties.

It is important to tailor the sintering conditions to achieve correct densification of BJ parts. This is arguably more difficult for BJ than it is for PM because of the lower powder packing uniformity in BJ [61] and lower green densities. Sintering temperature has an influence on microstructural evolution, which was observed in BJ parts in [20, 30]. Furthermore, sintering aids such as C or Cu can be added to lower the melting temperature [51]. Additives such as transition metals may be introduced in the powder to lower the sintering temperature in a concept known as "activated sintering" [80]. The outcome of sintering is also influenced by powder characteristics. Smaller particle sizes assist densification. Smaller particles encourage sinter bond formation by reducing the activation energy required to initiate sintering [1]. For a constant temperature, sintering of smaller particles achieves densification faster than that of larger particles [19, 81, 82, 83]. Moreover, the use of bi-modal powders was observed to promote densification [63]. Smaller particles increase packing by filling the voids among larger particles and increasing the particle coordination number.

Post-sintering

Post-sintering steps such as infiltration with a different material may be used to improve part qualities. In metals, infiltrating with a metal of a lower melting point than that of the original part helps to achieve full densities. Infiltration, however, requires interconnected porosity. Above 92% density, porosity becomes enclosed and no longer interconnected [1]. Therefore, infiltration is performed on sintered parts with densities lower than approximately 92%. The ExOne Company routinely performs infiltration on sintered parts to achieve full densities. Infiltration of sintered BJ parts can be done to increase mechanical strength [84].

Aside from infiltration, Hot Isostatic Pressing (HIP) can be used after sintering to

achieve full densities. HIP requires isolated porosity, and is hence performed at densities above 92%. Kumar et al. [85] demonstrated HIP as a post-sintering step to increase sintered part density. The study on copper parts demonstrated nearly 5% increase in density. This could be beneficial for some applications that require above 95% density. The authors also noted higher shrinkage in the z-direction, which was thought to indicate anisotropy in pore distribution or a gravity effect. Achieving near full density through HIP can produce parts with mechanical properties equivalent to alternate processes such as MIM [86].

2.3 Sintering Theory

2.3.1 Solid State Sintering

In 1949, Kuczynski [87] presented a model of sintering at the level of two contacting particles in which he attempted to explain the transport mechanism. This mode of sintering is known as Solid State Sintering (SSS). He suggested that metals mostly sinter via the lattice or volume diffusion of atoms into interstitial spaces. His early work concluded that volume diffusion is dominant for metals, but this was soon debated. Eventually, Rockland [88] suggested in 1967 that grain boundary diffusion was dominant, where sintering occurs as atoms diffuse into the spaces provided by grain boundaries. This meant that sintering starts at lower energies than previously thought, and this has been the consensus ever since [1, 2].

When two particles are in contact, they form a system that is not thermodynamically at equilibrium. This is because the total surface energy is not at a minimum. In theory, the two particles will bond at the contact site after a long period of time has elapsed and the total energy of the system will reach a minimum [87].

Sinter bonding progresses due to surface tension, first shown by Frenkel [89] in 1945. There is a capillary stress that depends on particle surface energy γ (J/m^2) and describes the bond formation [1]. The capillary stress σ (Pa) for a bond forming between two particles of radii R_1 (m) and R_2 (m) is shown in Equation 2.3.

$$\sigma = \gamma\left(\frac{1}{R_1} + \frac{1}{R_2}\right) \tag{2.3}$$

Sintering is characterized by the formation of sinter "necks," which are the bonds that form among compacted powder particles upon the addition of heat. Sinter necking is driven by the reduction of surface energy [1]. Surface energy increases with smaller particle size, allowing higher sintering rates or lower temperature requirements for sinter neck initiation. The random arrangement of particles and pores in a part means that different grain boundary configurations are possible; different grain misorientations have different boundary energies [1]. During sintering, some grains rearrange to reduce their grain boundary energy. Sintering behavior is affected by parameters such as: particle size, particle morphology and surface area, temperature, time, green density, pressure and atmosphere.

It is generally agreed upon that sintering progresses in three stages, as summarized by German [1]. In the "initial stage," sinter necks begin to grow between two contacting particles and porosity is interconnected throughout the green part. Sinter necks at this stage are less than one third of particle size and the bulk part experiences a linear shrinkage of less than 3%. This occurs below the 70% density mark for typical powders in BJ. In the "intermediate stage," pores begin to become more spherical, and grains start to grow. Pores are still interconnected at this stage. This occurs when a part is between 70-92% density. In the "final stage," pores collapse into closed spheres, usually starting above 92% density. At this point, porosity is no longer interconnected. Figure 2.3 is a depiction of the shape of sinter necks at the different stages of sintering.

Sintering is a mass transport phenomenon. Atoms in the particles move because of the heat input, which is the reason why sintering is a thermally activated process. The probability of diffusion of atoms with enough energy into vacant atomic sites is related to temperature via an Arrhenius relationship [1, 2]. The Arrhenius relationship is described in Equation 2.4, where the threshold for atomic movement is the activation energy Q (volume or grain boundary) (J). D is the diffusion coefficient (volume or grain boundary) (m^2/s), D_0 is an atomic vibration frequency constant (m^2/s), R is the universal gas constant (J. $K.mol^{-1}$) and T is the sintering temperature (K). A higher temperature results in faster

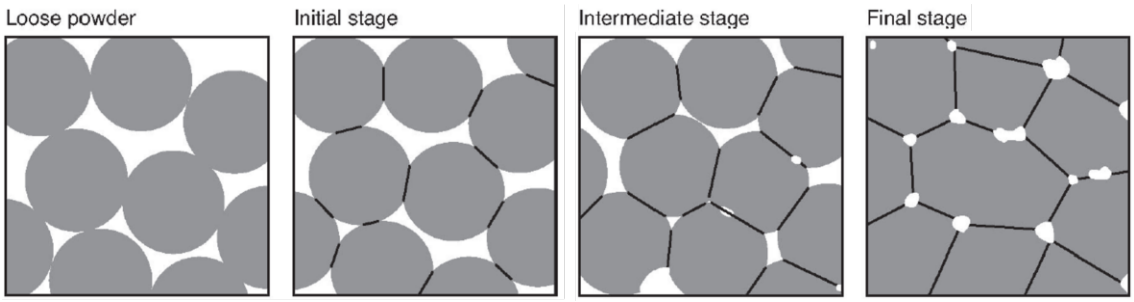


Figure 2.3: The different sintering stages, showing the progression of sinter neck formation; adapted from [1].

diffusion of atoms, or a higher sintering rate.

$$D = D_0 exp\left(- \frac{Q}{RT} \right) \tag{2.4}$$

Sintering action can be classified into two modes: surface transport and bulk transport. Surface transport is attributed to neck formation without densification (no change in particle diameter). Atoms are rearranged but vacancies are not filled. Surface diffusion is the dominant diffusion mechanism at low temperatures, and is thus active during the heat ramp up to the sintering temperature. It has a lower activation energy [1], so it starts earlier in the heat cycle. In contrast, bulk transport is attributed to the movement of atoms from both the surface and the interior regions of a particle. Bulk transport is dominant at higher temperatures. Both grain boundary diffusion and volume diffusion are attributed to this transport mode. Grain boundary diffusion has an activation energy that is between that of surface and volume diffusion, and is the dominant sintering mechanism for most metals [1]. It is typically active in the intermediate stage at densities of 70-92%. At high temperatures (and depending on powder size), volume diffusion can be activated and can lead to significant densification. Volume diffusion has a high activation energy and becomes more important for very fine powders. This is because smaller particles exhibit a lower activation energy threshold due to their large surface area. Figure 2.4 shows a schematic of the mass transport mechanisms in sintering.

Other than diffusion, plastic flow is a mass transport mechanism that occurs early in

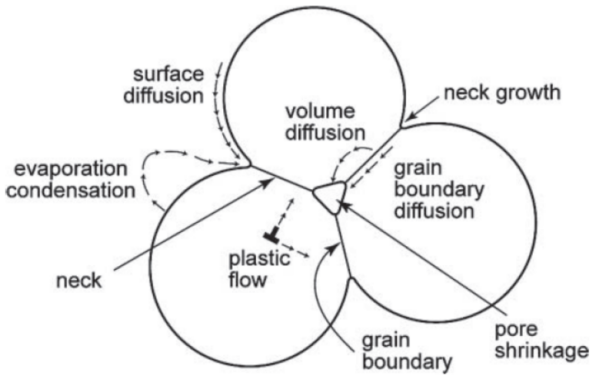


Figure 2.4: Schematic of three particles in contact and various mass transport mechanisms that drive necking in solid state sintering; adapted from [2].

sintering. It is related to dislocation movement [90]. Its presence is understood to decrease as temperature increases due to the elimination of dislocations [1], and its importance in sintering has been a topic of scientific debate [91]. Another mass transport mechanism is viscous flow, which occurs in amorphous materials and to a small extent in crystalline metal sintering at the grain boundaries [1]. In the context of this work, SSS of Fe will be studied. The bulk density and the shape of the sinter necks will be used as indicators of the sintering stages reached.

2.3.2 Liquid Phase Sintering

Most sintering processes in industrial metal applications occur in the liquid phase [1]. While SSS applies to sintering of pure metals, Liquid Phase Sintering (LPS) applies to multi-material systems and alloys. LPS leads to very rapid densification compared to SSS [3]. This is primarily motivated by the presence of a capillary force that arises from the liquid phase presence. Figure 2.5 illustrates two particles undergoing LPS. Equation 2.5 describes the forces in terms of surface energy at the liquid-vapor interface γ_{LV} (J/m^2), curvature radius r (m), neck width x (m) and angle ψ (°). The capillary force appears due to the liquid-vapor surface tension and densification occurs almost immediately [3]. It is an attractive force that acts on the solid particles in an inward fashion, and its magnitude is

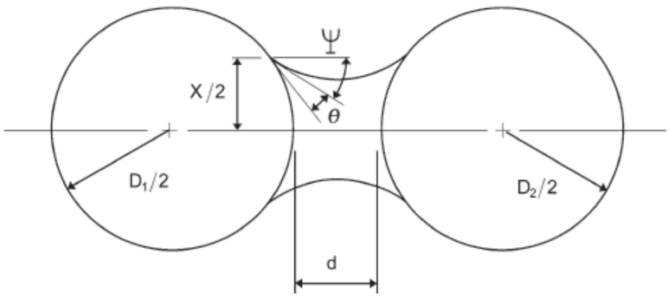


Figure 2.5: An illustration of two particles undergoing LPS, showing the geometry used to calculate the capillary force; adapted from [3].

high in comparison to SSS. Its effect on densification is such that pressure-assisted sintering produces no tangible benefits to densification rates [79]. More in-depth work on modelling of capillary forces in LPS and experimental validation is contained in [3, 92]. Generally in LPS, the liquid volume fraction is in the range of 5-15% [3] and the remainder is solid. This volume fraction is needed such that microstructural softening is not severe and the geometry does not collapse. Pores may grow during LPS due to vapor phase production and elimination of small pores. Often, an external force such as HIP is used after sintering to close large pores [3].

$$\begin{aligned} F_{total} &= F_{capillary} + F_{surface\,tension} \\ &= \gamma_{LV}\left(\frac{1}{r} - \frac{2}{x}\right)\frac{\pi x^2}{4} + \gamma_{LV}\pi x\cos\psi \end{aligned} \tag{2.5}$$

In the context of alloys powders, LPS can take three forms. The most common form is Transient LPS, where a liquid phase forms for a short duration and then dissolves into the solid [3]. The other two are a liquid phase that is present throughout the sintering process, known as Persisent LPS, and insoluble liquid-solid systems with solid skeleton sintering.

The liquid phase behaves as a wetting surface against the solid. When the liquid forms, the microstructure contains solid, liquid and vapor phases [3]. The contact angle θ (°) between the liquid, solid and vapor phases is described by Equation 2.6, where γ_{SV}, γ_{SL}

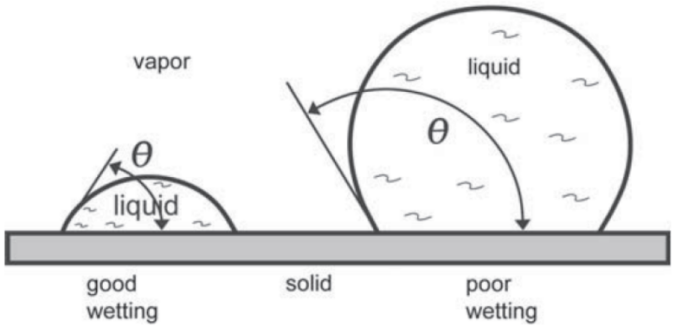


Figure 2.6: Illustration of wetting behavior of a liquid against a solid, relevant to liquid phase sintering. Smaller contact angles improve densification as grains are pulled together well; adapted from [3].

and γ_{LV} are the surface energy terms (J/m^2) for the solid-vapor, solid-liquid and liquid-vapor interfaces respectively [1] (see Figure 2.6).

$$\gamma_{SV} = \gamma_{SL} + \gamma_{LV} \cos(\theta) \tag{2.6}$$

The grain boundary interface between two solid phases and a liquid phase is described by the dihedral angle [1]. In Equation 2.7, ϕ is the dihedral angle (°), γ_{SS} is the solid-solid interface energy (J/m^2) and γ_{SL} is the solid-liquid interface energy (J/m^2). If a vapor were present instead of a liquid phase, then the solid-vapor interface energy term γ_{SV} would be used instead.

$$\gamma_{SS} = 2\gamma_{SL} \cos\left(\frac{\phi}{2}\right) \tag{2.7}$$

Supersolidus Liquid Phase Sintering

The description for LPS applies to a general mixture of elements with dissimilar melting points. Often for metals, one powder of a pure metal is mixed with a powder of different pure metal, thereby creating a mixture of distinct particles. In pre-alloyed powders, the

powder particles themselves consist of the various alloying elements of the alloy. For such powders, the sintering mode is known as Supersolidus Liquid Phase Sintering (SLPS). German [93] proposed the theory of SLPS in 1990. As the name implies, LPS is achieved by elevating temperatures to just above the solidus point of the alloy to create a liquid fraction in the powder. Liquid formation starts within powder particles and emerges out to wet the solid and enlarge the sinter necks. The liquid phase can usually be seen solidified at the location of the sinter necks, along grain boundaries and within the grains themselves [4].

Phase diagrams can be used to guide the selection of the sintering temperature. Careful control of the temperature is needed to obtain a small liquid fraction and avoid melting. This is an important practical consideration for sintering of BJ products. However, phase diagrams can be inaccurate by as much as 50°C for SLPS predictions [4]. Liquid can form earlier than the predicted solidus point. This is because particles solidify in non-equilibrium during atomization [93]. In PM, the hold duration at the maximum temperature is usually 10-60 min [93], although examples in BJ literature exist where the hold duration was over two hours [19, 30]. Figure 2.7 illustrates the progression of SLPS. SLPS can result in a homogeneous microstructure and superior mechanical properties if sintered to full density [4], in the context of PM products. In this work, LPS of Fe-Si powder will be studied to produce high densities in sintered samples. Observations of sinter necking and comments on the influence of the liquid phase will be made.

Microstructural Softening Parameter

Microstructural softening can occur in LPS, which can lead to geometrical distortion and loss of shape fidelity. It is useful to define a limit for this phenomenon that can be used during sintering to avoid distortion. Liu et al. [94] proposed such a limit for SLPS, expressed as the parameter ζ. This parameter is known as the "microstructural softening parameter" [94] and it depends on temperature and several material properties. To maintain shape fidelity, the parameter should be within a range such that liquid phase densification occurs but without structural collapse. The range is defined by threshold values for densification ζ_{densif} and microstructural softening $\zeta_{distort}$. There is some difficulty in accurately estimat-

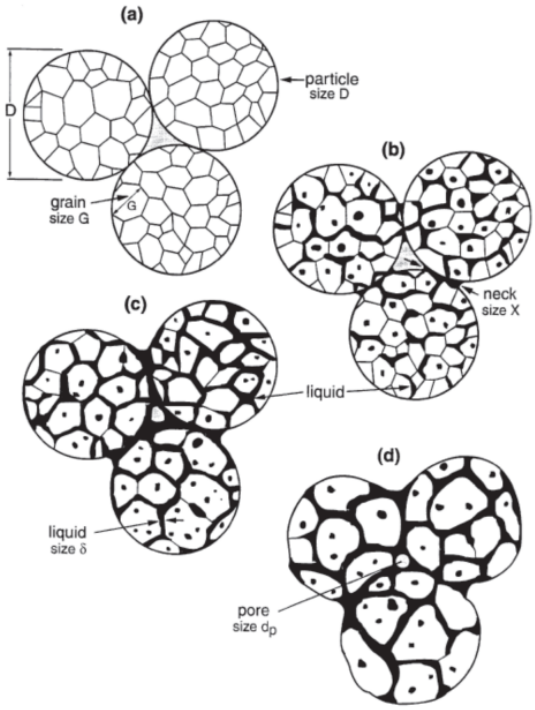


Figure 2.7: Illustration of supersolidus LPS in a pre-alloyed powder; adapted from German [4]. (a) Initial packed powder particles, (b) start of liquid formation with insufficient grain boundary wetting for densification, (c) and (d) continued densification into the final stage with pores closing.

ing the parameters for a given powder, due to the difficulty in obtaining accurate data on its material properties. For this reason, identifying the thresholds is beyond the scope of this thesis. More in-depth information on defining these parameters can be found in [94].

2.4 Master Sinter Curves

2.4.1 The Master Sinter Curve Concept

Predicting sintering behavior is difficult because of the dependence of sintering on a multitude of material parameters and the difficulty in accurately determining these parameters [79]. For this reason, the PM community developed an empirical concept to capture sintering behavior without needing to accurately know the material parameters. This concept is known as the Master Sinter Curve (MSC).

Frenkel [89], in 1945, proposed the idea that viscous materials sinter through mechanisms motivated by surface tension. The various stages of sintering and different diffusion modes made it necessary to develop a model that captures the entire sintering process. This led to the development of a combined stage sinter model by Hansen et al. [91]. The model would later become the basis of the MSC concept. The model has two underlying assumptions: (1) densifying mass transport kinetics are due to capillary forces (and not dislocations); and (2) changes in the microstructure can be captured through quantifiable parameters. Hansen's model attempted to correctly capture two such parameters – one for geometrical changes and one for scale. Geometrical changes represent rearrangement of grain boundaries and pores and are denoted by the dimensionless parameter Γ. Scale is represented by a dimensional parameter. The mathematical derivations, microstructure assumptions and experimental validation of the combined stage model are presented in detail by Hansen [91], including derivation of the Γ parameter. The model describes the linear shrinkage rate dL/dt (m/s) as a function of material and geometrical properties, as shown in Equation 2.8:

$$-\frac{dL}{Ldt} = \frac{\gamma\Omega}{kT}\left(\frac{\delta D_B \Gamma_B}{G^4} + \frac{D_V \Gamma_V}{G^3}\right) \tag{2.8}$$

where γ is the surface energy (J/m^2), Ω is the atomic volume (m^3), k is the Boltzmann constant (W.m.K^{-4}), T is the temperature (K), D_V and D_B are the volume and grain boundary diffusion coefficients (m^2/s), G is the average grain size (m), δ is the grain

boundary width (m), and Γ_V and Γ_B represent the volume and grain boundary microstructural changes that impact sintering kinetics.

This equation forms the basis from which the MSC was derived by Su & Johnson [5] in 1996. The motivation behind the MSC was the need to characterize sinterability of a powder-compacted body for a range of green densities. The MSC is therefore an empirical concept that is industrially relevant for powder compacting processes. If isotropic shrinkage were assumed, Equation 2.8 can be directly expressed in terms of density ρ, as shown in Equation 2.9 [5]. The grouping of the two Γ terms stems from an important assumption that either volume or grain boundary diffusion is the dominant mechanism for densification through sintering. For most metals, grain boundary diffusion is the dominant mechanism [1]. The rearrangement in this form separates the microstructural evolution terms on the left hand side from the atomic diffusion parameters on the right hand side. Another assumption made here is that G and Γ are functions of density alone.

$$\int_{\rho_0}^{\rho} \frac{(G(\rho))^n}{3\rho\Gamma(\rho)} d\rho = \int_0^t \frac{\gamma\Omega D_0}{kT} exp\Big(-\frac{Q}{RT}\Big) dt \tag{2.9}$$

Equation 2.9 can be rearranged into Equation 2.10 that expresses microstructural and atomic diffusion parameters on one side and the time-temperature profile on the other (with the exception of activation energy Q). The left hand side of Equation 2.10 is the densification term, denoted by $\Phi(\rho)$, and represents the effects of microstructural evolution on sintering kinetics. The right hand side represents the work of sintering, denoted by $\Theta(t, T(t))$. Equation 2.10 can thus be simplified into Equation 2.11, which summarizes the concept of the MSC.

$$\frac{k}{\gamma\Omega D_0} \int_{\rho_0}^{\rho} \frac{(G(\rho))^n}{3\rho\Gamma(\rho)} d\rho = \int_0^t \frac{1}{T} exp\Big(-\frac{Q}{RT}\Big) dt \tag{2.10}$$

$$\Phi(\rho) = \Theta(t, T(t)) \tag{2.11}$$

Most materials experience both volume and grain boundary diffusion [6], and grain growth can affect the actual activation energy for densification; as a result, empirically

derived activation energy values for densification are often different than those reported in literature for volume or grain boundary diffusion [6]. The empirically derived activation energy is often called the "apparent" activation energy because it relates to multiple diffusion mechanisms and phenomena occurring at the grain level.

2.4.2 Linearization of the Master Sinter Curve

A linearized form of the MSC developed by Blaine et al. [6] helps in using the MSC as a predictive model for densification through sintering. The relationship between relative density of a part and the sintering work parameter can be expressed as a sigmoidal function [95, 96, 97, 98, 99], described in Equation 2.12. The equation depends on knowledge of the starting green density ρ_0, and empirically determined fit coefficients a and b used in the sigmoid model.

$$\rho = \rho_0 + \frac{1-\rho_0}{1+exp\Big(-\frac{\ln\Theta - a}{b}\Big)} \tag{2.12}$$

This can be rearranged to express a densification parameter Ψ, which describes densification with respect to the original starting (green) density [6]. This is shown in Equation 2.13.

$$\Psi = \frac{\rho-\rho_0}{1-\rho_0} = \frac{1}{1+exp\Big(-\frac{\ln\Theta - a}{b}\Big)} \tag{2.13}$$

To utilize the MSC concept, measurements of linear shrinkage of a powder-compact green body undergoing densification sintering are needed, as well as time and temperature. Such measurements can be obtained through dilatometry experiments. Dilatometry is a thermo-analytical method that relies on contact or non-contact measurements of shrinkage of a green body as it is subjected to a time-temperature profile. The measurements allow estimation of the activation energy Q and obtaining the relative density or $\Phi(\rho)$ as a function of the work of sintering $\Theta(t, T(t))$. Determination of the activation energy Q, as proposed by Blaine et al. [6] is through minimizing the mean residual R in Equation 2.14.

This depends on the final density ρ_f, the number of dilatometry measurements N, the work of sintering at the i^{th} value of density Θ_i and the average value of work of sintering at the i^{th} value of density $\Theta_{i\,avg}$. The mean residual R is determined for different values of the activation energy Q, and the minimum residual value corresponds to the correct activation energy observed in the measurements.

$$R = \sqrt{\frac{1}{\rho_f - \rho_0} \int_{\rho_0}^{\rho_f} \frac{\sum_{i=1}^{N} \left(\frac{\Theta_i}{\Theta_{i-avg}} - 1 \right)^2}{N} d\rho} \tag{2.14}$$

Examples of MSCs from PM literature are shown in Figure 2.8. It was found that correcting for the coefficient of thermal expansion (CTE) could be needed to avoid skewing of dilatometry measurements [44]. The apparent activation energy Q was found to be impacted by particle size by Park et al. [100]. Smaller particle sizes resulted in lower Q values, which is in agreement with the theory [1]. Generally, literature that applies to the MSC is related to PM processes and not explicitly to BJ. Applying the MSC to BJ was proposed and tested in initial trials in [44], and is part of ongoing work. In the following section, the MSC concept is evaluated further to investigate how it can be implemented for LPS of BJ parts.

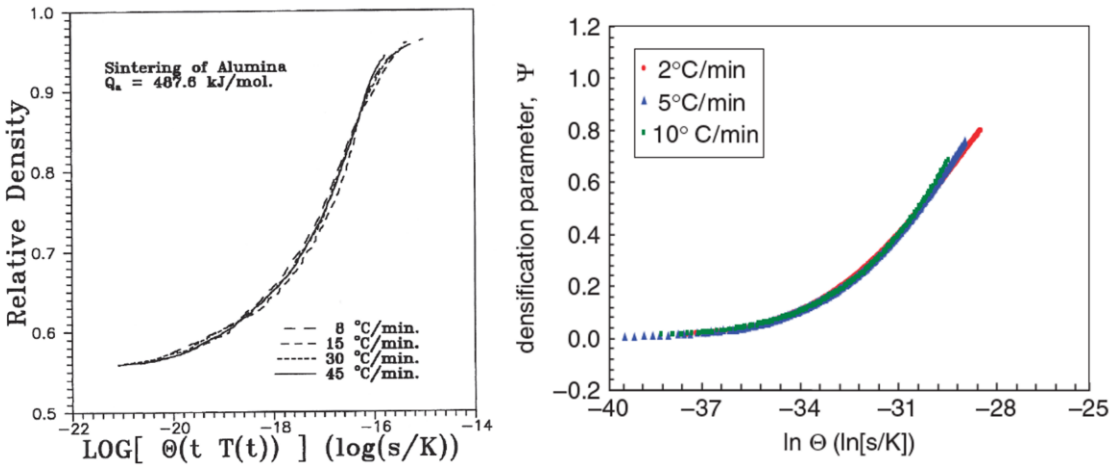


Figure 2.8: Examples of MSCs for (left) alumina [5] and (right) a tungsten-heavy alloy [6].

2.4.3 Master Sinter Curve for Liquid Phase Sintering

The derivation by Su & Johnson (Equation 2.10) relied on a critical assumption that states that grain growth is only a function of density [5]. This makes it suitable in its original form for SSS. In LPS, the grain growth rate changes depending on the volume fraction of the liquid [79]. As a result, the MSC can be applied to LPS after some modifications, as demonstrated by Bollina et al. [7] for a PM application. The variation in grain growth due to the liquid phase can be captured by modifying the work of sintering parameter in the MSC formulation, as expressed in Equation 2.15. A coefficient was introduced that assumes that the dominating mechanism is grain boundary diffusion with a fourth power relation to grain size. This modification no longer upholds the original assumption that grain growth G is only a function of ρ [7].

$$\Theta_{\rho/G}(t,T) \equiv \int_0^t \frac{1}{(G_0^3 + 3\Theta_G)^{4/3}} \frac{1}{T} exp\Big(- \frac{Q}{RT}\Big) dt \tag{2.15}$$

The results obtained by Bollina et al. were successful. The resulting MSC is shown in Figure 2.9. At the point of reaching the solidus temperature, densification rates increase enormously [79], which is evident in the figure by the rapidly increasing densification parameter at the rightmost end of the curve. The fitted model required some modification of the fitting parameters for the different regions of curve to capture the different grain growth behavior. Their model with and without accounting for grain growth due to liquid phase showed good fits, but the activation energy was less accurate without accounting for grain growth.

In this thesis, the framework for constructing the MSC for LPS of BJ parts is developed. The experimental procedure for dilatometry is suggested. The dilatometry measurements, analysis of the data and subsequent development of the MSC lies beyond the scope of this work, as the data will only become available after publication of this thesis. Sintering studies of Fe-Si in the liquid phase will serve as precursor information before dilatometry measurements.

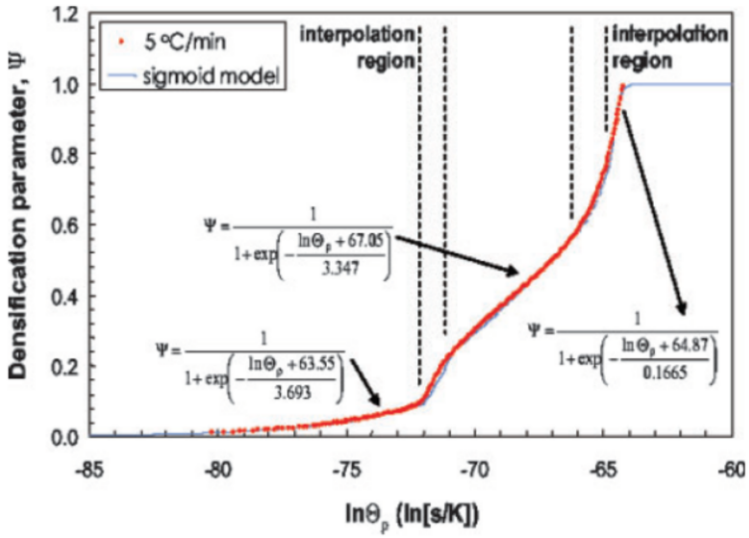


Figure 2.9: Example of a master sinter curve for liquid phase sintering for 316L stainless steel; adapted from [7]. The onset of the liquid phase is evident in the steep slope of the curve.

2.4.4 Master Sinter Surfaces

With industrial applications of the MSC in mind, it is possible to extend the concept for more utility. A Master Sinter Surface (MSS) is a collection of MSCs created for different conditions, effectively adding an extra dimension to the plot. This was demonstrated in several examples in literature [8, 101, 102]. One application could be constructing pressure-assisted MSSs as demonstrated by Brandt & Rabe [8], where densification behavior was determined for time-temperature profiles as well as pressure profiles. Brandt's MSS is presented in Figure 2.10.

In the context of BJ, the MSS can be used to include pre-process, process or post-process parameters as a third dimension. One possibility is using a process parameter such as layer thickness or a non-dimensional parameter such as packing factor as the third dimension. Construction of such surfaces could be helpful in accelerating process developments for new products and applications. In the context of this work, the MSS is an additional step after constructing the MSC. Following the MSC, the MSS can be explored where the third

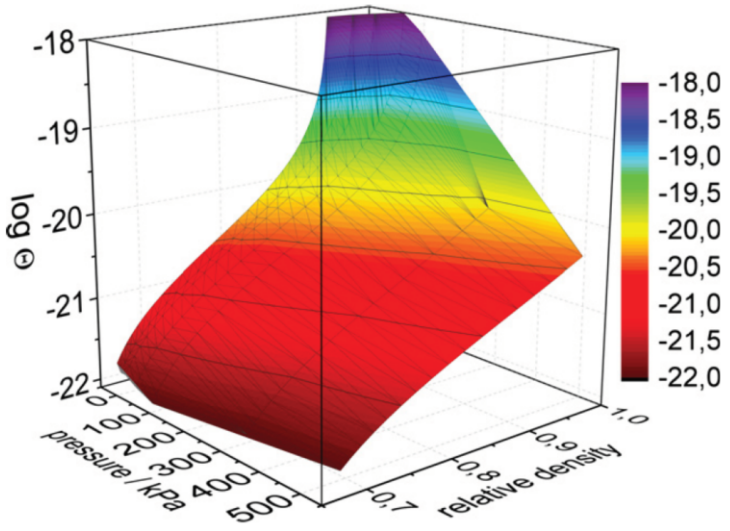


Figure 2.10: Example of a sinter surface that expresses densification behavior against time-temperature and pressure profiles; adapted from [8].

dimension is packing factor of the powder in the BJ process. Such a three-dimensional process map can be very helpful for optimization and general process development for new materials and applications. More discussion on the packing factor as a non-dimensional parameter is presented in Chapter 4. The MSS can thus investigate both SSS and LPS regimes depending on the material system. The MSS would be the terminal point in the BJ process development work flow.

Chapter 3

Binder Jetting and Sintering of Fe

3.1 Motivation

The purpose of this chapter is to demonstrate a successful process development cycle for commercially pure Fe powder. The Fe powder in this work was water-atomized. The use of water-atomized powders in BJ is a fairly recent topic of interest. In metal powder production, water atomization is much less expensive to use than gas or plasma atomization. In general, water atomization leads to an irregular particle shape, while gas or plasma atomization leads to a spherical shape. This is primarily attributed to the cooling rate that molten metal droplets experience during atomization. Typically, spherical powders allow for a higher packing density in the powder bed, thereby increasing the attainable density of a printed sample [61]. Efficient packing is hindered by inter-particle friction and mechanical interlocking in the part itself [15]. Hence, in the case of irregular powders, particles exhibit a large surface friction, leading to less efficient packing [61]. Schade et al. [61] compared water-atomized with gas-atomized powder characteristics as required for AM processes. The authors demonstrated that water-atomized powders are theoretically fit for use in AM processes. By using a low water-to-metal ratio and a high water pressure, water atomization can produce slightly more spherical particles [61]. This may be important for powder manufacturers who want to improve their powder packing.

Water-atomized metal powders were used in BJ on a few occasions in literature. In-

aekyan et al. [103] studied the density and mechanical strength of BJ parts produced with water-atomized Fe powder and sintered under typical PM conditions. The authors obtained low part densities of nearly 45%, primarily due to the low temperatures used. By contrast, Mostafaei et al. [20] achieved 95% density parts made from water-atomized superalloy Inconel 625, compared to 98% with those from a gas-atomized powder. Such high densities are promising results for water-atomized powder manufacturers. Since water-atomized powders are less expensive to produce, they may be used to further leverage the low-cost advantage of BJ. Exploiting this advantage can lead to faster industrial adoption.

The work flow derived in this chapter can serve as a starting point for industrially relevant ferrous metals, including Fe and many types of steels. Fe is directly applicable in soft magnetic materials for electromagnetic applications in PM [104]. The goal of the chapter was to produce green parts with high green densities and then sintered parts with high final densities. The processing of Fe was performed in support of a direct collaboration with Rio Tinto, with the intent to advance industrial adoption of BJ for ferrous alloys. The objectives of this chapter are therefore to:

1. Establish a process map for Fe to produce sufficiently high green densities; and
2. Develop debinding and sintering schedules that produce high final densities.

This chapter explores the effects of key process and post-process parameters on part density for Fe powder. Powder compaction, layer thickness and binder amount were varied to increase green density. The effect of process parameters on debinding was explored, and four sintering schedules were studied to increase sintered density.

3.2 Experimental Methods

3.2.1 Material System

The powder material used was water-atomized, commercially pure Fe powder (AT-1001-HP, Rio Tinto Iron & Titanium, Sorel-Tracy, QC). The powder composition was +99.4%

Fe, 0.18% Mn, 0.09% O, 0.01% S and 0.004% C. The powder was sieved down to mesh size -325 or < 45 μm. The powder was characterized for size distribution (Retsch Camsizer X2, Newtown, PA). Particle surface morphology was imaged via Scanning Electron Microscopy (SEM) (LEO 1530 SEM, NY).

Both liquid and solid-state binders were used in this study. The Fe powder was blended with polyvinyl alcohol (PVA) powder (Alfa Aesar, Ward Hill, MA) with a particle size of < 63 μm, forming a blend of 99 wt% Fe powder and 1 wt% PVA. Blending was performed by using a rotary tumbler (Thumlers A-R12, Auburn, WA) for 30 min. A commercial, water-based solvent (Zb60, Z-Corporation, Burlington, MA) was used as the liquid binder. While the exact composition of the liquid binder was proprietary, the composition was approximately 85-95% water and the remainder a glycerol-based compound. The PVA acted as a solid binding agent during printing to increase the binding strength of the liquid binder. In this chapter, use of the word "binder" refers to the binder mixture, unless otherwise stated.

3.2.2 Green Sample Fabrication

A commercial ZPrint 310 Plus (3D Systems, Rock Hill, SC) was used to produce the green samples. Three process variables were controlled in printing: roller actuation (which influences compaction), layer thickness and binder level. The roller actuation was varied from "ON" to "OFF" by manually disconnecting the roller pulley, thereby remaining static during printing. The roller rotates counter to the direction of spreading, which creates a compaction force on the powder bed. Layer thickness and binder level were varied by changing the printing settings in the machine. Cylindrical samples were printed, measuring 5 mm in diameter and 8 mm in height. Each printing batch contained 16 replicates. The machine design relied on a feed-bed system instead of a hopper to deliver powder. The build bed and feed bed were modified from the original size by using inserts to fit an xyz envelope of 32 mm $\times$ 32 mm $\times$ 50 mm. The experimental design table for the process parameters is summarized in Table 3.1. The printed samples were dried in the powder bed at 40°C before removal.

Table 3.1: The process parameters used for the Fe study.

Build	Compaction	Layer Thickness (μm)	Binder Level (pL/drop)
A	ON	75	70
B	ON	75	105
C	ON	100	70
D	ON	100	105
E	ON	125	70
F	ON	125	105
G	OFF	75	70
H	OFF	75	105
I	OFF	100	70
J	OFF	100	105
K	OFF	125	70
L	OFF	125	105

3.2.3 Density Estimations

Estimations of sample green and sintered density were first made via geometrical and mass measurements. Geometrical measurements by using calipers (Mitutoyo Absolute Digimatic Caliper, Mississauga, ON) and mass measurements by using a scale (Sartorius Secura 225D, Göttingen, Germany) of the samples were performed. The density was calculated by using Equation 3.1, in which m was the mass of the sample (g), h was the sample height (cm), and a and b were the major and minor diameters of the cylindrical samples (cm).

$$\rho = \frac{m}{\pi \frac{ab}{4} h} \tag{3.1}$$

The mass and calipers technique provided relative comparison of density across the samples; a more accurate density estimate was made through computed tomography (CT) imaging. Green and sintered sample densities were determined through CT images (ZEISS Xradia 520 Versa 3D X-ray Microscope, Pleasanton, CA). A voxel size of 5.5 μm was used, with an accelerating voltage of 140 kV, 5.5 s exposure time, 4X optical magnification and

capturing 1201 projections for reconstruction. Samples were stacked vertically in a sample holder. CT imaging relies on cone beam X-rays that illuminate the object throughout the measurement. The transmitted X-rays are converted to photons in the visible light spectrum by a scintillator, magnified by using the objective lens and then detected by a charge-coupled detector (CCD). The sample was rotated over 360° while a sequence of two-dimensional images was taken. Reconstruction of the projections was completed by using the ZEISS Scout-and-Scan Control System Reconstructor Software package, and a series of grayscale images with 16-bit intensity ranges was produced. Examples of images reconstructed in 3D are shown in Figure 3.1 for green and sintered sample A.

Advanced image processing and porosity analysis were performed by using Dragonfly Pro v3.1 (Object Research Systems Inc., Montréal, QC). The reconstructed dataset was denoised and filtered by using a 3D non-local means filter. The dataset was cropped and segmented into the solid material and pores. Segmentation was performed by using the Otsu algorithm with manual adjustment. Binarized images obtained following segmentation and morphological operations were used for relative density calculation. The binarized datasets were manually aligned with the z-axis of the CT scanner corresponding to the build direction; this was completed in ImageJ (Fiji, version 1.51) by using the "Rotate" function with bilinear interpolation. Relative density was calculated by dividing 2D projections of the binarized dataset by a binary mask in which each pore was closed by using the ImageJ plugin, "Fill Holes."

The calipers density estimates were then correlated with the accurate CT densities. This made it possible to determine the density for three replicates per build, which was the basis for further analysis of density.

3.2.4 Debinding and Sintering

Different post-process variables were varied: debinding duration, sintering temperature and sintering duration. The debinding schedule was developed based on thermogravimetry (TG) of the binder. TG is a thermal analysis technique that allows tracking of mass change of a sample as it is subjected to heat. A TG measurement (Netzsch Jupiter STA 449 F1,

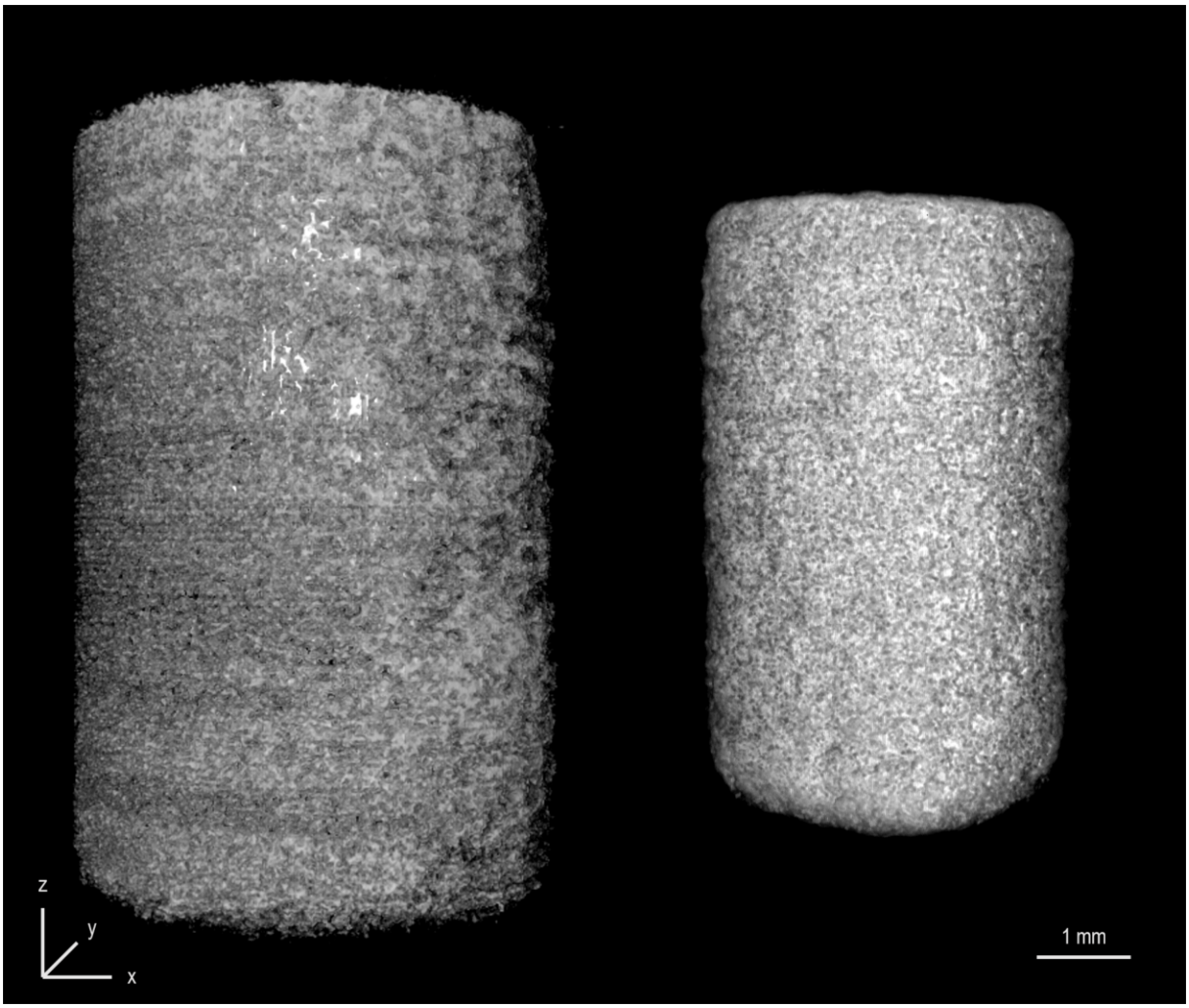


Figure 3.1: CT images of green and sintered samples were captured and reconstructed for analysis. This visual illustrates the (left) green and (right) sintered sample A in a 3D visualization.

Selb, Germany) was first performed on the binder alone. An appropriate debinding temperature was derived from this experiment. Subsequently, TG experiments were performed on the green samples under atmospheric air. The binder was removed by burning. The influence of process parameters on debinding duration was investigated based on the TG data.

The framework for sintering was developed based on examples from literature [13, 20, 43, 77, 103]. Temperature was increased directly from the debinding up to the sintering temperature at a heating rate of 10°C/min. Sintering was conducted in the same TG system, which enabled tracking of the sample mass. This was beneficial in detecting mass gain due to oxidation. Two sintering temperatures were studied: 1390°C and 1490°C, corresponding to 90% and 97% of the powder melting point respectively. Two isotherm durations were studied: 2 hours and 6 hours. The temperatures and durations were chosen to promote significant densification in Fe based on knowledge from SSS theory [1]. Sintering was done under a high-purity reducing atmosphere of 5% H_2-Ar. SEM imaging of the sintered samples was conducted to observe sinter neck formation (Tescan Vega3 SEM, Warrendale, PA).

The bulk shrinkage incurred by the sintering process was quantified via Equation 3.2, with x_G being the measured dimensional feature of a green sample and x_S that of the sample after sintering. Shrinkage measurements were estimated in the radial and z-axis directions by using calipers (Mitutoyo Absolute Digimatic Caliper, Mississauga, ON).

$$Shrinkage_x = \frac{x_G - x_S}{x_G} \times 100\% \tag{3.2}$$

3.3 Results

3.3.1 Metal Powder Characteristics

Figure 3.2 illustrates SEM images of the powder, showing its irregular and angular shape. Initial observations on powder flow showed that while the powder flowed well, it did not flow as well as typical spherical powders. This is consistent with the general understanding

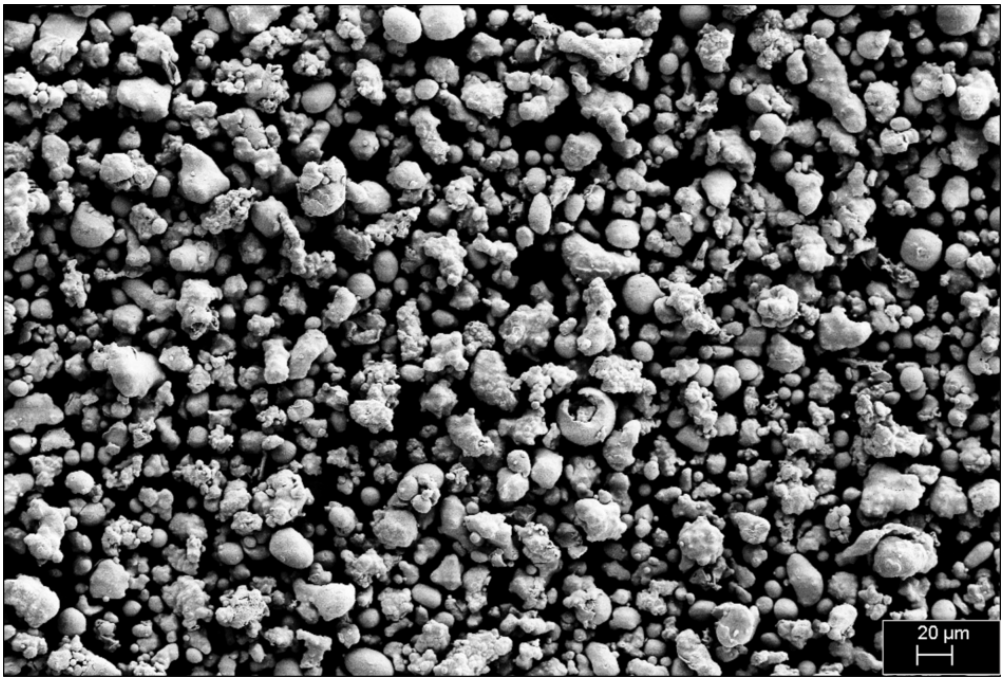


Figure 3.2: SEM images of the Fe powder showing irregular particle morphology at a magnification 200×.

of irregular powders [61, 105]. The PSD was measured to range from 15.7 ± 0.1 μm to 44.1 ± 0.2 μm with a D_{50} of 29.1 ± 0.3 μm. The layer thickness values in the experimental study were selected to be greater than the D_{50} value, in order to avoid problems with powder flow. Particle sphericity was 0.9-0.75 for the size range, with larger particles being less spherical. Sphericity at the D_{50} size was measured to be 0.8.

3.3.2 Effects of Process Parameters on Green Density

Green densities were calculated based on segmentation of the CT images. An example of a segmentation step on a green sample (sample A) is shown in Figure 3.3 in the xy plane. The green densities of all the builds are summarized in Table 3.2. In the table, the layer thickness normalized by the D_{50} of the powder is shown as L^* in parentheses. Based on the CT images, the highest density was obtained for build A, with roller rotation

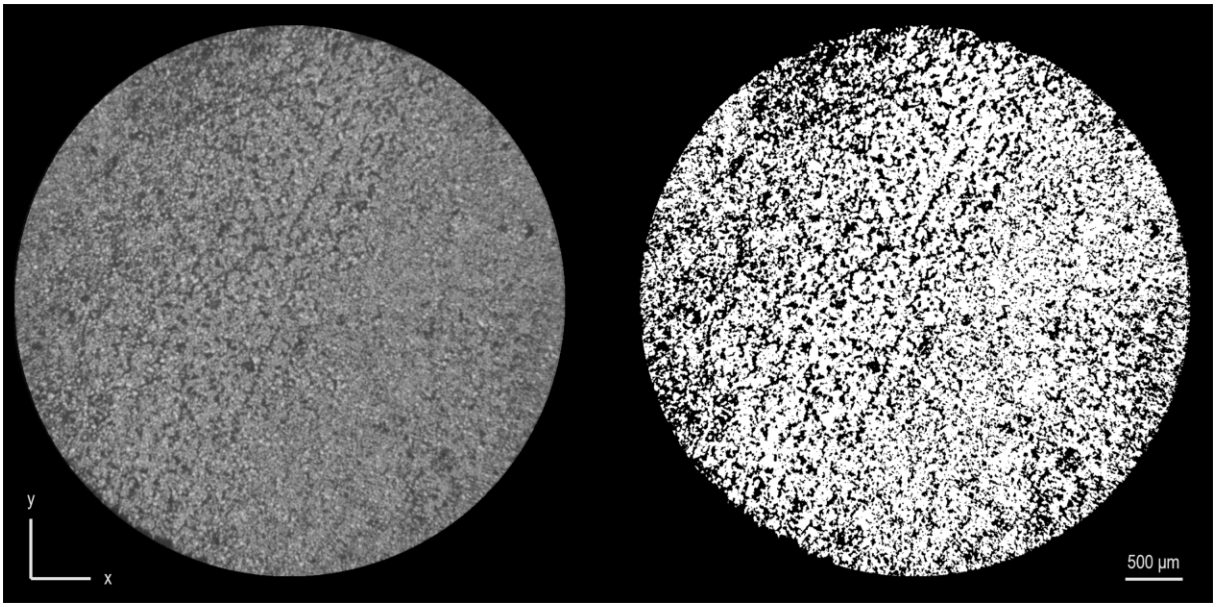


Figure 3.3: CT images were segmented for density calculation; (left) unsegmented and (right) segmented images in the xy plane of sample A in the green state.

enabled, a layer thickness of 75 μm and a binder level of 70 pL/drop. In build A, the CT-calculated density was 48.1%, and the highest density measured across the samples in that build was 50.6%. The mean density for this build was 49.7 $\pm$ 1.4%. This density value is within the acceptable range for BJ. However, the irregular powder shape likely led to inefficient packing in the bed [61], leading to the range of green densities obtained in this study. In addition, the selected parameter range could have not captured the optimal parameter combination for maximum green density. Another contributing factor was likely that rotational speed was varied only from "ON" to "OFF" instead of varying the value.

Process maps for green density could be drawn by examining how green density was affected by the different parameters. Green density process maps are illustrated in Figure 3.4 as plots of green density against (normalized) layer thickness and binder volume. The plot of green density against binder volume describes the volume of binder in the entire sample. Binder volume V_B was calculated for each build based on the binder level V_{drop} (pL/drop), the number of layers N_L and the layer area (in^2), as shown in Equation 3.3.

Table 3.2: Green densities obtained for the various builds for Fe.

Build	Compaction	Layer Thickness (μm) (L^*)	Binder Level (pL/drop) (Binder Volume (μL))	Green Density (%)
A	ON	75 (2.6)	70 (82.1)	49.7 ± 1.4
B	ON	75 (2.6)	105 (123.1)	45.0 ± 0.9
C	ON	100 (3.4)	70 (61.1)	37.3 ± 2.0
D	ON	100 (3.4)	105 (92.0)	40.0 ± 0.2
E	ON	125 (4.3)	70 (49.1)	41.2 ± 2.3
F	ON	125 (4.3)	105 (73.6)	38.2 ± 0.7
G	OFF	75 (2.6)	70 (82.1)	17.6 ± 0.2
H	OFF	75 (2.6)	105 (123.1)	35.7 ± 1.8
I	OFF	100 (3.4)	70 (61.1)	24.4 ± 1.4
J	OFF	100 (3.4)	105 (92.0)	24.8 ± 0.7
K	OFF	125 (4.3)	70 (49.1)	20.8 ± 0.3
L	OFF	125 (4.3)	105 (73.6)	27.0 ± 0.6

The number of layers depended on the layer thickness, as all samples were 8 mm in height. The printhead resolution R was 600 DPI (dots per inch) in x and y. The sample diameter d per the CAD was 5 mm or approximately 0.1985 in. Binder volume was selected for analysis instead of the original binder level as it allowed for a fairer comparison across the samples. Although two builds contained the same binder level, a difference in the layer thickness (and hence, number of layers) meant that the total volume of binder was different. In principle, using binder volume should show more meaningful trends. The binder volume is shown for the samples in Table 3.2 in parentheses.

$$V_B = N_L \times R^2 \times \pi \frac{d^2}{4} \times V_{drop} \tag{3.3}$$

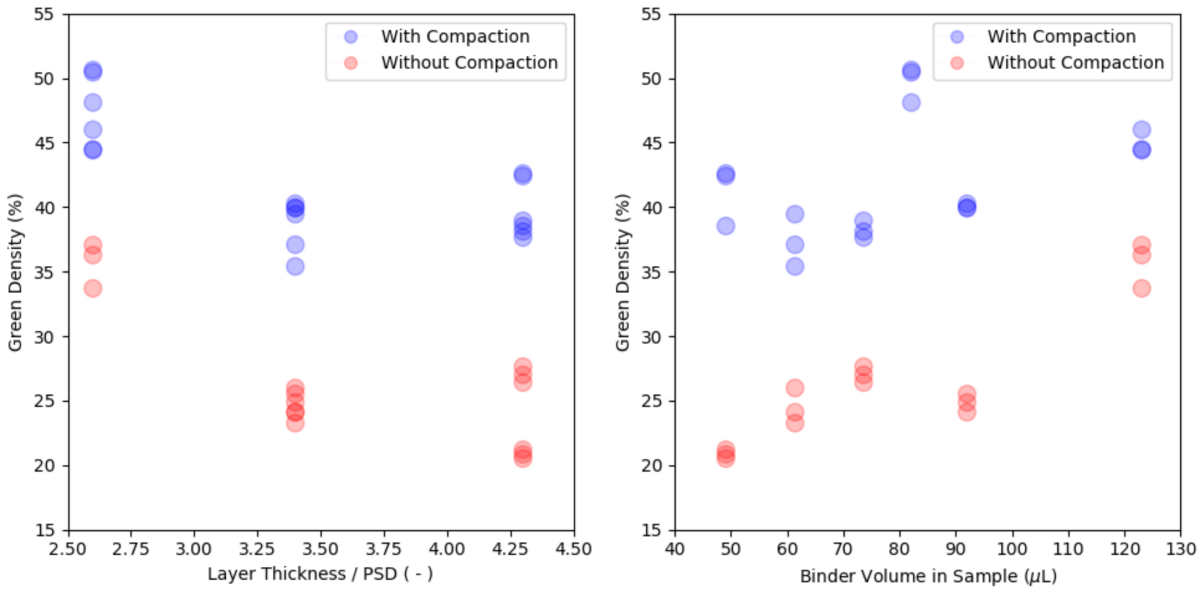


Figure 3.4: Plots of green density against (left) layer thickness and (right) binder volume.

Regression Analysis

It is important to note that the observed effects of compaction, layer thickness and binder volume on green density were not decoupled from one another. Therefore, it was useful to analyze trends in the data through a regression model with Analysis of Variance (ANOVA). A threshold of $p < 0.05$ was used for statistical significance. The complete tables of the Ordinary Least Squares (OLS) linear regression model and ANOVA are contained in Table B.1 and Table B.2. The residuals and Q-Q plots for the regression model are presented in Figure B.1 and Figure B.2.

The trend in the data showed that powder compaction highly influenced green density. Compaction was the most significant parameter with $p = 3.7{\times}10^{-6}$ and by far the highest regression coefficient. Enabling roller rotation greatly increased green density in all cases. The action of the roller compacted the powder into a tighter packing factor, thereby increasing green density. This is an indication that powder spreading and compaction are relevant for an optimization study to maximize green density. The green densities of non-compacted samples were consistently low except when the binder volume was 123 μL.

Powder that was not compacted thus required a higher amount of binder to achieve higher densities, indicating a low packing factor. Many of the non-compacted samples suffered from crumbling defects, which was reflected in their very low densities.

Some observations were made during printing that related to powder spreading and compaction. Powder spreading was less uniform with the roller rotation deactivated. Powder streaking was noted, which appeared to be due to powder clinging to the fixed roller during spreading. This could have been caused by electrostatic charge on the particles or by the wet binder from the previous layer. Moreover, printing with the roller deactivated resulted in more noticeable layer shifting. Layer shifting is a defect in which a printed BJ sample is vertically slanted in the direction of spreading. It usually occurs if the layer adhesion is too weak, which could have many causes. Binder level, layer thickness and spreading speed are all contributing factors. No layer shifting was observed in any of the compacted samples.

Layer thickness showed a probability of significance of $p = 0.0017$. It was observed that lower layer thickness on average resulted in higher green density. A lower layer thickness led to a tighter powder packing in the bed, since the roller pushes down a thinner layer of particles onto the powder bed. This is consistent with results reported in the literature [21, 68, 69]. The regression analysis resulted in a positive fit coefficient of 0.3995. This suggested that increasing layer thickness should increase green density – although the coefficient value is small. This is a counter-intuitive outcome, since studies in literature show that lower layer thickness improves green density (see Section 2.2.2). It is possible that outliers existed in the data, in particular the non-compacted samples that contained defects. The possible outlier in the data was the samples from build F (75 μm, 82.1 μL and no compaction) with a density of 17.6 $\pm$ 0.2%. When the outlier was removed and the regression rerun, the coefficient dropped to 0.1749. This indicates a reduced effect, although still positive. Since higher densities were obtained on average at lower layer thickness, this particular outcome of the regression model was not considered very reliable.

In this experiment, binder volume was more significant than layer thickness in the regression analysis, with $p = 2.7\times10^{-4}$. All densities measured at a binder volume of 82 μL were higher than those at different values in the set of compacted samples. Lower or higher values than this "middle-ground" value resulted in lower densities. This is an

indication that binder volume needs to be carefully controlled in tandem with other process parameters. This finding is consistent with indications from literature as described in Section 2.2.2, where higher densities were obtained by tailoring binder level. The binder occupies space in between and can displace the powder particles. In principle, density should increase by minimizing the binder volume to the minimum amount needed for sufficient adhesion. Insufficient binder amounts can lead to defects in samples. The non-compacted samples suffered from defects, which made them less reliable for trend analysis about binder volume effects.

Nonetheless, only the amount of liquid binder was varied in this experiment. Varying the solid-state binder content is also expected to affect density because it affects binding strength. A larger liquid binder volume can result in better dissolution of the solid-state binder and stronger adhesive bonds between metal powder particles. A balance should be reached in terms of the allowable ratio of binder constituents in the green state required to impart green strength, and at the same time avoiding issues related to cracking and void formation during debinding and sintering.

There is expected to be interplay between parameters based on the spread of the data. This is evident in the interaction terms in the regression analysis. The experimental design was not set up to capture effects above the second order. For this reason, only main and second order effects were considered. The regression analysis showed that the interaction of layer thickness and compaction was significant ($p = 5.3\times10^{-5}$). This echoes the idea that thinner layers allow tighter packing in the bed, which is also influenced by roller compaction. Thicker layers coupled with no compaction should result in consistently low densities, which is evident in Figure 3.4. Binder volume also had an interaction with compaction ($p = 4.3\times10^{-5}$). Compacted powder and a low binder volume could lead to insufficiently adhered powder. This was observed in the data in Figure 3.4. By the same token, high amounts of binder deposited over non-compacted powder resulted in higher green densities, also evident in the figure. Despite inadequate powder packing, enough binder was jetted to increase density. Layer thickness and binder volume showed the weakest interaction ($p = 0.036$). It is possible that a larger set of parameters could show clearer trends for this interaction.

Limitations of the Regression Analysis

There were limitations to the regression model. First, the model R^2 fit value of 0.913 was reasonably high, but the density data was spread out to a certain extent. The residuals plot (see Figure B.1) showed a reasonably random distribution, although the data might have contained some bias. Second, the experimental design was set up in terms of binder level, whereas analysis was performed in terms of binder volume. Since binder volume was not set up as a factorial, its statistical outcomes from the model were slightly weakened. Finally, the experiment was not set up as a complete optimization study. The range of parameters studied was practical in observing meaningful trends about the parameters for the Fe powder. This provided a useful mapping of the process parameters to define the regions where high density samples were possible. Nevertheless, a more focused selection of parameters within the region of high density samples could be used to optimize the process. Studying other parameters such as spreading speed or different roller rotation speeds could be useful for an optimization study. These parameters will be studied in more depth in Chapter 4.

3.3.3 Debinding Analysis

The binder used in this experiment burns off in an oxidizing environment. A suitable debinding temperature was determined based on thermal analysis of the binder alone. The binder in the printed samples was a combination of the solid PVA and the liquid binding agent. Most of the binder in the samples consisted of PVA by mass. The jetted liquid binder consisted of mostly water and a small amount of a glycerol-based compound. The water content was largely evaporated during drying. The glycerol compound had a decomposition temperature between 150°C and 230°C [106]. The TG curve of the binder up to 600°C is shown in Figure 3.5.

A binder sample mass of 45.97 mg was used. It was observed that mass loss started at nearly 270°C and continued until nearly 570°C, with rapid loss occurring between 270°C and roughly 360°C. These results were similar to PVA pyrolysis temperatures reported in the literature [18]. Based on this analysis, 300°C was selected as a suitable debinding

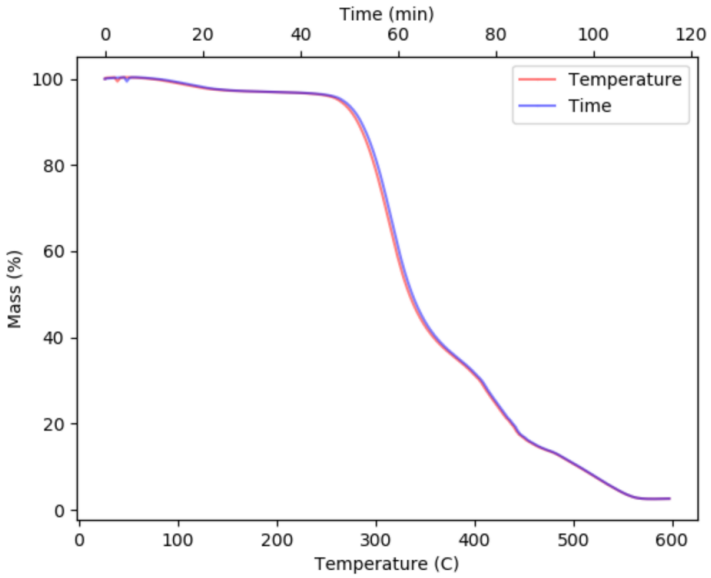


Figure 3.5: An appropriate debinding temperature was determined based on the mass loss curve of the sold-liquid binder mixture used in the Fe study.

temperature for the green samples.

Incomplete burning of the binder could result in the formation of undesired oxides. During sintering, oxide presence could affect sinter neck formation. Unburned carbon residues could lower the melting temperature of the Fe particles and melt the sample. Oxidation should ideally be avoided, but sintering in a reducing atmosphere could strip away the oxides. TG measurements of the samples during debinding were run to validate the debinding temperature and study the effect of binder content on the debinding profile. Sufficient binder removal could be judged by the shape of the sample mass loss curve. Minimal oxidation should be detected, which could be evidenced by minimal sample mass gain. Analysis of oxidation products was beyond the scope of this experiment.

Initial TG measurements were performed on samples from builds A, B and C to determine the minimum duration for debinding. The judgment for minimum duration was based on observing both a plateau in mass loss and no subsequent mass gain when the temperature elevated beyond the debinding temperature. The minimum needed debinding

duration depended solely on the binder volume in this case, considering that all samples had the same geometry. The minimum debinding durations are summarized in Table 3.3. The duration values in the table represent the isotherm at 300°C. The effect of binder volume on debinding is illustrated in Figure 3.6.

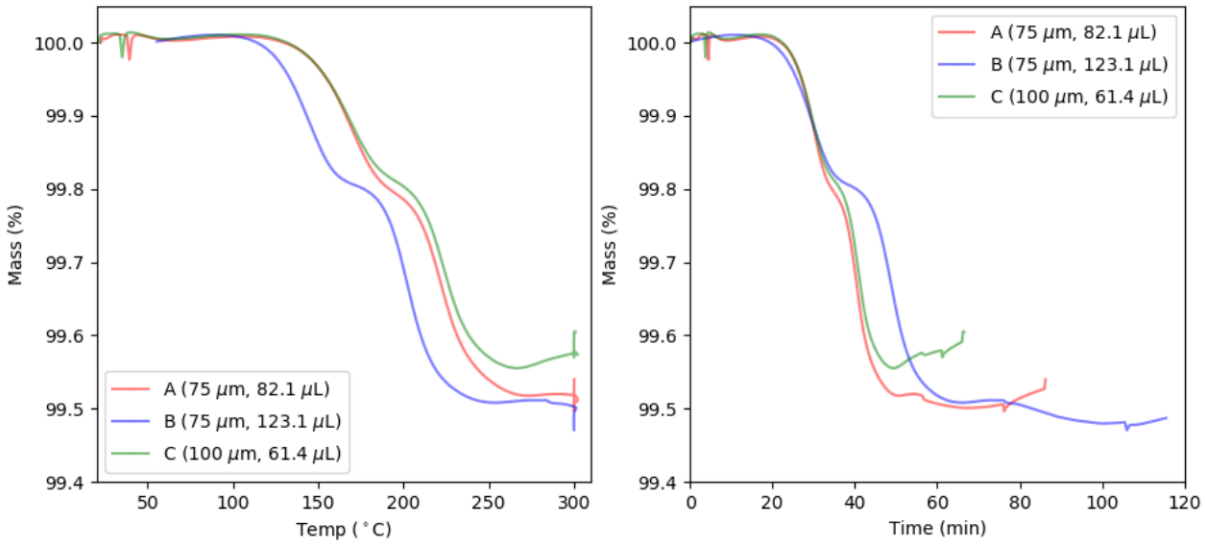


Figure 3.6: Effect of process parameters on debinding; the curves show sample mass loss against (left) temperature and (right) time, due to debinding starting from ambient temperature until the end of the 300°C isotherm.

Table 3.3: Debinding duration requirement for different samples; the differences indicated effects of process parameters on debinding duration.

Sample	Layer Thickness (μm)	Binder Volume (μL)	Debinding Duration (min)
A	75	82.1	30
B	75	123.1	40
C	100	61.4	10

The table indicates that minimum debinding duration increases with binder volume. For a given geometry, a larger number of binder molecules needed to pyrolyze, and since they could only escape from the surface of the sample, a longer time was needed for all

the binder molecules to be removed. Sample B contained 50.1% more binder than sample A and twice as much binder as sample C. However, its debinding duration needed was 33.3% longer than that for A and four times as long as that for C. The number of data points was too low to draw a meaningful conclusion, but certainly deriving a correlation through a larger dataset is of interest in future studies. Overall, the TG results showed that debinding temperature and duration should be tailored to the binder material and the amount of binder used. It is also expected that debinding should be tailored to part geometry, which can be verified through future work. An additional recommendation for testing binder residuals in the debound samples is to use Fourier-transform infrared (FTIR) spectroscopy, elemental mass spectrometry (LECO) or to examine the microstructure.

3.3.4 Solid State Sintering

As the highest green density was obtained with sample A, sintering was performed on replicates of this sample to analyze the final density. Sintered density was determined through CT analysis, and is presented in Table 3.4 for the sintering conditions studied.

Table 3.4: Sintered density values of the sample with the highest green density (sample A), under the various sintering conditions; 1390°C corresponds to 90% of the powder melting point and 1490°C corresponds to 97%.

Temperature (°C)	Isotherm Duration (hh:mm)	Density (%)
1390	02:00	64.5
1390	06:00	84.0
1490	02:00	79.1
1490	06:00	91.3

The sintered density values indicated that the sintering schedules studied were adequate in obtaining high density samples while maintaining shape fidelity. For the range of temperatures selected, density increased with both higher temperature and higher duration. Increasing temperature to 97% of the melting point promoted the formation of sinter necks across powder particles, thereby increasing the final density. The highest density obtained

was 91.3%. Overall, the results indicated that tailoring of the final density was possible by changing sintering schedule. Increasing sintering time beyond 6 hours is expected to result in higher densities based on the observed trend.

Observations of Sinter Necks

The pure Fe powder experienced sintering in the solid state. The formation of sinter necks is driven by reduction of energy in the material system on a particulate level, which in turn depends on particle size. The driving force behind sintering is dependent on crossing the activation energy barrier that promotes diffusion mass transport. Figure 3.7 shows surface SEM micrographs of sinter necks formed among particles in the sintered samples.

All micrographs were taken at the same magnification. It was observed that sinter necking was more developed in the samples sintered at 1490°C. At 1390°C, the shape of the sinter necks indicated that grain boundary diffusion was the dominant mechanism [2] and that sintering was active in the intermediate stage (refer to Figure 2.3). The effect of temperature was stronger than that of duration. The difference in sinter neck shape between sintering at 1390°C and 1490°C is more drastic than that between sintering at 2 hours and 6 hours. This is consistent with the theoretical understanding of SSS theory [1].

Sintering at 1490°C for 6 hours resulted in seemingly wide sinter necks among the particles. The geometrical features of the irregular Fe particles were largely smoothed and pores appeared to have begun closing. Spots of a darker shade were visible in the images, which could be a different phase, due to residual oxides or trace alloying elements. Both grain boundary diffusion and volume diffusion were likely active due to the high temperature and the shape of the sinter necks. As the final density was just below 92%, it is expected that sintering occurred just at the start of the final stage or at the end of the intermediate stage.

Calculation of the activation energies would be of interest in future studies, which could be done through dilatometry measurements, as described in Section 2.4. Quantifying the apparent activation energies could be used to better understand the progress of sintering for the Fe powder.

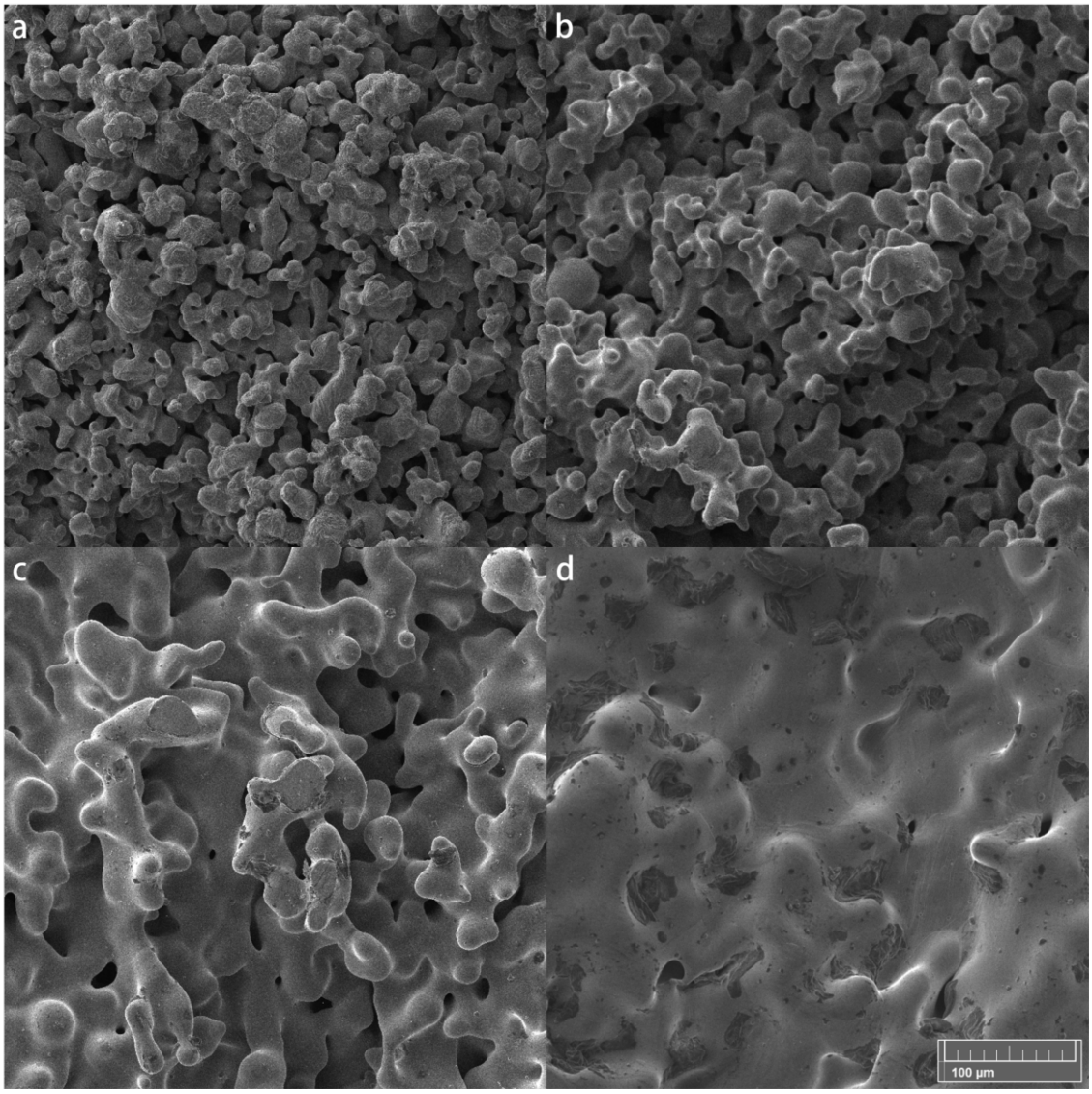


Figure 3.7: Sinter neck formation and different stages of sintering for the different conditions: (a) 1390°C, 2 hours; (b) 1390°C, 6 hours; (c) 1490°C, 2 hours; (d) 1490°C, 6 hours.

Spatial Porosity in the Sintered Sample

A consistent voxel size of 5.5 μm was used to capture CT images for both green and sintered samples. Segmentation of the solid fraction was first conducted through the Otsu algorithm

to establish a standardized threshold. Subsequently, the threshold was manually adjusted to capture a more accurate segment based on visual inspection of the images before and after segmentation. This ensured that the segment matched the solid and void fractions visible in the images.

In all samples, the images were resliced to an orthogonal view that could be flattened by using the Minimum Intensity Projection (MinIP) method to visualize the distribution of low density regions in the sample. The spatial porosity distribution was then visually aligned with the relative density data. The method projects the voxel with the lowest attenuation value onto a single 2D image for the entire data set. The binder was not visible in any of the grayscale images due to its extremely low attenuation value in comparison to Fe. Slice-wise relative density calculation of sample A before and after sintering is shown in Figure 3.8. The sintered sample density profile and MinIP were rescaled in the z-direction only for alignment.

The relative density profiles of the green and sintered (1490°C, 6 hours) samples are shown in Figure 3.8(a). The profiles revealed the porosity distribution in the build direction (z-axis). In the green sample, porosity distribution varied in the build direction. The variation was likely an outcome of powder stacking or compaction, where layers at the bottom of the sample experienced more packing under the weight of the powder and binder above. The overall lower regions (along the z-axis) of the green sample exhibited higher local densities approaching 65%, while in the central regions local density varied between approximately 40% and 55%. At the top of the sample, local density was at its lowest value. This trend was indicative of a powder compaction effect, either due to the roller or gravity. The repeated motion of the spreader in the BJ system compacted the powder bed; topmost layers received less compaction, resulting in reduced local density. To some extent, pore distribution was least concentrated near the central region of the sintered sample. A large collection of pores near the bottom of the sintered sample indicated a layer defect, shown by the dark "gash" in Figure 3.8(c) and the drop in local density in Figure 3.8(a). The defect was likely due to a manufacturing process error.

A periodicity effect in density variation was noted in the green sample. Such an effect was previously observed for BJ samples in literature [44]. The effect could be seen as vertical bands in Figure 3.8(b) and (e), with the bands being almost equivalent to the

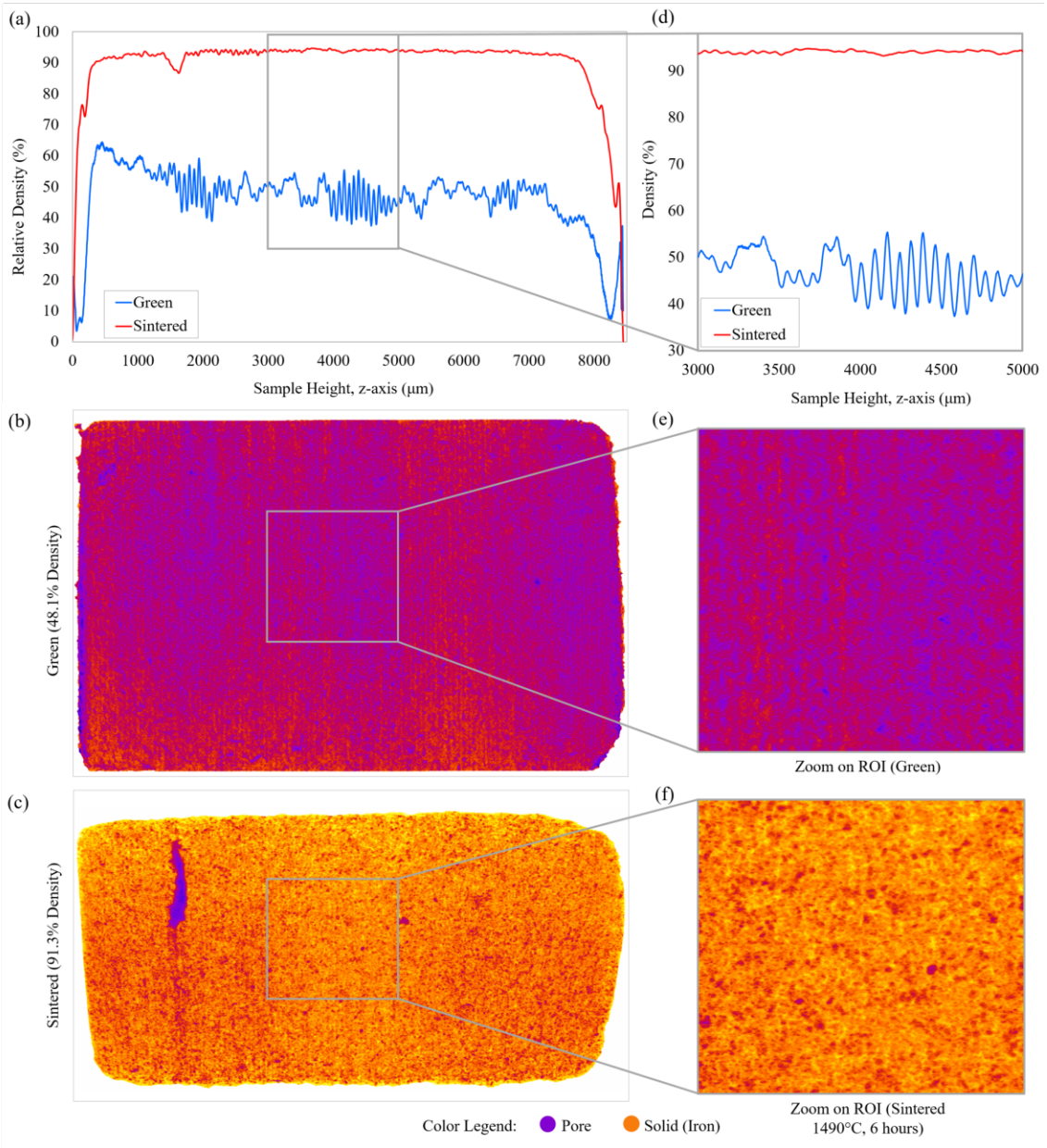


Figure 3.8: (a) Comparison of relative density profiles along sample height across green and sintered (1490°C, 6 hours) sample A; (b) minimum intensity projection of the CT scan showing pore distribution for the green and (c) sintered sample; (d) a region of interest (ROI) 2 mm in length; (e) minimum intensity projection of the ROI for the green and (f) sintered sample.

layer thickness. Regions of high variability seen in Figure 3.8(a) and (d) occurred along the z-axis: 1347 μm to 2320 μm, and 3926 μm to 4921 μm. The bands corresponded to a periodicity of 75.7 $\pm$ 5.7 μm, which reflected the 75 μm layer thickness of this sample. This suggested that particle packing across a layer in the xy plane was tighter than in between layers in the z-axis.

The high variation was mostly dampened in the sintered samples. This was evident by the significant reduction of the vertical bands in Figure 3.8(c) and (f). This is an important outcome of sintering that was not observed in previous work [44]. The absence of variability and periodicity artifacts was due to the aggressive sintering that densified the sample from 49.7% to 91.3%. For comparison, this effect is discussed for other sintered densities further on in this section. This finding implied that imperfections and irregularities in green samples could be overcome if sintered to a high enough density. This could be an important finding on the effects of sintering, particularly relevant in an industrial context.

Porosity also varied in the layer-wise (radial) direction. This suggested a build orientation effect. In the green sample, a larger pore distribution was present at one side of the sample (top of Figure 3.8(b)). This pattern was echoed to some extent in the sintered sample, but was reduced after sintering. Powder spreading could lead to preferential packing in the build bed, where powder at the end of the bed exhibited lower packing. This observation was previously noted in literature [107]. It could also be an effect of the spreading mechanism. More detailed analysis of this effect could not be conducted due to the symmetry of the samples and lack of a feature that identified build orientation. This phenomenon is of interest and should be studied in more depth. Generally, it is of interest to mathematically describe a relationship between spreading parameters and powder packing, as well as the resultant green density. This idea will be further explored in Chapter 4.

A comparison was drawn across the four sintering schedules in terms of density profile. The density profiles are plotted in Figure 3.9. Variability in the density profile was observed in the cases of sintering at 1390°C, and to a much lesser extent at 1490°C. The profile of (1390°C, 2 hours) showed high variability in local density over small regions as well as over the entire sample height. This bore similarity to the green sample profile, except that local density was highest near the sample center and lowest at the bottom. The profiles of

(1390°C, 6 hours) and (1490°C, 2 hours) also showed some variability in local density, which was attributed to periodic regions of poorer powder packing and thus poorer sinter neck formation. This trend was mostly not observed in the (1490°C, 6 hours) profile. Variability and periodicity effects became increasingly dampened with more aggressive sintering. The data showed that sintering temperature was more influential than duration in eliminating these effects. The curve of 1490°C in Figure 3.9 illustrated this idea.

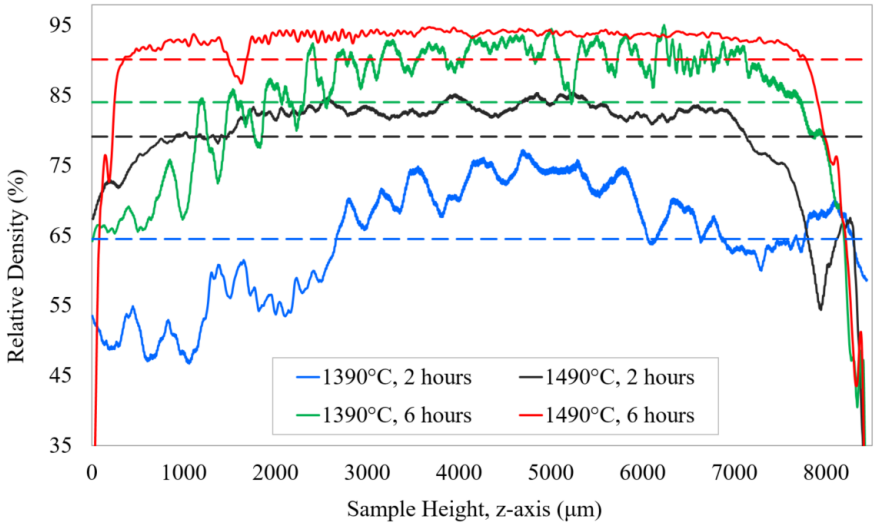


Figure 3.9: Relative density profile comparison across sintering schedules (average density value shown in dotted lines).

Sintering at 1390°C for 6 hours produced a higher density of 84.0% compared to sintering at 1490°C for 2 hours that produced 79.1% density (refer to Table 3.4). Although lower temperature and longer duration produced a higher mean density, variability and periodicity effects were still pronounced. Sintering at the higher temperature therefore resulted in more uniform densification with fewer irregularities. This is consistent with sintering thermodynamics [1], where temperature affects the diffusion coefficient in volume and grain boundary diffusion (Equation 2.4). From a practicality perspective, sintering at temperatures as high as 97% of the powder melting temperature is difficult, because many industrial furnaces are not designed for such high temperatures. Future work could include studying the feasibility of achieving $>$ 90% density at lower temperatures and

adding sintering aids to lower the melting temperature [51].

Tailoring sintering temperature and duration further could result in higher densities. For these samples, dilatometry measurements were not possible due to availability constraints, and the MSC was not constructed. Construction of the MSC would allow prediction of densification behavior with respect to the time-temperature profile.

Pore Morphology

The distribution of the number of pores is illustrated against pore volume in Figure 3.10(a) and against pore sphericity in Figure 3.10(b) for green and sintered sample A. Pore sphericity refers to the aspect ratio of the pores, where a value of 1 indicates a perfect sphere. The pore count was normalized against the total number of pores detected.

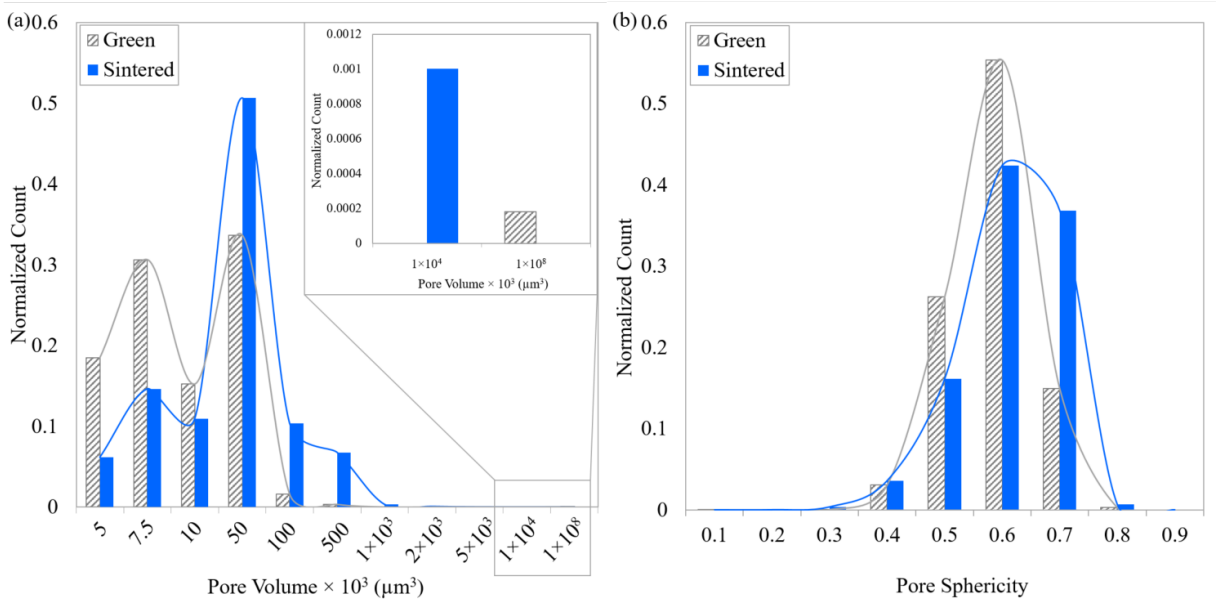


Figure 3.10: Histograms of pore count against (a) pore volume, and (b) pore sphericity for green and sintered (91.3% density), evaluated via CT image processing. Pore volumes greater than 1×10^{11} μm^3 indicated an interconnected pore network that was detected only in the green sample.

The number of isolated pores was higher in sintered sample than in green sample, but the cumulative pore volume was overall smaller in the sintered sample. Interconnected porosity was detected in the green sample, denoted by a pore volume greater than 1×10^{11} μm^3. Interconnected porosity was captured as a single, extremely large pore in the histogram. It was not detected in the sintered sample, as pores became isolated and started closing after sintering to a high density. This was more or less consistent with sintering theory [1], where the general threshold for overcoming interconnected porosity is 92%. In general, the distribution of pore volumes was narrower after sintering, particularly in the presence of interconnected porosity that dominated the volume (but not count) of pores in the green sample.

Sphericity of the pores increased after sintering and approaches 1, with the majority of pores attaining values 0.6 and 0.7 with pore closure and spheroidization [1]. 3D renders from the CT images of the sintered sample are presented, highlighting pore distribution by volume in Figure 3.11(a) and pore sphericity distribution in Figure 3.11(b).

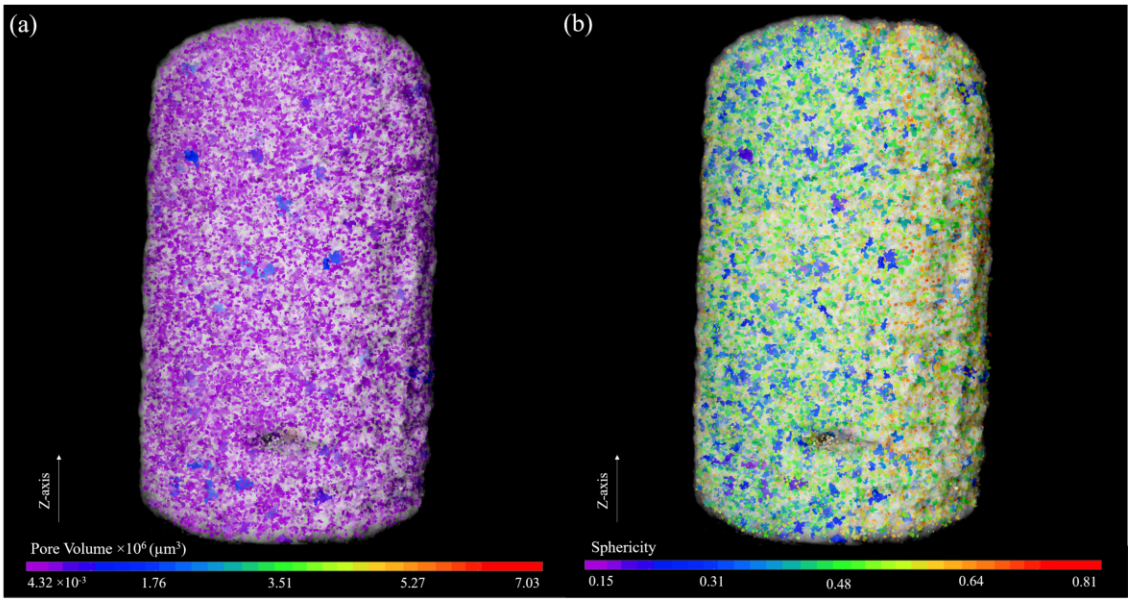


Figure 3.11: Three-dimensional rendering of μCT scans of sintered sample A (1490°C, 6 h) showing the distributions of (a) pore volume and (b) pore sphericity.

Dimensional Shrinkage

The dimensional shrinkage of sample A was quantified by comparing the major and minor diameters a and b and height h before and after sintering. Maximum shrinkage occurred in the case of sintering at 1490°C for 6 hours, with a height shrinkage of 24.8 ± 3.5% and diametrical shrinkages of 25.3 ± 2.8% and 24.2 ± 2.1% respectively. A photographic representation of sample A in the green state and in the various states of sintering is shown in Figure 3.12. Shrinkage trends with respect to sintering temperature and time are illustrated in Figure 3.13.

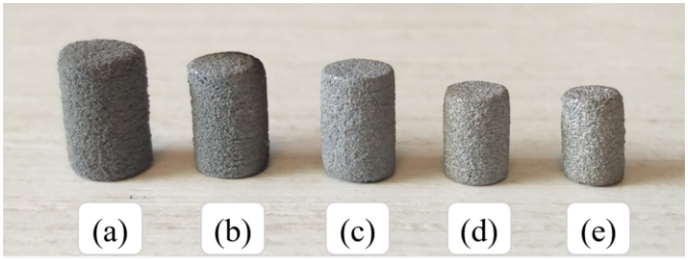


Figure 3.12: Dimensional shrinkage due to sintering. Sample A in (a) green state, and sintered at (b) 1390°C, 2 hours, (c) 1390°C, 6 hours, (d) 1490°C, 2 hours and (e) 1490°C, 6 hours. The extent of dimensional shrinkage correlated with density.

In general, larger shrinkage was associated with sintering temperature. Increasing the sintering temperature incurred higher shrinkage than did increasing the sintering time. Although sintering at 1390°C for 6 hours produced a higher average density than at 1490°C for 2 hours, shrinkage was higher at the higher temperature. This could be attributed to the significant variability across sample height for 1390°C and 6 hours (refer to Figure 3.9). The measurements captured shrinkage both at the surface and in the core of the samples, which could have been non-uniform. This was a possible contributor to the observation that shrinkage correlated with temperature rather than with density.

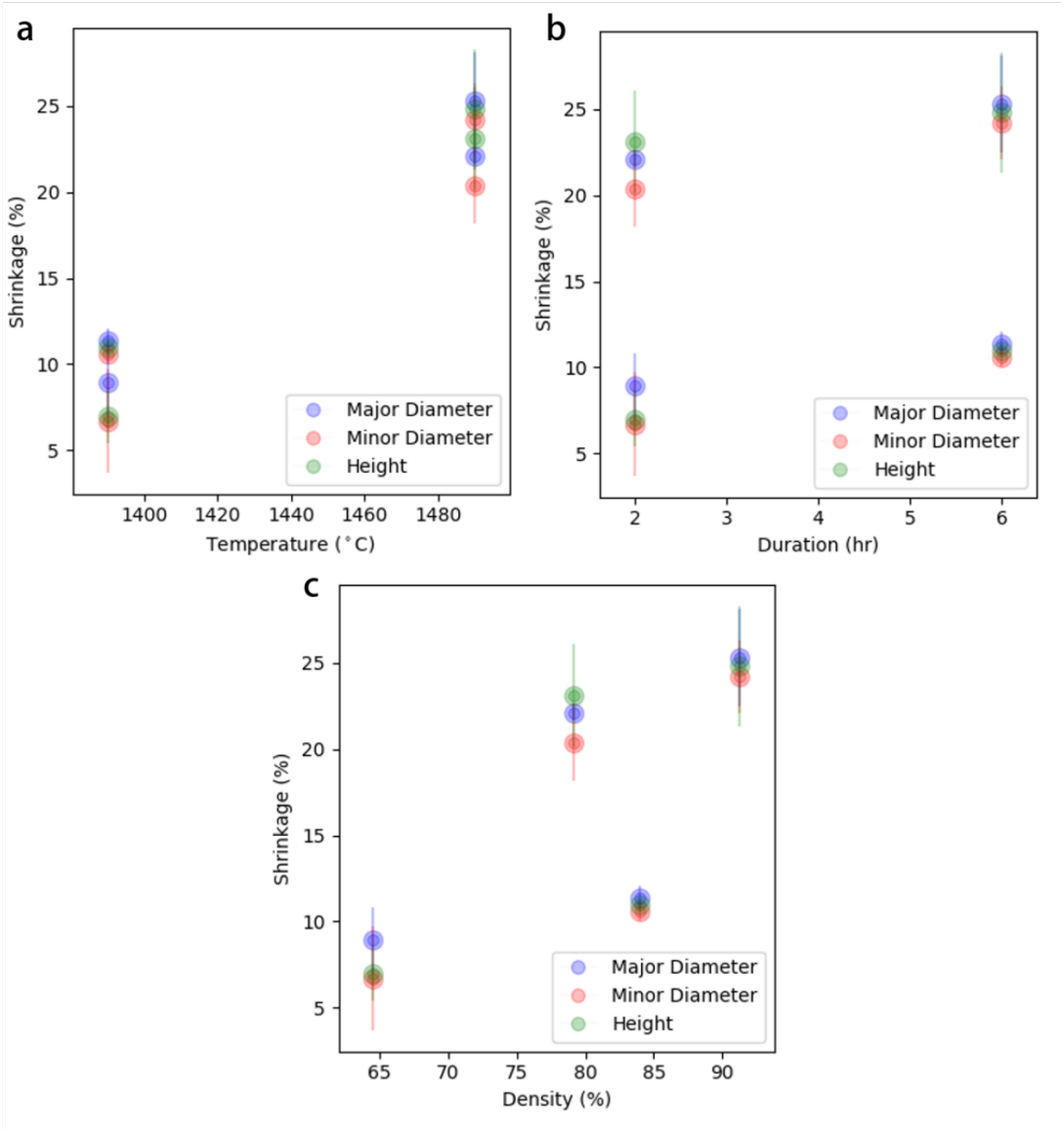


Figure 3.13: Shrinkage due to sintering with respect to (a) temperature, (b) duration and (c) density for sample A.

No meaningful trend could be extracted from the shrinkage analysis about shrinkage in build direction (sample height h) compared to the horizontal direction (sample diameters a and b). A more expansive experimental design could be created with various sample

geometries to reveal trends about anisotropy or pore collapse in various directions. Other studies on BJ of metals typically show shrinkage values of 2-32%, depending on powder, process and post-process parameters [37, 47, 50, 81, 108].

Radial uniformity in shrinkage was quantified by comparing shrinkage of the major and minor diameters. Shrinkage in the major and minor diameters varied by 5% ± 33%, where sintering at 1490°C for 6 hours gave the best uniformity. Vertical uniformity in shrinkage was qualified by visual inspection of the samples. Shrinkage was generally uniform in the vertical direction for all sintering schedules, notwithstanding the dimensional accuracy of the BJ process itself.

Consistency in shrinkage was assessed across multiple samples undergoing identical sintering schedules. This was quantified through the standard deviation in shrinkage. The deviation is consistently low when sintering at 1390°C for 6 hours. A predictable shrinkage is useful for industrial processes, because it could be compensated for by design. A more comprehensive experimental study could be designed to better assess shrinkage consistency in future research.

3.4 Summary and Outcomes

In this chapter, samples of pure Fe were fabricated through BJ and sintered to high densities. The effects of layer thickness, binder volume and powder compaction were studied for the material and process maps were charted for achieving high green densities. Debinding was studied with respect to binder volume, and sintering temperature and duration were varied to produce high density final samples.

Green densities of up to 49.7% were possible with the parameter values selected. A more expansive optimization study could result in higher densities and clearer parameter trends, and will be the scope of Chapter 4. Tailoring of the binder volume requires special attention because of the seemingly complex effect on green density. Deriving a relationship between spreading parameters and powder packing would be useful for BJ research, especially if studied alongside binder volume and their resultant effect on green density.

Tailoring the debinding conditions is an important step in the work flow. Debinding duration varied with the amount of binder present in the samples. Selecting the appropriate debinding temperature depended on the binder material, with careful attention to unwanted oxidation in the Fe powder itself. Debinding strategies for BJ samples is a topic of research interest, which can be tackled further in future work.

Sintered samples of up to 91.3% density were achieved for the material. Tailoring sintering conditions could allow control over final densities, in particular with the construction of the MSC, which was not possible for these samples. Porosity analysis through CT imaging revealed artifacts as a result of powder spreading and compaction. Variability in green porosity distribution was largely dampened after sintering at high temperatures. The high temperature accelerated densification by grain boundary or volume diffusion, cancelling many of the powder packing artifacts and irregularities. This observation could be useful in an industrial context. Finally, shrinkage was impacted most heavily by sintering temperature, which was consistent with the theoretical understanding of sintering.

Within the larger context of BJ research, the contribution of this chapter was to demonstrate that unaided sintering of BJ samples made from irregular Fe powder was successful in reaching densities above 90%. This is a useful result for water-atomized powder manufacturers who target the PM industry. Tailoring the sintering conditions could overcome some of the inherent powder packing limitations of the powder morphology. Moreover, this study offers considerations into the debinding profile for BJ samples, which is a topic not yet fully explored in literature. A large part of the conclusions of this chapter were directly applicable to the Fe powder manufacturer Rio Tinto. The larger motivation is to advance industrial adoption of BJ.

In the next chapter, an optimization study will be demonstrated to draw more meaningful trends on the effects of key process parameters on green density. The study will derive an empirical relationship between spreading parameters and packing factor, and subsequently capture their effects on green density. Sintering of the powder in the liquid phase will be studied with the goal of achieving high final densities.

Chapter 4

Binder Jetting and Sintering of Fe-Si

4.1 Motivation

Fe-Si powder has direct applications in the industry for which BJ can be useful. Typical applications of Fe-Si include soft magnetic materials and electric machinery. Many soft magnetic components are made by using PM, with target component densities typically in the range of 95-98% of the wrought material [104]. This density range renders BJ a suitable technology for such applications. Although pure Fe is a common candidate for soft magnetic applications, the addition of Si increases electrical conductivity of Fe, which could be desired depending on the application. Other examples of Fe-Si in the PM domain include anti-lock brake sensor rings for automobiles [104].

Further applications of Fe-Si include rotors or stators for electric generators or motors [109]. For laminated core materials, sheets of 100 μm thickness are typical [109]. The fabrication of such sheets is in the range of possible layer thicknesses for BJ. Some examples of AM of Fe-Si exist in the literature, although predominantly with laser AM processes [110].

This chapter is concerned with optimizing BJ process parameters to maximize green density for Fe-Si powder, as an extension to the work done on BJ process mapping for the Fe powder. In this context, mathematical expressions were derived to describe the relationship

between process parameters, the non-dimensional packing factor and binder saturation for the material used. Following green density optimization, a debinding schedule was developed for the binder system. Finally, a thermal schedule was developed for sintering in the liquid phase, and the sintered sample outcomes were assessed. A framework was setup for conducting dilatometry measurements and constructing the MSC for the material. The objectives of this chapter are as follows:

1. Derive empirical expressions that relate key process parameters to packing factor and green density; and
2. Conduct sintering in the liquid phase for the material to obtain high densities, and setup the framework for development of the MSC.

4.2 Experimental Methods

4.2.1 Metal Powder Material

The powder material used in this chapter was gas-atomized Fe-Si (GKN-Höganäs, Cinnaminson, NJ) with a composition of 3.42% Si, 0.043% O, 0.01% C, 0.002% S and 0.001% N. The powder size distribution was 20-51 μm with a D_{50} of 32 μm. The supplied tap density ρ_{tap} of the powder was 57.2%. Imaging of the powder was conducted through SEM (Zeiss Ultra Plus, Toronto, ON) to observe its morphology and surface quality. Imaging was performed under a vacuum of 9.85×10^{-7} mbar.

4.2.2 Green Density Optimization Experimental Design

One of the aims of this chapter was to experimentally optimize the BJ process for green density. The objective function in this optimization study was therefore green density. An experimental design was developed to conduct the optimization work. The experimental procedure tackled in the previous chapter served as a screening study for the parameters of interest. All of layer thickness, powder compaction and binder amount were found to be

significant variables. As such, the optimization work performed in this chapter included these parameters and added a new parameter: linear spreading speed. Information from literature as discussed in Section 2.2.2 suggested its impact on green density.

In this chapter, four process parameters were varied according to a half-factorial design with two center points ($2^{4-1}+2$). The half-factorial design was chosen over the full factorial in order to reduce the number of experiments. The two center points were added in order to make the design expandable to a central composite design, if necessary. One motivation for this design is to enable adequate regression analysis about significance and interaction of parameters with a minimum number of builds. Although other optimization designs such as Taguchi's method were previously used [68, 70, 71], this method was chosen in order to capture an experimental fit function. This approach would better describe the influence of the parameters on green density.

The total number of builds for the optimization study was 10. For experimental robustness, each build contained 16 replicates of cylindrical samples, measuring 5.8 mm in diameter and 10 mm in height. In this experimental design, layer thickness was considered as a non-dimensional parameter. Layer thickness was observed to have a relationship with the powder size range [21, 63], both of which have an influence on powder packing, as shown by several studies. Therefore, layer thickness was normalized by the D_{50} value of the PSD to produce more meaningful trends in the optimization work, in particular with regards to the packing factor. The experimental design table is presented in Table 4.1. In the table, L^* denotes layer thickness normalized by the D_{50} value of the PSD, v denotes linear spreading speed (mm/s), ω denotes the roller rotational speed or compaction speed (rpm) and S denotes binder saturation (%). Saturation in this case was defined by Equation 2.1 – it therefore described binder amount in the whole sample and was not dependent on the number of layers.

Green Sample Fabrication

The samples fabricated for this study were produced by using a commercial ExOne M-Flex system (the ExOne Company, North Huntington, PA). The system is a production-scale machine with a standard build envelope of 400 mm × 250 mm × 250 mm and is designed

Table 4.1: Half-factorial with two center points design of experiments for optimization. The process parameter values are displayed in parentheses.

Build	L^*	v (mm/s)	ω (rpm)	S (%)
1	-1 (1.5)	-1 (6)	-1 (100)	-1 (67.5)
2	1 (2)	1 (10)	-1 (100)	-1 (67.5)
3	1 (2)	-1 (6)	1 (200)	-1 (67.5)
4	-1 (1.5)	1 (10)	1 (200)	-1 (67.5)
5	1 (2)	-1 (6)	-1 (100)	1 (82.5)
6	-1 (1.5)	1 (10)	-1 (100)	1 (82.5)
7	-1 (1.5)	-1 (6)	1 (200)	1 (82.5)
8	1 (2)	1 (10)	1 (200)	1 (82.5)
9	0 (1.75)	0 (8)	0 (150)	0 (75.0)
10	0 (1.75)	0 (8)	0 (150)	0 (75.0)

to handle metals or ceramics. The machine uses a hopper-type recoating mechanism to dispense powder onto the build area. Powder is contained in a chamber that moves across the build bed every layer and dispenses powder by using a motorized oscillator to shake and release powder. The machine uses a steel roller to then uniformly spread the deposited powder over the entire build area.

The machine uses a high-resolution printhead to jet the binder. The printhead relies on piezoelectrically actuated nozzles to release the binder. The average droplet size is 80 pL. The printhead consists of four columns of 256 independently activated nozzles, forming a total of 1,024 nozzles. The printhead resolution is 63.5 μm in x and y. The machine has a minimum recommended build resolution of 50 μm in z, but finer vertical resolution is possible.

A reduced build volume (RBV) insert was designed and fabricated in order to reduce the total available bed volume. The RBV was installed to reduce powder consumption given the large number of experiments. The modified build bed was reduced to 90 mm $\times$ 90 mm $\times$ 150 mm. The RBV, shown in Figure 4.1, was designed to mimic the standard machine design, and therefore did not introduce any new variables to the process.

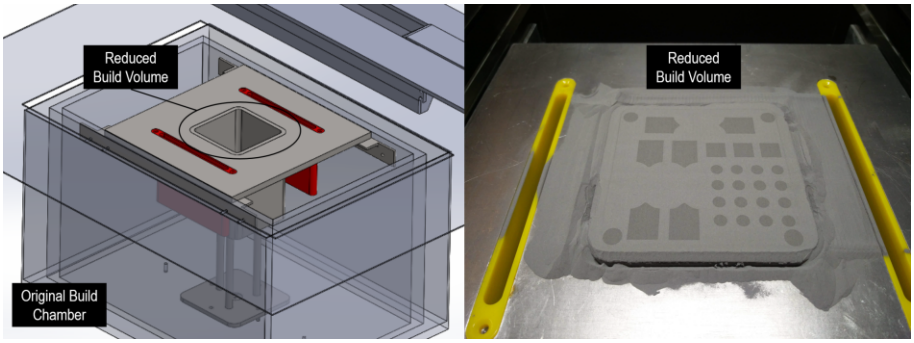


Figure 4.1: A reduced-size build volume insert was used in the ExOne system during green sample production. The insert was used only to reduce powder consumption and did not affect the build quality or sequence.

Curing

The binder system used in the ExOne M-Flex only relies on an aqueous binder. A solid-state binder was not needed. The standard manufacturing process for the machine system used involves a curing step. The entire build chamber was extracted out of the machine and placed in a curing oven (JPW Model ST333A, Trout Run, PA). Curing proceeded for a duration of 12 hours, where temperature was increased from room temperature up to 180°C and held until the end of the duration. The elevated temperature allowed the binder to cross-link and harden, increasing the strength of the green samples. This curing method was the recommended standard procedure by the ExOne Company. Upon completion of the curing step, the samples were removed from the build bed and depowdered by using a soft brush.

4.2.3 CT Analytics for Green Samples

Determination of the green sample density for all manufactured samples was completed in two steps. The process was generally similar to that for Fe in the previous chapter. A single sample out of each treatment was imaged via CT at high resolution and the data was reconstructed to calculate density. A 2 μm voxel size CT scan was used to capture an

internal, cylindrical ROI that is 2 mm in diameter and 2 mm in height. Imaging of all the samples was completed at approximately the same physical location (center) of the sample, therefore producing approximately the same ROI for all samples. The reconstructed image was processed (Dragonfly 3.0, Object Research Systems Inc., Montréal, QC) with a non-local means filter and a bilateral filter. The image was segmented by using the Otsu algorithm with manual threshold adjustment to extract a binary segment of the solid powder fraction of the sample. Density was calculated by dividing the total number of voxels in the segmented image by the total number of voxels in the unsegmented image. The high-resolution scan produced an accurate estimate of the density. The size of the ROI captured 30-40 layers and was therefore deemed to be representative of the whole sample.

In each treatment, the dimensions and mass of all the samples (including the one for imaging) were measured via calipers (Mitutoyo Absolute Digimatic Caliper, Mississauga, ON) and a mass balance (Sartorius Secura 225D, Göttingen, Germany). A rough estimate of the density was calculated using these measurements as described in Equation 3.1. Calipers measurements for each of the variables were taken for averaging at consistent locations in all samples. The calipers density estimate was then correlated with the CT density as a reference. This then allowed determination of density for all other samples in that build based on calipers density and the reference CT density value.

4.2.4 Microscopy Analysis for Sintered Samples

Calculation of density through CT imaging was found to be unreliable for the sintered Fe-Si samples. Reconstruction of the CT images and subsequent Laser Confocal Microscopy (LCM) imaging revealed that the CT detector had difficulty in differentiating between pores (air) and Si-rich regions. (More discussion on the Si-rich regions is presented later in the chapter.) Both air and Si have low X-ray attenuation values compared to Fe, which made their intensity peaks difficult to resolve. By contrast, LCM gives a height profile of the imaged region with an accuracy of 2–0.05 μm depending on the magnification. Therefore with LCM, it was possible to correctly segment the images and calculate the density level. Samples were mounted in polymer resin, sectioned, polished and subsequently imaged via LCM (Keyence VK-X250, Osaka, Japan). LCM imaging also captured optical images in

addition to laser images. The density calculation was performed in ImageJ (Fiji, version 1.51) through manual segmentation. The images used to calculate density spanned a region of nearly 5 mm $\times$ 4 mm (at 2 μm depth or z-resolution) at the center of the samples. The density values were also compared with higher magnification images at 0.5-0.05 μm z-resolution to corroborate the calculated values. Three replicates of each heat treatment were analyzed for density determination.

There was a drawback to determining density through LCM instead of CT imaging. Although the LCM images clearly showed the level of porosity, the calculations were based on images of single cross-section of each sample. It was assumed that the section was representative of the entire sample. CT imaging by contrast captures a complete volume. The LCM images segmentation in ImageJ was compared to "automated" segmentation via a local adaptive threshold method in custom scripts and produced very similar results.

SEM imaging of the sectioned samples was performed (Tescan Vega3 SEM, Warrendale, PA) and Energy Dispersive Spectroscopy (EDS) was performed by using the same instrument. The EDS analysis was used to identify the distribution of elements in the sample and its relation to sinter necking. A voltage of 10 kV was used for SEM imaging, and 20 kV was used for EDS measurements.

4.2.5 Debinding

The debinding schedule was developed by using TG (TA Instruments Q500 TGA, Grimsby, ON) on a specimen measuring 47.26 mg in a high-purity inert N_2 atmosphere. This gas was used instead of a reducing atmosphere due to gas use restrictions for the equipment. The TG measurement was performed on a specimen from the green sample with the highest green density. The commercial ExOne binder consisted of proprietary constituents. A TG measurement (Netzsch Jupiter ST 449 F1, Burlington, MA) on the cured binder alone was also completed. For the purpose of this chapter, a single, sufficient isotherm duration was determined in order to fully debind the samples. The debinding duration was already determined to depend on the amount of binder in Section 3.3.3. A more expansive study could capture a model fit with enough data points. This was not pursued in this chapter due to time constraints. An acceptable debinding temperature and duration were

determined from the TG results to ensure minimal binder residue before sintering. The actual debinding of the BJ sample set of the highest green density was completed in a tube furnace (Carbolite 1200 Series, UK) under a reducing 5% H_2-Ar atmosphere.

4.2.6 Sintering

Development of the sintering profile required knowledge of the solidus temperature of the Fe-Si alloy. A phase diagram of Fe-Si is presented in Figure 4.2. The alloy composition contained 3.42% Si by weight. For this composition, the phase diagram showed that a liquid phase would start to form at approximately 1485°C and the liquidus point would crossed at approximately 1510°C.

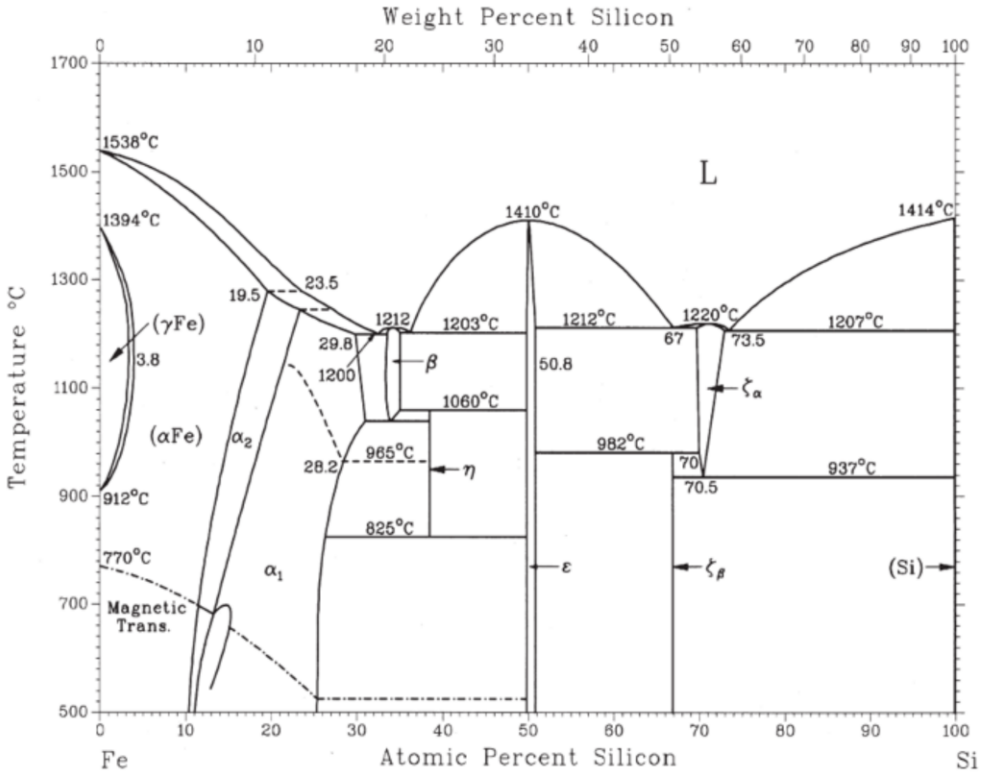


Figure 4.2: Phase diagram of the Fe-Si alloy [9].

The phase diagram provided a reference for selecting sintering temperatures. However, the Fe-Si alloy contained other alloying elements that could slightly shift the melting range. In order to accurately capture the melting behavior of the alloy, a Differential Scanning Caloritmetry (DSC) measurement was performed (Netzsch Jupiter ST 449 F1, Burlington, MA) on a BJ sample from the highest green density sample set (29.60 mg, 20°C/min) under Ar gas. The gas was selected for the DSC measurement based on the availability and restrictions for use. The measurement helped in estimating the solidus and liquidus temperatures.

The DSC was expected to capture any effects of potential carbon residue from the binder that could affect the melting behavior. The DSC curve and its first derivative (DDSC) are shown in Figure 4.3 and were used as the basis for temperature selection for sintering.

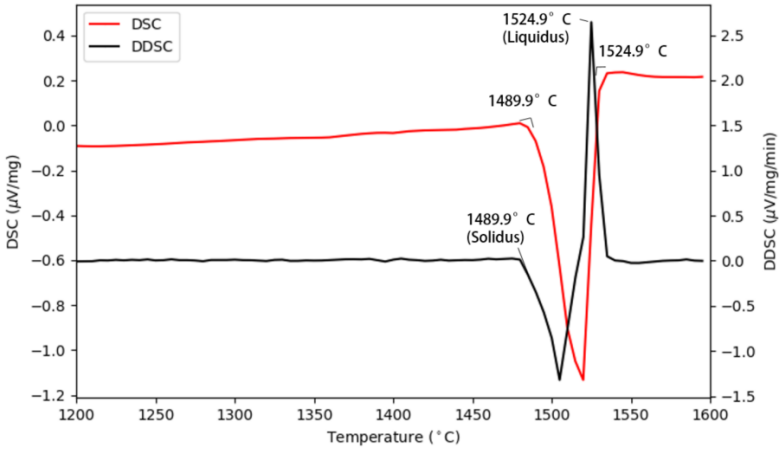


Figure 4.3: DSC and DDSC curves for the Fe-Si BJ sample; the melting signature was used to determine the appropriate temperature for liquid phase sintering.

The measurements showed a solidus temperature of 1484.9°C and a liquidus temperature of 1524.9°C. This range slightly differed from the phase diagram prediction. This is not atypical of pre-alloyed powders, since the effective solidus onset temperature of the alloy is affected by non-equilibrium particle solidification during atomization, which will

affect how closely it follows the phase diagram [93]. The presence of alloying elements (C, O, N) could also contribute to the discrepancy.

Sintering of samples was conducted in a high-temperature furnace (Nabertherm VHT 40/18 KE, Lilienthal, Germany). Sintering was run on the debound samples, according to the schedule shown in Table 4.2. A sintering temperature of 1470°C was used. Initial sintering trials at 1490°C resulted in complete melting of the samples. For this reason, a lower sintering temperature was selected. This will be discussed in more detail in Section 4.3.4. Two isotherm durations were used: 15 min and 1 hour. The isotherm durations, heating rates and atmospheres are shown in the table. The selection of the two isotherm durations was based on typical PM protocols for steel alloys [7, 93]. Although sintering in a vacuum is ideal for LPS to prevent trapped gas porosity [79], it was not possible to reach the maximum temperature in vacuum due to furnace limitations. For this reason, high-purity Ar gas was used at the maximum temperature.

Table 4.2: Liquid phase sintering schedules, showing sintering temperatures, isotherm durations, heating rates and atmospheres used. Two isotherm durations were studied: 15 min and 1 hour.

Start T (°C)	End T (°C)	Isotherm (hh:mm)	Heating Rate (°C/min)	Atmosphere
25	300	-	5	Vacuum
300	300	00:05	-	Vacuum
300	1000	-	20	Vacuum
1000	1000	00:10	-	Ar
1000	1470	-	5	Ar
1470	1470	00:15 or 01:00	-	Ar
1470	25	-	20	Ar

4.2.7 Dilatometry and the MSC

This section describes the methodology for producing the MSC, including measurements of dilatometry. The measurement results and the MSC will be part of future work.

An optical dilatometer (Fraunhofer ISC Model TOM-AC, Wertheim-Bronnbach, Germany) will be used to measure *in situ* shrinkage during sintering. The dilatometer consists of a high-temperature furnace capable of inert or reducing atmospheres and a set of CMOS cameras that capture the contour of the samples in the xz plane and thus measure shrinkage. The camera images are analyzed in real-time by a proprietary software by the manufacturer. The schedule for dilatometry is summarized in Table 4.3. The schedule aims to capture LPS in the samples. The schedule can be modified or expanded to encompass different sintering temperatures or durations, depending on initial results. The BJ Fe-Si samples were printed to fit in the dilatometer sample holder. The samples will be debound separately before dilatometry.

Table 4.3: Dilatometry schedule for liquid phase sintering of the Fe-Si samples.

Start T (°C)	End T (°C)	Isotherm (hh:mm)	Heating Rate (°C/min)	Atmosphere
25	750	-	20	5% H_2-Ar
750	1470	-	1 or 3 or 5	5% H_2-Ar
1470	1470	01:00	-	5% H_2-Ar
1470	25	-	20	5% H_2-Ar

The methodology for developing the MSC will follow the process that was discussed in Chapter 2. Specifically, the studies by Bollina et al. [7] and Wheat [44] will be used as supporting guidelines. The code for determining the activation energy Q and plotting the MSC has been developed by Wheat [44], and can be used for the Fe-Si samples with some modifications. The modifications will be related to LPS and the incorporation of a multi-segment sigmoid fit model, where the coefficients of the fit function will be changed after initiation of the liquid phase. The work by Bollina et al. [7] provides an excellent reference for this modification.

4.3 Results

4.3.1 Metal Powder Characteristics

An SEM image is shown in Figure 4.4. The particles appeared generally spherical with smooth surfaces. Some of the particles had an elongated shape or appeared irregular, which was most likely an outcome of the powder atomization process. Initial observations of the powder revealed good flow. The PSD of 20-51 μm is within the typical range for BJ. The D_{50} value of 32 μm influenced the selection of layer thickness in the optimization study. The layer thickness was normalized by the D_{50} value, as described in Section 4.2.2. The resultant layer thickness values spanned a range of 49-65 μm, which were feasible in the BJ system.

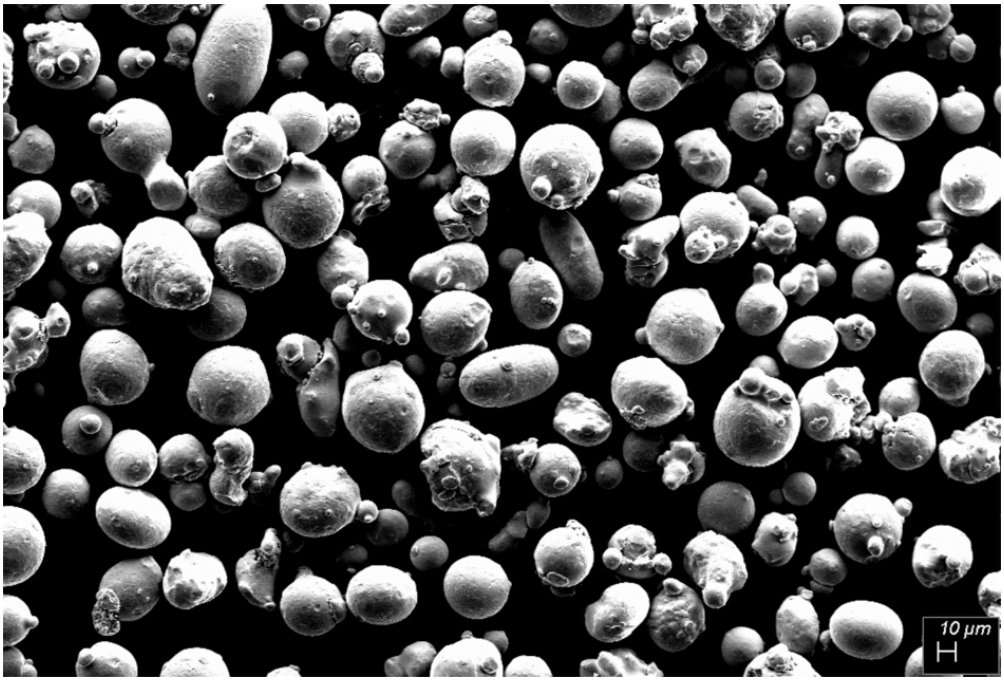


Figure 4.4: SEM image of the Fe-Si powder at 200× magnification, showing its generally spherical particle shape.

4.3.2 Green Density Optimization

Table 4.4 shows the average green densities of the samples obtained through CT analysis. The maximum green density obtained was 71.3 % ± 0.5 %, corresponding to build 7. Figure 4.5 shows a cross-section of the sample from build 7 in the xy plane, before and after image segmentation. The maximum density value obtained for Fe-Si is 43% higher than that obtained for Fe. This is in part due to the difference in particle shape, where the spherical Fe-Si packed more efficiently in the bed [61]. Other contributors included the binder adhesive strength, as well as the parameter space that was probed, as discussed below. The density profiles along the z-direction are shown in Appendix B.

Table 4.4: Green densities obtained for the different builds for Fe-Si.

Build	L^*	v (mm/s)	w (rpm)	S (%)	Green Density (%)
1	1.5	6	100	67.5	56.6 ± 0.7
2	2	10	100	67.5	56.5 ± 0.8
3	2	6	200	67.5	56.3 ± 0.5
4	1.5	10	200	67.5	55.9 ± 0.4
5	2	6	100	82.5	55.4 ± 0.3
6	1.5	10	100	82.5	65.7 ± 1.3
7	1.5	6	200	82.5	71.3 ± 0.5
8	2	10	200	82.5	52.5 ± 0.3
9	1.75	8	150	75.0	58.7 ± 0.1
10	1.75	8	150	75.0	57.1 ± 0.3

Green Density as a Function of Process Parameters

One of the goals of this chapter is to determine an optimum set of print parameters for the material and the process map. This set of parameters should in principle produce close to the maximum green density. The optimization could be performed based on an experimental model that describes green density as a function of the process parameters. An OLS regression model was run on the dataset to extract the model. The complete

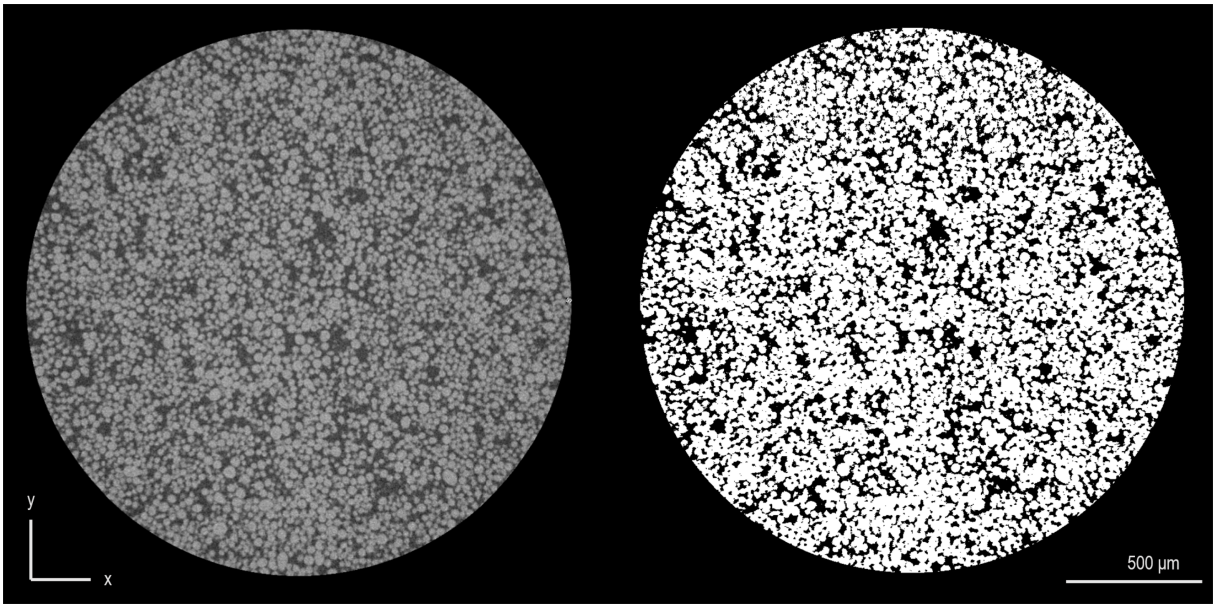


Figure 4.5: Segmentation of CT images density calculation; (left) unsegmented and (right) segmented images in the xy plane of sample 7 as a green sample.

tables, residuals plot and Q-Q plot of the regression model are shown in Table B.3, Table B.4, Figure B.5 and Figure B.6. The half-factorial experimental design allowed detection of main and second order effects only. For this reason, the regression model was run for only those effects. More discussion on this point is given later in this section.

The process maps showing the parameter effects on green density are shown in Figure 4.6. The isolated plots of green density against each parameter are contained in Figure B.3. A threshold of $p < 0.05$ was used as a probability of significance in the regression analysis. The results were generally consistent with those obtained for Fe. All of the main effects were significant, with L^* showing the strongest effect ($p = 6.6\times10^{-21}$); ω on its own exhibited the weakest effect ($p = 0.0061$), although still being significant.

The experimental design contained aliased interactions. The interaction of L^* and S was aliased with that of v and ω. This alias pairing was chosen on purpose in the experimental design based on the results obtained for Fe (see Table B.1), where layer thickness and binder saturation did not heavily interact. Moreover, it was expected that

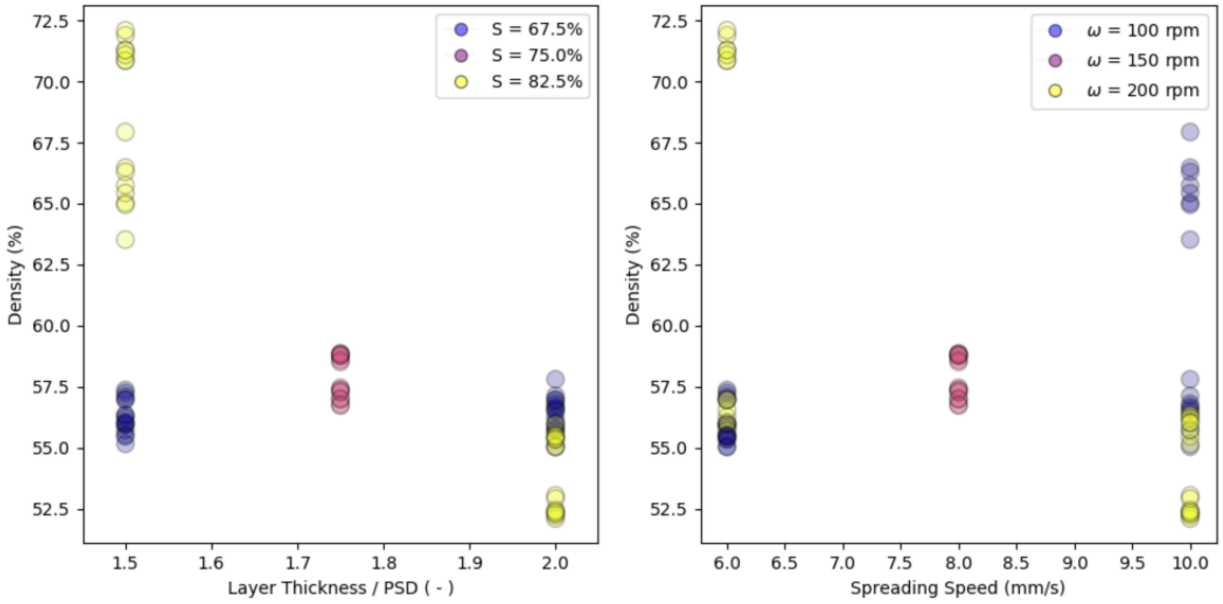


Figure 4.6: Green density behavior with respect to (left) normalized layer thickness and binder saturation, and (right) spreading and compaction speeds.

the v-ω interaction would be stronger than that of L^*-S because v and ω directly affect powder packing. This idea was observed in the results, where the strongest interaction effect was by far that of v-ω ($p = 1.7\times10^{-46}$). The aliased L^*-S interaction was not a significant interaction ($p = 0.66$). The L^*-S interaction could impact shape fidelity rather than density, which was not quantified in this study.

Another aliased interaction was that of v-S and L^*-ω. The influence of ω was mostly on powder compaction, and it follows that L^* and w had a strong interaction ($p = 2.3\times10^{-4}$) since both affect powder packing in a layer. The v-S interaction did not have a significant effect ($p = 0.095$). The v-S interaction could impact shape fidelity, as it was visually observed that linear spreading of the powder was impacted by the amount of binder deposited in the previous layer. Therefore, it is more meaningful to interpret the L^*-ω as the significant interaction on density.

Based on the regression model, a linear equation was obtained that describes green density as a function of the four printing parameters. Such an equation would hold for

the spanned parameter range, but may or may not hold outside it. From the regression analysis and the statistical significance results, green density ρ can be expressed through Equation 4.1.

$$\begin{aligned}\rho =& 8.3129 + 4.7237L^* + 8.1254v + 0.1982\omega + 3.0759S \\ & - 1.1786L^*v - 0.0631L^*\omega - 0.0367v\omega + 0.2802\omega S\end{aligned} \tag{4.1}$$

Density Optimization

The experimental plan was designed to allow optimization. The fit model obtained through regression was used as the curve for optimization. A linear least squares algorithm was used for optimization. The bounds were chosen as the parameter range spanned in this experiment (Equation 4.2), and the resulting optimized set of parameters is shown in Equation 4.3. This optimal set of parameters was not part of the fractional factorial experimental design. Future work can include a validation print at the optimum parameters and measure green density.

$$\begin{aligned}1.5 \leq L^* \leq 2 \\ 6 \leq v \leq 10 \\ 100 \leq \omega \leq 200 \\ 67.5 \leq S \leq 82.5\end{aligned} \tag{4.2}$$

The values of the optimum parameters are sensible. Based on the Fe results and literature, higher green densities are usually obtained with lower L^* and lower v. Lowering ω intuitively means compacting the powder more gently. Finally, the Fe results suggested that a medium binder level improved density as opposed to too low or too high. The optimization analysis here suggested that increasing S leads to higher densities. This outcome is expected to change if a larger range of saturation levels were chosen. A larger span of parameters would likely result in slightly different optimum parameters. The fit model captured here was successful in providing an optimum set of parameters for the

process map and boundaries described by Equation 4.2, which was the intended goal for this material.

$$\begin{aligned} L^* &= 1.5 \\ v &= 6.0 \\ \omega &= 100 \\ S &= 82.5 \end{aligned} \tag{4.3}$$

In the optimum set, only L^* and v were on the bounds (Equation 4.2), but not ω nor S. This suggested that there was curvature in the hyperplane that represented the fitted model in 5 dimensions. To capture the curvature, ω and S could be expressed in the regression function not as a line but as an exponential or a quadratic term. This notion was reinforced by the seeming trend in the data points for ω and S in Figure B.3, although there are too few points to fit a good curve with high confidence. A larger span of parameters would likely reveal clearer trends.

Packing Factor

The optimization above is directly applicable to industrial settings that use the BJ system used in this work (ExOne M-Flex), or similarly designed systems. Beyond that, it is useful to generalize functional forms as much as possible such that they apply to other BJ systems that are designed differently and have different parameters. (This can apply to manufacturers such as Desktop Metal and Markforged.) Layer thickness (or L^*), v and ω all influence powder packing. Saturation is a distinct variable that relies on powder packing as an input (see Equation 2.2) but is not directly related to layer thickness nor spreading speeds. In the most general sense, green density is influenced by powder packing factor PF and saturation. It is therefore useful to extract a function from the regression analysis that describes PF in terms of powder packing – namely, L^*, v and w.

Equation 4.1 represented the regression model with the coefficients with least errors (OLS). It follows that Equation 4.4 describes the green density, where a and b are the fit

coefficients. The PF is therefore expressed in Equation 4.5 with the coefficients as obtained from the model. The limitation of this analysis is the narrow process region and the short span of the parameter values. With enough data points, it could be possible to observe how well the expression holds outside the narrow region. Future work can validate the derived equation form and tune the coefficients by having more data points and a larger span of parameter values.

$$\rho = PF(L^*, v, \omega) + aS + b\omega S \tag{4.4}$$

$$PF = 4.7237L^* + 8.1254v + 0.1982\omega - 1.1786L^*v - 0.0631L\omega - 0.0367v\omega \tag{4.5}$$

One of the obstacles in the optimization work is expressing the most appropriate model that correctly describes packing behavior and its interaction with saturation. This is challenging because there are no computationally-inexpensive methods to describe powder behavior. Efforts to model powder flow and powder-binder interaction such as the work of Miyanaji et al. [72] will help in developing good physical models, which can guide future work on response surface modeling and optimization of the BJ process.

The PF can be treated as a non-dimensional process parameter that groups together several dimensional parameters such as L^*, v and ω. One benefit, as suggested earlier, is a unified approach to parameter optimization across various BJ systems. Another benefit is the potential to use PF as a parameter in a MSS created for the process. The MSS can represent a complex 3D process map for a material or a product application. By using the PF as the third dimension of the MSS, a large portion of the BJ process can be captured in a single parameter and plotted against SSS or LPS behavior of a particular alloy. Such a map can be beneficial to the adoption and utility of BJ in industrial applications.

Limitations of the Regression and the Optimization Method

There are limitations to the regression and optimization work in this chapter. First, a validation print should be conducted to test the optimum parameter result. This will be

part of future work beyond this thesis. Second, the fit function was a linear function. A non-linear model could result in a better fit, in particular for S and ω. However, a larger span of data points is needed to detect the trends. Since this work focused on a narrow process window, the linear model was likely accurate enough for the purpose of optimization. In addition, the green density of 71.3% obtained here is quite high in comparison to the powder tap density of 57.2%. The high density obtained here was due to the slow compaction of the powder by the counter-rotating roller. Similar green densities have been demonstrated in literature with adequate compaction [15], albeit with multi-modal powder blends.

4.3.3 Debinding Analysis and Debinding of the Final Samples

The work done in this chapter used a commercial binder from the ExOne Company. The binder is aqueous and can be driven off by thermal decomposition in an inert atmosphere. The debinding profile of the binder is illustrated in Figure 4.7. Decomposition started early at nearly 100°C, but it only became very rapid at 400°C. The binder was completely driven off at nearly 480°C.

A TG measurement of debinding performed on a printed sample is shown in Figure 4.8. An isotherm was held at 400°C for 60 min to drive off the binder, which was completed by nearly 500°C. No oxidation was detected in the curve.

The final samples were debound in a tube furnace. While debinding was under reducing atmosphere, the furnace was not fully gas-sealed. Surface oxidation was visible in all the samples, apparent as a dark red-brown shade. This is demonstrated in Figure 4.9. The presence of oxides was not ideal as they could interfere with sintering. Since the samples were porous, it was expected that some oxides could have formed on some particle surfaces inside the samples. Because of the oxidation, it was expected that sintering at the surface could retain higher porosity than the core of the samples.

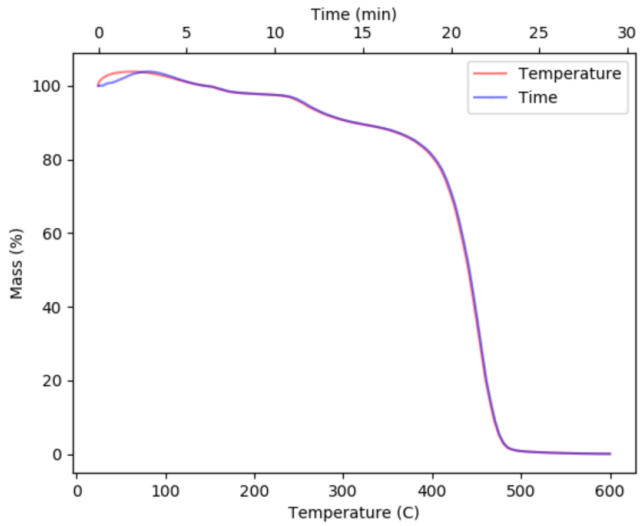


Figure 4.7: TG curve of the ExOne binder showed an acceptable debinding temperature of 400°C.

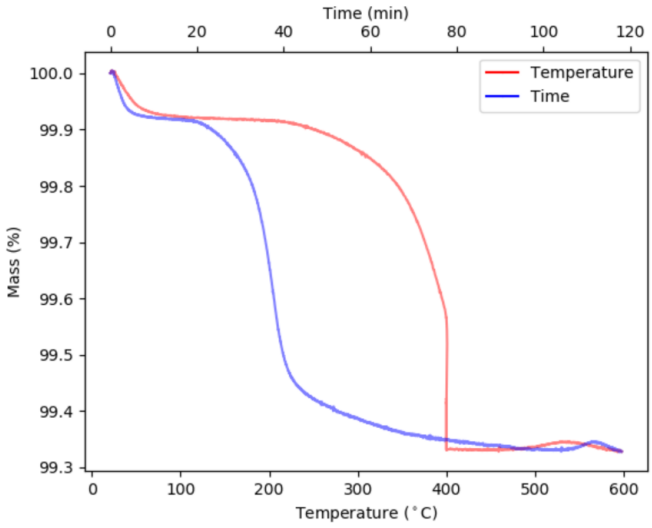


Figure 4.8: TG curve showing the debinding profile of Fe-Si (build 7) printed with the ExOne binder.

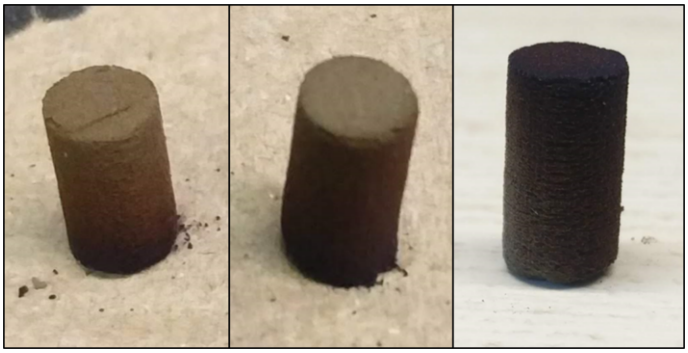


Figure 4.9: Debound samples in preparation for sintering.

4.3.4 Liquid Phase Sintering

Core Density

Sintering was performed on the samples from build 7, which resulted in the highest green density. Sintering was conducted at a temperature of 1470°C with an isotherm duration of 15 minutes and 1 hour. The density values were calculated through LCM analysis and are presented in Table 4.5. These values reflected the core density of the samples, which is representative of the sintering conditions. However, they did not capture density at the sample edges. Linear shrinkage in the 1 hour and 15 minute samples was 9.5 ± 1.2 % and 7.7 ± 1.1 % respectively. The most likely explanation is that variation in surface porosity, particularly at the edges of the samples, was not captured in the core density calculations. Surface porosity in BJ samples is not uncommon [75]. It is in part due to weakly adhered powder (where the binder only partially binds the powder) and in part due to oxidation.

Table 4.5: Density values of sintered samples from build 7 at two different isotherm durations.

Temperature (°C)	Isotherm Duration (hh:mm)	Density (%)
1470	00:15	94.2 ± 0.3
1470	01:00	94.7 ± 0.9

The density values indicated that the temperature used was adequate in producing high

core densities. Figure 4.10 shows LCM optical images of samples sintered for 15 min and 1 hour. Generally, the level of porosity is similar for both durations, but pores appeared slightly more closed with the longer duration. The optical images can be misleading in terms of the porosity level for these Fe-Si samples. Close examination of the optical images revealed that many of the dark "spots" were dark-colored regions in the larger matrix and could appear as pores. Further characterization via laser height mapping showed that the dark regions were solid features and represented liquid phase sinter necking. A more detailed discussion on these observations is presented below.

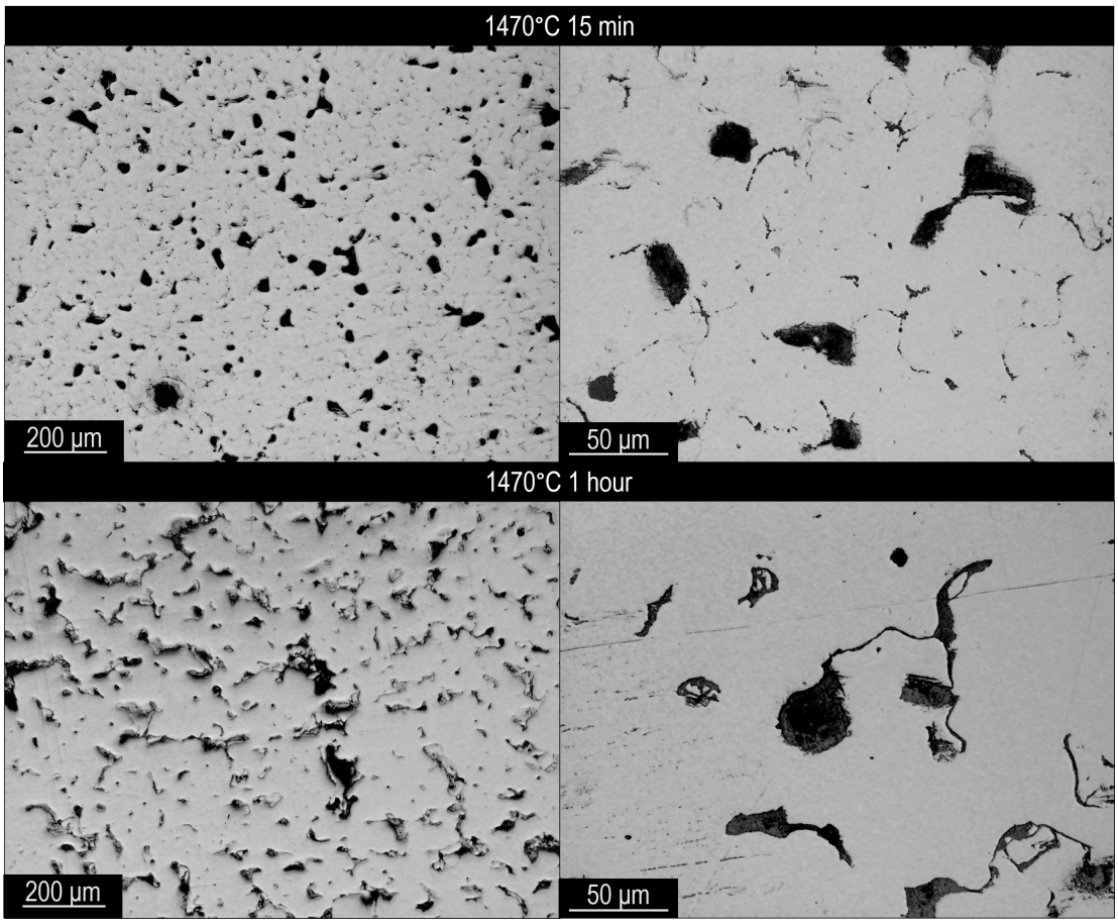


Figure 4.10: Laser confocal microscopy images of the sintered samples.

Evidence of Liquid Phase Sintering

There were several observations that indicated the presence of LPS. The first observation related to the effect of sintering duration. Sintering for 15 min achieved above 90% core density. Such a high densification rate is consistent with LPS [3, 79, 93]. Sintering in the solid state does not normally lead to such high densification rates [1]. This idea was also observed in the Fe dataset in Chapter 3. Furthermore, the results in Table 4.5 showed that increasing sintering time from 15 min to 1 hour only slightly increased densification. This is also consistent with the theoretical understanding of LPS [3, 93].

The second observation was related to sinter necks and pore closure. Examination of the height maps under high magnification in LCM showed the formation of sinter necks. The height maps and composite laser-optical images are shown in Figure 4.11. The height maps clearly differentiated between open pores and closed pores, as only the open pores appeared dark. If the dark regions were traced, they often followed a curved outline. These closely resembled fully formed sinter necks in the liquid phase [3, 4]. The shape of the necks indicated that the final stage of sintering was reached [79]. The density value being above 92% also suggested that the final stage was reached [79]. As annotated in Figure 4.11, some of the necks traced a circular outline that appeared to represent fully sintered individual powder particles.

In addition, it was observed that pores were often seen where the dark regions appeared. This evidence supported the idea that liquid formed during sintering, contributed to sinter neck growth between particles and fully or partially filled the voids in the particle arrangement. It was hypothesized that the liquid consisted at least in part of the dark-colored material, and that the material contained more Si than the larger Fe matrix. This observation was reported in literature for Fe-Si powders melting under high temperatures [110]. In order to check if the hypothesis were correct, the samples were imaged under SEM and analyzed with EDS. SEM images of the samples are shown in Figure 4.12. Since SEM shows the surface morphology in high resolution, the texture of the sinter necks was visible in the images.

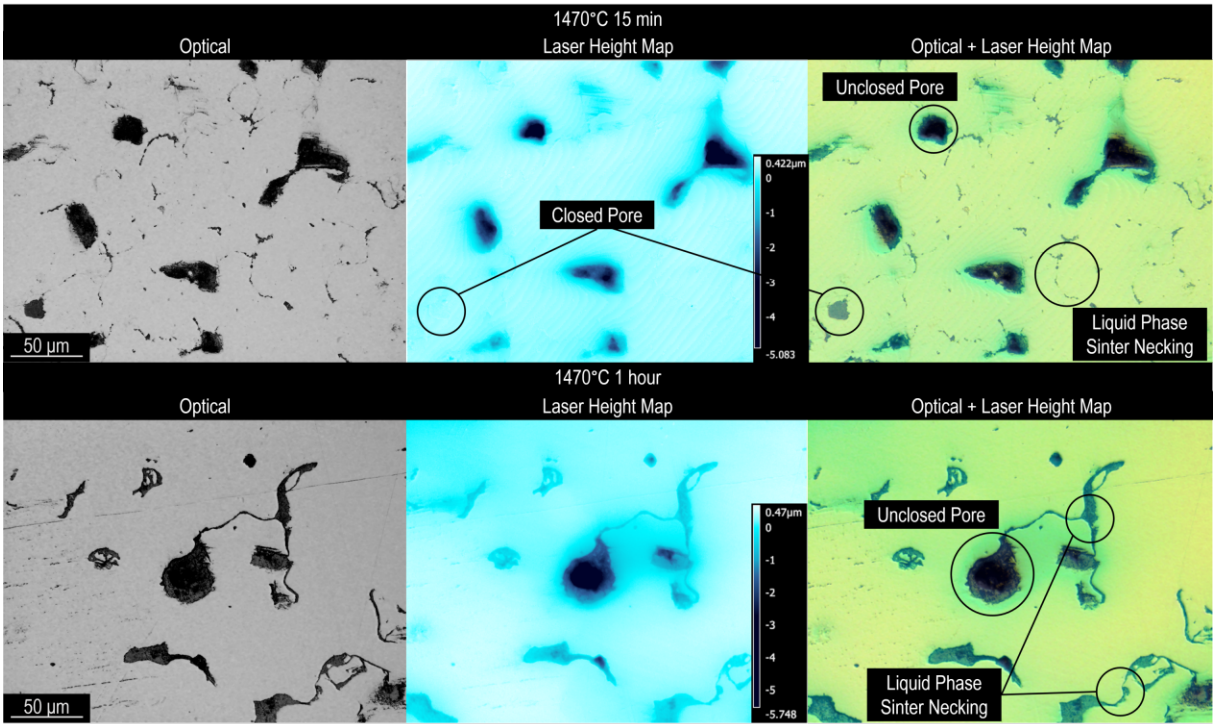


Figure 4.11: Optical and laser confocal images of sectioned samples sintered for 15 min and 1 hour; by using laser height mapping, pores could be clearly differentiated from the solid darker regions. Examples of sinter necks are annotated where it appeared liquid formation occurred and connected particles together.

Observations of Segregation

In the LCM and SEM images, darker regions were observed at sinter necks and pores, and sporadically deposited in the larger alloy matrix. The hypothesis was that the dark regions contained Si, which diffused out of the alloying particles and filled the pores, as posited in the theory of SLPS [93]. EDS analysis was performed to detect the elemental composition of the dark regions. The EDS results in Figure 4.13 showed that dark regions were Si- and O- rich compositions and had lower Fe levels than the larger alloy matrix.

The presence of O suggested that oxides formed, which was likely an artifact of oxidation from debinding. The EDS signals for Si and O peaked mostly in tandem. The Fe signal was

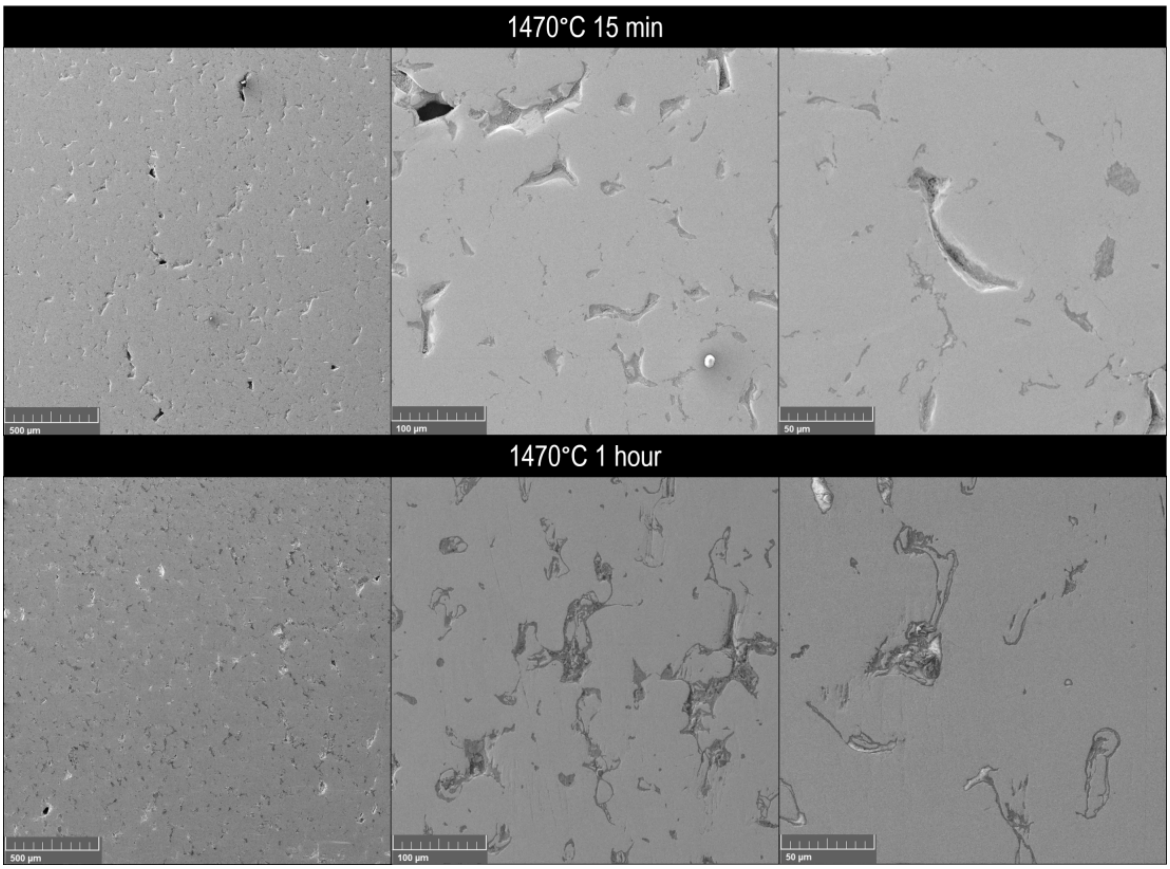


Figure 4.12: Scanning electron microscopy images of the sintered samples, showing sinter necks formed in the alloy matrix. A curvature in the regions of sinter necks is visible, which was indicative of sintered powder particles.

low when the Si-O signals peaked, which indicated a segregation of the alloying elements. This confirmed the hypothesis that the dark regions were a Si-rich constituent. This observation is consistent with the theory of SLPS [4, 93]. This result, coupled with the observation that many pores existed near the Si-rich regions, suggested that Si diffused out of the powder particles as a liquid and wetted the particle surfaces. This created a strong capillary force that resulted in rapid densification [3]. A schematic of the hypothesis is illustrated in Figure 4.14. Close future studies can be planned to further validate the hypothesis at a wider range of sintering conditions.

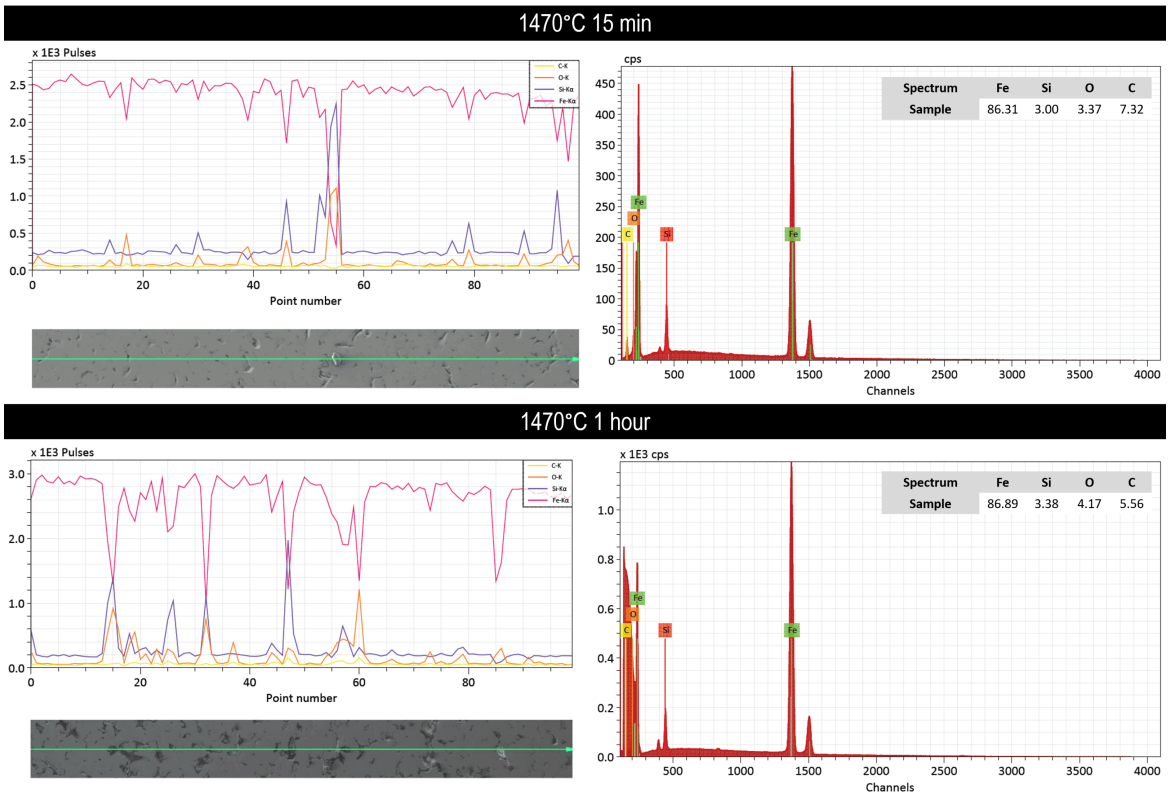


Figure 4.13: Energy dispersive spectroscopy results for the sintered samples. The analysis showed that a Si-rich constituent separated from the main Fe matrix upon liquid phase sintering.

SSS usually occurs in the ramp up to the liquid phase [4]. Sinter necks in the solid state likely occurred before Si diffused out of the particles, leading to slight densification at first. As the temperature increased, Si gained enough energy to diffuse out and initiate LPS. At the peak temperature of 1470°C, Fe atoms likely gained enough energy to diffuse via volume diffusion [1] and form sinter necks. The Fe particles began to soften, deform and sinter together at the peak temperature. This was evident in the LCM and SEM images, where the Fe matrix appeared well-connected and without many visible sintered powder particles. This observation indicated an advanced state of sintering in the final stage [1, 79, 93].

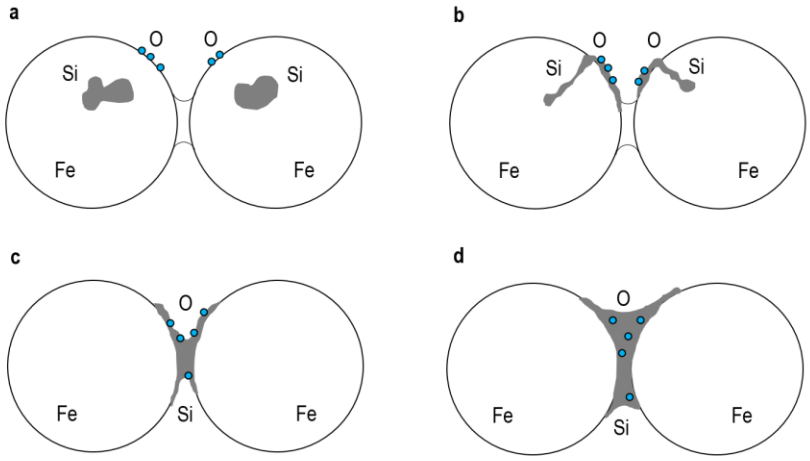


Figure 4.14: Schematic of the hypothesized diffusion of Si during sintering: (a) at high temperatures below the peak, solid state sinter necks slowly began to form; (b) at the peak temperature, Si diffused out of the particles; O was present on the surface of particles due to surface oxidation; (c) Si formed sinter necks in the liquid phase; (d) sinter necks grew wider and the larger Fe matrix softened, deformed and connected.

A larger collection of the LCM images, SEM images and EDS results are contained in Appendix C for reference.

Discussion on the Solidus Temperature

The pre-alloyed nature of the Fe-Si powder meant that it underwent SLPS. SLPS is advantageous because it reduces the need for fine particle sizes to initiate LPS [93]. Normally in LPS, the liquid starts to nucleate on surfaces or boundaries because of the lower nucleation energy barrier [79], and therefore a finer particle size increases the surfaces available for liquid formation. In SLPS, liquid formation starts inside the powder particles. The disadvantage of SLPS is the requirement to cross the solidus point of the alloy. This is in contrast to typical LPS, in which liquid formation can start at lower temperatures if the particle sizes were sufficiently fine. Furthermore, the range of stable liquid formation is narrow in SLPS [4], as typically microstructural softening and shape distortion occurs

beyond nearly 30% of the metling range [93]. This makes control of SLPS more difficult. In this work, the bulk of the evidence suggested that LPS was the mode of sintering for the Fe-Si alloy. DSC measurements showed a solidus point of 1489.9°C, yet initial trials at this temperature resulted in complete melting of the samples. For this reason, it was suspected that the effective onset temperature was lower than 1489.9°C. One limitation of the DSC measurement in this case was the fast heating rate of 20°C/min, which could have caused a peak shift. Moreover, the presence of oxides due to debinding could induce melting earlier than predicted [19, 82].

It is useful to ascertain if the temperature of 1470°C used for sintering were beyond the solidus point or not. This would help in evaluating whether SLPS was the mode of sintering. To establish this, sintering of one sample was conducted at 1482°C. This temperature was deliberately chosen to narrow down the range of possible values of the solidus temperature. The sample sintered at 1482°C was sinetered without shape distortion and resulted in a core density of 95.8%. LCM and SEM images of this sample are shown in Figure 4.15.

The observations made thus far are that sintering at 1490°C resulted in complete melting, and that sintering at 1482°C did not result in complete melting. Taking the threshold of melting as the estimated 30% of the melting range [93], it follows that (1) 1490°C must be at least 30% of the melting range and (2) 1482°C must be at most 30% of the melting range. The DSC measurement showed a melting range of 35°C. From (1), it can be said that the solidus point is approximately 1479.5°C. Therefore, 1482°C is 2.5°C above the solidus point, or at nearly 7% liquid volume fraction. Such a volume fraction is acceptable for SLPS [3]. This suggests that sintering at 1482°C was in the SLPS mode. However, observations of sinter necking, rapid densificaton and the slight influence of sintering duration strongly indicated LPS in the samples sintered at 1470°C. All of these observations culminate in the conclusion that liquid formation likely started in the alloy before the solidus point. Although pre-alloyed, the distribution of Si in the Fe particles could be non-uniform (depending on the powder manufacturing process), which could cause early melting of Si and its subsequent segregation from the Fe matrix.

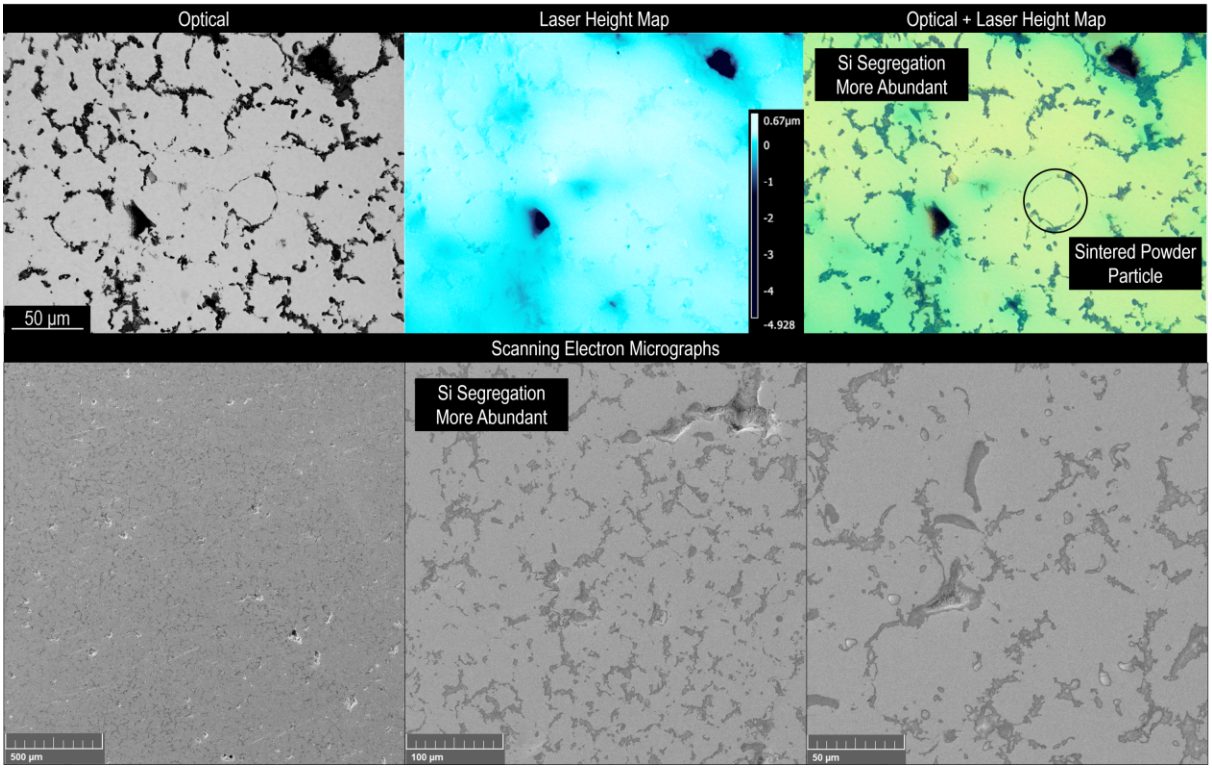


Figure 4.15: Laser confocal microscopy and scanning electron microscopy of the sample sintered at 1482°C. The sample did not experience shape distortion and the micrographs show progression of liquid phase sintering. A higher abundance of the darker Si region was observed, which could indicate that Si segregation could be amplified by temperature.

Discussion on Si Segregation

Observations of all the sintered samples (see Appendix C) generally suggested a segregation of the Si from the Fe matrix. Since more segregation was observed in the sample sintered at 1482°C, it is possible that Si segregation could be promoted by increasing temperature. On the other hand, one of the early samples sintered at 1470°C for 1 hour resulted in severely pronounced segregation. The sample core density was calculated to be 94.8% and EDS analysis showed that the segregated material was Si-rich. LCM images and EDS analysis of the sample are shown in Figure 4.16 to illustrate the severe segregation.

The severe segregation phenomenon was considered an anomaly due to the lack of replicates. It is certainly of interest to understand the cause of the phenomenon. The LCM images showed that the Si "flowed" very well around the Fe matrix, dispersing itself more uniformly than in other samples. This enhanced "flow" phenomenon is consistent with improved surface wetting [79].

One likely explanation is excessive oxidation. EDS analysis showed excessive O content at 15.11%. The region rich in Si and O also showed low levels of Fe, consistent with other samples. The sample could have oxidized to a tremendous extent during debinding; during LPS, the diffused Si (which was likely in the liquid phase) wetted both Fe and oxide surfaces. It is possible that the Si reacted with O to form SiO_2, where the presence of Fe lowered its melting point. The regions rich in Si and O were consistently low in Fe, making it unlikely that Fe-O oxides were dominant. If the wetting behavior of Si is better (by producing a smaller wetting angle) on oxides than on Fe, then the oxidation would justify the phenomenon. It is difficult to quantify and validate this idea without further research and analysis.

The element segregation can have potential benefits if it were exploited properly. One idea is to segregate a non-conductive element or phase from the alloy itself in a controlled manner such that predictable layers of conducting and non-conducting material are created, similar to a laminar composite. This could be useful for instance for magnetic applications, where the layered structure could mimic the laminated core material of stators in electric generators. If the segregation were related to oxidation, then it could be possible to vary powder particle arrangement to induce segregation in controlled locations. The O content could be purposely varied to exploit the segregation effect. Multi-modal or multi-compositional powder blends could be used to promote LPS and segregation. Variable binder content across layers in the print could promote segregation in select locations. Coating of particle surfaces could also be explored to promote sinter neck formation in preferential locations. These ideas are starting points for future research in BJ and sintering. The potential rests in the high degree of process customization native to BJ, and the vast depth of knowledge in LPS.

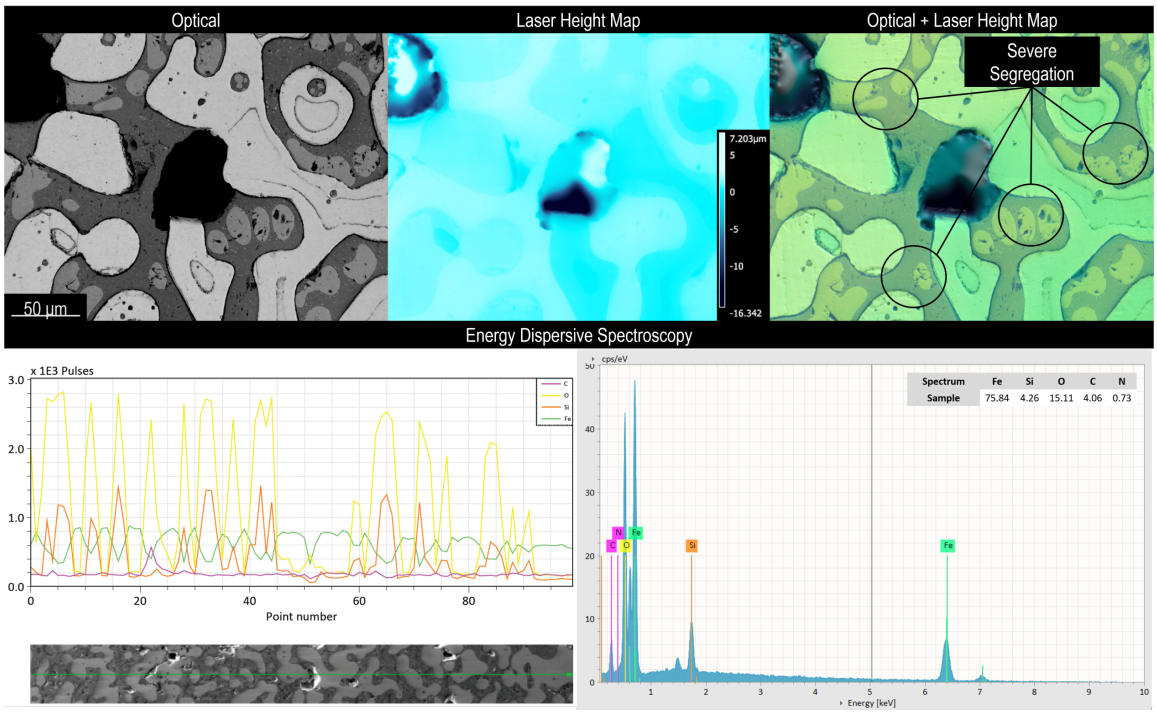


Figure 4.16: Laser confocal microscopy and energy dispersive spectroscopy images of an outlier sample sintered at 1470°C. The sample showed severe Si segregation, which was most likely caused by excessive oxidation before sintering.

4.4 Summary and Outcomes

In this chapter, the BJ process was optimized for green density through a factorial experimental design for spherical Fe-Si powder. Green parts were produced in a commercial BJ system and analyzed for density estimates through CT analysis. The optimization study produced a process map for the powder and an optimal set of parameters to achieve a high green density. More importantly, empirical expressions were derived that describe green density as a function of layer thickness, powder size, binder saturation, linear spreading speed and rotational spreading speed. An expression for the powder packing factor was derived in terms of the layer thickness, powder size and spreading parameters. The trends showed that layer thickness and spreading speed should be as low as possible, as their

effects were observed to be mostly linear. By contrast, binder saturation and rotational spreading speed exhibited a curvature in the regression analysis, and should be set to optimal values for maximum green density. Rotational speed should generally be a low value so as to compact the powder without causing layer shifting. Binder saturation should be high enough to fill most of the voids between particles. The empirical relationships can be useful for modeling of powder behavior and powder-binder interaction in BJ. The optimal parameter set needs to be validated with a test print, which is of interest in future work.

Generally, higher green densities were obtained with the spherical Fe-Si powder than the irregular Fe powder. A maximum green density of 71.3% was achieved. This was primarily due to the tight packing of the powder particles. The careful selection of parameters, narrow process region and spherical particle shape all contributed to this achievement. A full central composite experimental design with a response surface model is of interest in future work. It can accurately capture the response of green density to binder saturation and rotational spreading speed.

Samples from the highest green density parameter set were selected for sintering in the liquid phase. Core density values of 94.2-94.7% were achieved. Imaging of sectioned samples under LCM and SEM revealed that sinter necks were well developed and that sintering reached the final stage. There was little improvement to densification at longer durations, where sintering at peak temperature for 15 minutes was sufficient in causing high densification. This observation agreed with the theory of LPS. High densification rates are an important advantage of LPS over SSS, as demonstrated with the Fe dataset in Chapter 3. However, careful control of the sintering conditions is needed and can involve iterations of trial and error [79].

EDS analysis showed that sporadic, dark regions in the main alloy matrix were rich in Si and O. The observations suggested that Si segregated from the Fe matrix by diffusing out of the particles as a liquid and filling the pores. More pronounced Si segregation was noted at increased temperatures, and in particular under excessive oxidation. Overall, this work demonstrated the work flow for sintering Fe-Si powder in the liquid phase. This work also set the framework for dilatometry measurements and development of the MSC model. The MSC (or MSS) will represent the process map for sintering of this alloy, and will be of great utility to control final product densities. Dilatometry measurements are currently

planned as future work beyond this thesis. In the context of industrial applications, the work flow can be applied to manufacture complex geometries in BJ and achieve high densities through LPS. Examples of such applications include stators and rotors in electric motors or generators. Future work will print and sinter complete products and quantify their functional properties. For stator or rotor applications, these can include mechanical strength, electrical conductivity and response to magnetic fields.

Chapter 5

Conclusions & Future Directions

The work in this thesis focused on process development of BJ and subsequent heat treatment for Fe and Fe-Si powders. BJ process maps for the two materials were developed in terms of key process parameters. The study on Fe-Si focused on process optimization through regression analysis. Debinding of printed samples was studied through TG analysis, and was examined against binder content for the Fe dataset. Sintering of printed samples was studied in the solid state (Fe) and liquid phase (Fe-Si). Samples with high final densities were produced, with values exceeding 90%. Fe and Fe-Si are industrially relevant powders, with applications in soft magnetic components and electric machinery. The following sections summarize the important conclusions drawn and future directions in this research.

5.1 Green Density Optimization

The irregular Fe powder resulted in lower green density values than did the spherical Fe-Si powder. This was primarily due to its different morphology, as well as a narrower selection of process parameters for Fe-Si intended to maximize green density. Maximum green densities of 49.7% were obtained for Fe, compared to 71.3% for Fe-Si.

The green density optimization study revealed interesting trends in the response of

green density to process parameters. Generally, the data showed that all of normalized layer thickness, binder saturation, and powder spreading linear and rotational speeds influenced green density. For the parameter range studied, normalized layer thickness had the strongest effect. Strong interactions were detected of normalized layer thickness and rotational speed, as well as linear speed and rotational speed. These are expected to strongly relate to powder compaction. The regression analysis and optimization revealed that to maximize green density, normalized layer thickness and linear speed should be minimized, while rotational speed and binder saturation should be carefully set to an optimal value. Mathematical expressions were derived for green density and powder packing factor as functions of process parameters. The work could be applicable to research in powder behavior modeling and powder-binder interactions.

Future research in this area will focus first on validating the optimization results through a test print. A larger span of parameter values will benefit the regression analysis, where non-linear models and response surfaces can be fit in order to extract broader trends.

5.2 Debinding and Sintering

Debinding is a critical step in the BJ work flow. Setting of the debinding temperature depends on the binder chemistry, while the hold duration depends at least in part on the amount of binder present.

Solid state sintering was explored in the Fe samples. A final density of 91.3% was achieved after 6 hours of sintering at 97% of the melting point. Observations of sinter necks and porosity distribution suggested that sintering progressed in the intermediate-final stages. Spatial variability in local density of the samples was greatly dampened after solid state sintering at the high temperature. Control over the sintering conditions could overcome some of the limitations of irregular powder packing. Liquid phase sintering was studied for Fe-Si samples, where densification occurred at much fast rates than in solid state. A sintered density of 94.2% was achieved after 15 minutes of sintering at peak temperature. The bulk of the evidence suggested that sintering occurred in the supersolidus liquid phase mode, and liquid formation likely started before the solidus point of the alloy

was reached. Segregation of Si was consistently observed, which appeared to be accelerated at higher temperatures and by the presence of oxidation.

In future research, the characteristics of debinding with respect to process parameters in more depth can be explored. Analysis of oxidation products or binder residuals can be useful in predicting potential sintering failures; this can be done through chemical analysis techniques.

This thesis set up the groundwork for development of master sinter curves (or surfaces). Dilatometry measurements are planned in future work to compliment the efforts of this thesis. Estimation of the apparent activation energies in sintering will help in predicting densification behavior. Studies on consistency and predictability of shrinkage is of interest, as well as shape distortion. With both solid state and liquid phase sintering, exploration of sintering aids is of interest. Multi-modal powder blends and particle surface additives are possible avenues of research. This can be useful for product development for specific applications. Finally, printing and sintering of large, complex products are of interest. The Fe and Fe-Si materials are directly applicable to soft magnetic components, and quantification of densification behavior and final product functionality can be an extension to the work done in this thesis.

References

[1] R.M. German. Fundamentals of sintering. *ASM International, Engineered Materials Handbook*, 4:260–269, 1991.

[2] R.M. German. Coarsening in sintering: Grain shape distribution, grain size distribution, and grain growth kinetics in solid-pore systems. *Critical Reviews in Solid State and Materials Sciences*, 35(4):263–305, 2010.

[3] R.M. German, P. Suri, and S.J. Park. Review: Liquid phase sintering. *Journal of Materials Science*, 44(1):1–39, 2009.

[4] R.M. German. Supersolidus liquid-phase sintering of prealloyed powders. *Metallurgical and Materials Transactions A: Physical Metallurgy and Materials Science*, 28(7):1553–1567, 1997.

[5] H. Su and D.L. Johnson. Master sintering curve: a practical approach to sintering. *Journal of the American Ceramic Society*, 79(12):3211–3217, 1996.

[6] D.C. Blaine, S.J. Park, and R.M. German. Linearization of master sintering curve. *Journal of the American Ceramic Society*, 92(7):1403–1409, 2009.

[7] R. Bollina, S.J. Park, and R.M. German. Master sintering curve concepts applied to full-density supersolidus liquid phase sintering of 316L stainless steel powder. *Powder Metallurgy*, 53(1):20–26, 2010.

[8] T. Brandt, B.and Rabe. Compilation and Evaluation of the Pressure-Assisted Master Sintering Surface for Lowerature Cofired Ceramics. *Journal of the American Ceramic Society*, 98(11):3503–3508, 2015.

[9] O. Kubaschewski. *Phase diagrams of binary iron alloy*. ASM International, 1993.

[10] I. Rishmawi, M. Salarian, and M. Vlasea. Tailoring green and sintered density of pure iron parts using binder jetting additive manufacturing. *Additive Manufacturing*, 24:508–520, 2018.

[11] E.M. Sachs, J.S. Haggerty, M.J. Cima, and P.A. Williams. Three-dimensional printing techniques, April 20 1993. US Patent 5,204,055.

[12] ExOne History. https://www.exone.com/About-ExOne/History.

[13] M. Vlasea, E. Toyserkani, and R. Pilliar. Effect of gray scale binder levels on additive manufacturing of porous scaffolds with heterogeneous properties. *International Journal of Applied Ceramic Technology*, 12(1):62–70, 2015.

[14] Y. Bai and C.B. Williams. Binder jetting additive manufacturing with a particle-free metal ink as a binder precursor. *Materials and Design*, 147:146–156, 2018.

[15] S.J. Gregorski. High green density metal parts by vibrational compaction of dry powder in the three-dimensional printing process, 1996.

[16] Emanuel Sachs, Michael Cima, James Cornie, David Brancazio, Jim Bredt, Alain Curodeau, Tailin Fan, Satbir Khanuja, Alan Lauder, John Lee, et al. Three-dimensional printing: the physics and implications of additive manufacturing. *CIRP annals*, 42(1):257–260, 1993.

[17] A. Mostafaei, E.L. Stevens, J.J. Ference, D.E. Schmidt, and M. Chmielus. Binder jetting of a complex-shaped metal partial denture framework. *Additive Manufacturing*, 21:63–68, 2018.

[18] M. Vlasea. Additive Manufacturing Methodology and System for Fabrication of Porous Structures with Functionally Graded Properties, 2014.

[19] A. Mostafaei, Y. Behnamian, Y.L. Krimer, E.L. Stevens, J.L. Luo, and M. Chmielus. Effect of solutionizing and aging on the microstructure and mechanical properties of powder bed binder jet printed nickel-based superalloy 625. *Materials & Design*, 111:482–491, 2016.

[20] A. Mostafaei, J. Toman, E.L. Stevens, E.T. Hughes, Y.L. Krimer, and M. Chmielus. Microstructural evolution and mechanical properties of differently heat-treated binder jet printed samples from gas- and water-atomized alloy 625 powders. *Acta Materialia*, 124:280–289, 2017.

[21] J.A. Gonzalez, J. Mireles, Y. Lin, and R.B. Wicker. Characterization of ceramic components fabricated using binder jetting additive manufacturing technology. *Ceramics International*, 42(9):10559–10564, 2016.

[22] A. Lauder, M.J. Cima, E. Sachs, and T. Fan. Three dimensional printing; surface finish and microstructure of rapid prototyped components. In *Proceedings, Synthesis and Processing of Ceramics: Scientific Issues.* Boston, MA, 1991.

[23] T. Fan, A. Lauder, E. Sachs, and M.J. Cima. The surface finish in three dimensional printing. In *The Third International Conference on Rapid Prototyping.* Dayton, OH, 1992.

[24] ExOne Case Study: German Automaker. https://www.exone.com/ExOne/media/Case-Studies/X1_Case-Study-German-Automaker.pdf.

[25] K. Agarwal, D. Mathur, R. Shivpuri, and J. Lembo. Evaluation of prometal technique for application to dies for short run forgings. *Solid Freeform Fab. Proceedings, Austin, TX*, pages 376–83, 2002.

[26] E. Sachs, S. Allen, M. Cima, E. Wylonis, and H. Gu. Production of Injection Molding Tooling With Conformal Cooling Channels Using the Three Dimensional Printing Process. *Polymer Engineering and Science*, 40, 2000.

[27] S.M. Allen and E.M. Sachs. Three-dimensional printing of metal parts for tooling and other applications. *Metals and Materials International*, 6(6):589–594, 2000.

[28] E.A. Rojas-Nastrucci, J. Nussbaum, T.M. Weller, and N.B. Crane. Meshed rectangular waveguide for high power, low loss and reduced weight applications. *IEEE MTT-S International Microwave Symposium Digest*, 2016-August:5–8, 2016.

[29] K. Lu and W.T. Reynolds. 3DP process for fine mesh structure printing. *Powder Technology*, 187(1):11–18, 2008.

[30] A. Mostafaei, P. R. De Vecchis, E.L. Stevens, and M. Chmielus. Sintering regimes and resulting microstructure and properties of binder jet 3D printed Ni-Mn-Ga magnetic shape memory alloys. *Acta Materialia*, 154:355–364, 2018.

[31] P. Nandwana, A.M. Elliott, D. Siddel, A. Merriman, W.H. Peter, and S.S. Babu. Powder bed binder jet 3D printing of Inconel 718: Densification, microstructural evolution and challenges. *Current Opinion in Solid State and Materials Science*, 21(4):207–218, 2017.

[32] D. Snelling, Q. Li, N. Meisel, C.B. Williams, Romesh C. Batra, and A.P. Druschitz. Lightweight Metal Cellular Structures Fabricated via 3D Printing of Sand Cast Molds. *Advanced Engineering Materials*, 17(7):923–932, 2015.

[33] A. Azhari, E. Marzbanrad, D. Yilman, E. Toyserkani, and M. A. Pope. Binder-jet powder-bed additive manufacturing (3D printing) of thick graphene-based electrodes. *Carbon*, 119:257–266, 2017.

[34] C. Szpalski, M. Wetterau, J. Barr, and S.M. Warren. Bone tissue engineering: current strategies and techniquespart i: scaffolds. *Tissue Engineering Part B: Reviews*, 18(4):246–257, 2012.

[35] A. Butscher, M. Bohner, S. Hofmann, L. Gauckler, and R. Müller. Structural and material approaches to bone tissue engineering in powder-based three-dimensional printing. *Acta biomaterialia*, 7(3):907–920, 2011.

[36] C. Lam, X. Mo, S.H. Teoh, and D. Hutmacher. Scaffold development using 3d printing with a starch-based polymer. *Materials Science and Engineering: C*, 20(1-2):49–56, 2002.

[37] D. Hong, D.T. Chou, O.I. Velikokhatnyi, A. Roy, B. Lee, I. Swink, I. Issaev, H.A. Kuhn, and P.N. Kumta. Binder-jetting 3D printing and alloy development of new biodegradable Fe-Mn-Ca/Mg alloys. *Acta biomaterialia*, 45:375–386, 2016.

[38] F. Liravi and M. Vlasea. Powder bed binder jetting additive manufacturing of silicone structures. *Additive Manufacturing*, 21(February):112–124, 2018.

[39] J. Norman, R.D. Madurawe, C.M.V. Moore, M.A. Khan, and A. Khairuzzaman. A new chapter in pharmaceutical manufacturing: 3D-printed drug products. *Advanced Drug Delivery Reviews*, 108:39–50, 2017.

[40] D.T. Chou, D. Wells, D. Hong, B. Lee, H. Kuhn, and P.N. Kumta. Novel processing of iron-manganese alloy-based biomaterials by inkjet 3-D printing. *Acta Biomaterialia*, 9(10):8593–8603, 2013.

[41] U. Scheithauer, T. Slawik, E. Schwarzer, H.J. Richter, T. Moritz, and A. Michaelis. Additive manufacturing of metal-ceramic-composites by thermoplastic 3D-printing (3DTP). *Journal of Ceramic Science and Technology*, 6(2):125–132, 2015.

[42] M. Dourandish, D. Godlinski, and A. Simchi. 3D printing of biocompatible PM-materials. In *Materials science forum*, volume 534, pages 453–456. Trans Tech Publ, 2007.

[43] A. Basalah, Y. Shanjani, S. Esmaeili, and E. Toyserkani. Characterizations of additive manufactured porous titanium implants. *Journal of biomedical materials research. Part B, Applied biomaterials*, 100(7):1970–9, 2012.

[44] E. Wheat. Process Mapping and Optimization of Titanium Parts Made by Binder Jetting Additive Manufacturing, 2018.

[45] A. Basalah, S. Esmaeili, and E. Toyserkani. On the influence of sintering protocols and layer thickness on the physical and mechanical properties of additive manufactured titanium porous bio-structures. *Journal of Materials Processing Technology*, 238:341–351, 2016.

[46] F.E. Wiria, J.Y.M. Shyan, P.N. Lim, F.G.C. Wen, J.F. Yeo, and T. Cao. Printing of Titanium implant prototype. *Materials and Design*, 31(SUPPL. 1):S101–S105, 2010.

[47] S.M. Gaytan, M.A. Cadena, H. Karim, D. Delfin, Y. Lin, D. Espalin, E. MacDonald, and R.B. Wicker. Fabrication of barium titanate by binder jetting additive manufacturing technology. *Ceramics International*, 41(5):6610–6619, 2015.

[48] F.E. Wiria, S. Maleksaeedi, and Z. He. Manufacturing and characterization of porous titanium components. *Progress in Crystal Growth and Characterization of Materials*, 60(3-4):94–98, 2014.

[49] A. Mostafaei, E.L. Stevens, E.T. Hughes, S.D. Biery, C. Hilla, and M. Chmielus. Powder bed binder jet printed alloy 625: Densification, microstructure and mechanical properties. *Materials and Design*, 108:126–135, 2016.

[50] Y. Bai and C.B. Williams. An exploration of binder jetting of copper. *Rapid Prototyping Journal*, 21(2):177–185, 2015.

[51] A. Bailey, A. Merriman, A. Elliott, and M. Basti. Preliminary Testing of Nanoparticle Effectiveness in Binder Jetting Applications. *27th Annual International Solid Freeform Fabrication Symposium*, pages 1069–1077, 2016.

[52] J.P. Singh and R. Singh. Investigations for a statistically controlled rapid casting solution of lead alloys using three-dimensional printing. *Proceedings of the Institution of Mechanical Engineers, Part C: Journal of Mechanical Engineering Science*, 223(9):2125–2134, 2009.

[53] R. Singh and J.P. Singh. Comparison of rapid casting solutions for lead and brass alloys using three-dimensional printing. *Proceedings of the Institution of Mechanical Engineers, Part C: Journal of Mechanical Engineering Science*, 223(9):2117–2123, 2009.

[54] D.W. Lipke, Y. Zhang, Y. Liu, B.C. Church, and K.H. Sandhage. Near net-shape/net-dimension ZrC/W-based composites with complex geometries via rapid prototyping and displacive compensation of porosity. *Journal of the European Ceramic Society*, 30(11):2265–2277, 2010.

[55] M. Kaplas and R. Singh. Experimental investigations for reducing wall thickness in zinc shell casting using three-dimensional printing. *Proceedings of the Institution of Mechanical Engineers, Part C: Journal of Mechanical Engineering Science*, 222(12):2427–2431, 2008.

[56] M. Lanzetta and M. Santochi. Liquid-phase infiltration of thermal sintered skeletons by low-temperature gold eutectic alloys. *CIRP annals*, 55(1):213–216, 2006.

[57] M.P. Paranthaman, C.S. Shafer, A.M. Elliott, D.H. Siddel, M.A. McGuire, R.M. Springfield, J. Martin, R. Fredette, and J. Ormerod. Binder jetting: A novel NdFeB bonded magnet fabrication process. *Jom*, 68(7):1978–1982, 2016.

[58] J. Moon, J.E. Grau, V. Knezevic, M.J. Cima, and E.M. Sachs. Ink-Jet Printing of Binders for Ceramic Components. *Journal of the American Ceramic Society*, 85(4):755–762, 2002.

[59] U. Scheithauer, A. Bergner, E. Schwarzer, H.J. Richter, and T. Moritz. Studies on thermoplastic 3d printing of steel–zirconia composites. *Journal of materials research*, 29(17):1931–1940, 2014.

[60] R. Soundararajan, G. Kuhn, R. Atisivan, S. Bose, and A. Bandyopadhyay. Processing of mullite–aluminum composites. *Journal of the American Ceramic Society*, 84(3):509–513, 2001.

[61] C.T. Schade and T.F. Murphy. Development of Atomized Powders for Additive Manufacturing. 2008.

[62] A. Elliott, S. AlSalihi, A.L. Merriman, and M.M. Basti. Infiltration of Nanoparticles into Porous Binder Jet Printed Parts. *American Journal of Engineering and Applied Sciences*, 9(1):128–133, 2016.

[63] Y. Bai, G. Wagner, and C.B. Williams. Effect of Particle Size Distribution on Powder Packing and Sintering in Binder Jetting Additive Manufacturing of Metals. *Journal of Manufacturing Science and Engineering*, 139(8):081019, 2017.

[64] H.J. Yoo. Reactive binders for metal parts produced by three dimensional printing, 1995.

[65] W. Du, X. Ren, C. Ma, and Z. Pei. Ceramic binder jetting additive manufacturing: Particle coating for increasing powder sinterability and part strength. *Materials Letters*, 234:327–330, 2019.

[66] M. Asadi-Eydivand, M. Solati-Hashjin, A. Farzad, and N. A. A. Osman. Effect of technical parameters on porous structure and strength of 3d printed calcium sulfate prototypes. *Robotics and Computer-Integrated Manufacturing*, 37:57–67, 2017.

[67] M. Doyle, K. Agarwal, W. Sealy, and K. Schull. Effect of Layer Thickness and Orientation on Mechanical Behavior of Binder Jet Stainless Steel 420 + Bronze Parts. *Procedia Manufacturing*, 1:251–262, 2015.

[68] T.J. Hsu and W.H. Lai. Manufacturing parts optimization in the three-dimensional printing process by the taguchi method. *Journal of the Chinese Institute of Engineers*, 33(1):121–130, 2010.

[69] S. Atre, J. Porter, T. Batchelor, M. Bulger, K. Kunal, and P. Gangopadhya. Process Parameter Optimization for Binder Jetting using 420 Stainless Steel. *European Congress and Exhibition on Powder Metallurgy. European PM Conference Proceedings*, pages 1–6, 2016.

[70] H. Chen and Y.F. Zhao. Process parameters optimization for improving surface quality and manufacturing accuracy of binder jetting additive manufacturing process. *Rapid Prototyping Journal*, 22(3):527–538, 2016.

[71] S. Shrestha and G. Manogharan. Optimization of Binder Jetting Using Taguchi Method. *The Journal of The Minerals, Metals and Materials Society (TMS)*, 69(3):491–497, 2017.

[72] H. Miyanaji, S. Zhang, and L. Yang. A new physics-based model for equilibrium saturation determination in binder jetting additive manufacturing process. *International Journal of Machine Tools and Manufacture*, 124(September 2017):1–11, 2018.

[73] H. Miyanaji, S. Zhang, A. Lassell, A. Zandinejad, and L. Yang. Process Development of Porcelain Ceramic Material with Binder Jetting Process for Dental Applications. *The Journal of The Minerals, Metals and Materials Society (TMS)*, 68(3):831–841, 2016.

[74] H. Miyanaji, N Momenzadeh, and L. Yang. Effect of printing speed on quality of printed parts in Binder Jetting Process. *Additive Manufacturing*, 20:1–10, 2018.

[75] E. Stevens, S. Schloder, E. Bono, D. Schmidt, and M. Chmielus. Density variation in binder jetting 3D-printed and sintered Ti-6Al-4V. *Additive Manufacturing*, 22(June):746–752, 2018.

[76] S. Haeri, Y. Wang, O. Ghita, and J. Sun. Discrete element simulation and experimental study of powder spreading process in additive manufacturing. *Powder Technology*, 306:45–54, 2016.

[77] M. Vlasea, R. Pilliar, and E. Toyserkani. Control of Structural and Mechanical Properties in Bioceramic Bone Substitutes via Additive Manufacturing Layer Stacking Orientation. *Journal of Additive Manufacturing*, 6:30–38, 2015.

[78] M.J. Cima, J. Yoo, S. Khanuja, M. Rynerson, D. Nammour, B. Giritlioglu, J. Grau, and E.M. Sachs. Structural ceramic components by 3d printing. In *1995 International Solid Freeform Fabrication Symposium*, 1995.

[79] R.M. German. *Liquid Phase Sintering*. Springer Science and Business Media, New York, 1985.

[80] J.L. Johnson and R.M. German. Theoretical modeling of densification during activated solid-state sintering. *Metallurgical and Materials Transactions A: Physical Metallurgy and Materials Science*, 27(2):441–450, 1996.

[81] M. Dourandish, D. Godlinski, A. Simchi, and V. Firouzdor. Sintering of biocompatible P/M Co-Cr-Mo alloy (F-75) for fabrication of porosity-graded composite structures. *Materials Science and Engineering A*, 472(1-2):338–346, 2008.

[82] Ö. Özgün, H.Ö. Gülsoy, F. Findik, and R. Yilmaz. Microstructure and mechanical properties of injection moulded Nimonic-90 superalloy parts. *Powder Metallurgy*, 55(5):405–414, 2013.

[83] Ö. Özgün, R. Yilmaz, H.Ö. Gülsoy, and F. Findik. The effect of aging treatment on the fracture toughness and impact strength of injection molded Ni-625 superalloy parts. *Materials Characterization*, 108:8–15, 2015.

[84] Z.C. Cordero, D.H. Siddel, W.H. Peter, and A.M. Elliott. Strengthening of ferrous binder jet 3D printed components through bronze infiltration. *Additive Manufacturing*, 15:87–92, 2017.

[85] A. Kumar, Y. Bai, A. Eklund, and C.B. Williams. Effects of hot isostatic pressing on copper parts fabricated via binder jetting. *Procedia Manufacturing*, 10:935–944, 2017.

[86] R. Frykholm, Y. Takeda, B.G. Andersson, and R. Carlström. Solid State Sintered 3-D Printing Component by Using Inkjet (Binder) Method. *Journal of the Japan Society of Powder and Powder Metallurgy*, 63(7):421–426, 2016.

[87] G.C. Kuczynski. Self-diffusion in sintering of metallic particles. *Journal of Metals*, 1(2):169–178, 1949.

[88] J.G.R. Rockland. The Determination of the Mechanism of Sintering. *Acta Metallurgica*, 15(1), 1967.

[89] Y.I. Frenkel. Viscous flow of crystalline bodies under the action of surface tension. *Journal of Physics*, 9(5):385–391, 1945.

[90] D.R.H. Jones and M.F. Ashby. *Engineering Materials 1: An Introduction to Properties, Applications and Design*. Butterworth-Heinemann, Oxford, UK, 5th edition, 2019.

[91] J.D. Hansen, R.P. Rusin, M.H. Teng, and D.L. Johnson. Combined-Stage Sintering Model. *Journal of the American Ceramic Society*, 75(5):1129–1135, 1992.

[92] Y. Liu, R. Tandon, and R.M. German. Modeling of supersolidus liquid phase sintering: I. Capillary force. *Metallurgical and Materials Transactions A*, 26(9):2415–2422, 1995.

[93] R.M. German. Supersolidus Liquid Phase Sintering Part I: Process Review. *International Journal of Powder Metallurgy*, 26(1), 1990.

[94] J. Liu, A. Lal, and R.M. German. Densification and shape retention in supersolidus liquid phase sintering. *Acta Materialia*, 47(18):4615–4626, 1999.

[95] D.C. Blaine, S Park, and RM German. Master sintering curve for a two-phase material. In *Proceedings of the 4th International Conference on Science, Technology and Applications of Sintering*, pages 268–271. INPG Grenoble, France, 2005.

[96] D.C. Blaine, J.D. Gurosik, S.J. Park, R.M. German, and D.F. Heaney. Master sintering curve concepts as applied to the sintering of molybdenum. *Metallurgical and materials transactions A*, 37(3):715–720, 2006.

[97] D.C. Blaine, S.J. Park, R.M. German, and P. Suri. Application of work-of-sintering concepts in powder metals. *Metallurgical and Materials Transactions A*, 37(9):2827–2835, 2006.

[98] D.L. Johnson. Finding and utilizing the master sintering curve. *Third International Conference on Science, Technology and Applications of Sintering*, 2003.

[99] M.H. Teng, Y.C. Lai, and Y.T. Chen. Computer Program of Master Sintering Modeling to Accurately Predict Sintering Results. 2(2):171–180, 2002.

[100] D.Y. Park, S.W. Lee, S.J. Park, Y.S. Kwon, and I. Otsuka. Effects of particle sizes on sintering behavior of 316l stainless steel powder. *Metallurgical and Materials Transactions A*, 44(3):1508–1518, 2012.

[101] P. Garg, S.J. Park, and R.M. German. Effect of die compaction pressure on densification behavior of molybdenum powders. *International Journal of Refractory Metals and Hard Materials*, 25(1):16–24, 2007.

[102] K. An. Pressure assisted master sintering surface of Co, Cu and Fe powder mixture. *Powder Technology*, 234:117–122, 2013.

[103] K. Inaekyan, V. Paserin, I. Bailon-Poujol, and V. Brailovski. Presented at the AMPM 2016 conference on Additive Manufacturing. *AMPM2016 Conf. Addit.Manuf., Boston, USA*, (June):4–6, 2016.

[104] J.A. Bas, J.A. Calero, and M.J. Dougan. Sintered soft magnetic materials. properties and applications. *Journal of Magnetism and Magnetic Materials*, 254:391–398, 2003.

[105] A. Rogalsky, I. Rishmawi, L. Brock, and M. Vlasea. Low cost irregular feed stock for laser powder bed fusion. *Journal of Manufacturing Processes*, 35:446–456, 2018.

[106] B. Dou, V. Dupont, P.T. Williams, H. Chen, and Y. Ding. Thermogravimetric kinetics of crude glycerol. *Bioresource Technology*, 100(9):2613–2620, 2009.

[107] A.W.L. Yao and Y.C. Tseng. A robust process optimization for a powder type rapid prototyper. *Rapid Prototyping Journal*, 8(3):180–189, 2002.

[108] D. Godlinski and S. Morvan. Steel parts with tailored material gradients by 3d-printing using nano-particulate ink. In *Materials Science Forum*, volume 492, pages 679–684. Trans Tech Publ, 2005.

[109] D. Gerada, N.L. Mebarki, A.and Brown, C. Gerada, A. Cavagnino, and A. Boglietti. High-speed electrical machines: Technologies, trends, and developments. *IEEE Transactions on Industrial Electronics*, 61(6):2946–2959, 2014.

[110] M. Garibaldi, I. Ashcroft, M. Simonelli, and R. Hague. Metallurgy of high-silicon steel parts produced using selective laser melting. *Acta Materialia*, 110:207–216, 2016.

APPENDICES

Appendix A

Table of Parameters

Pre-Process	Process	Post-Process	Product / Print Property
Powder	**Powder Deposition**	**Curing**	**Product**
Morphology (Sphericity)	Layer Thickness	Drying Time	Green Density
PSD	Powder Deposition Rate (Expandable)	Heating Rate	Sintered / Final Density
Surface Area	Linear Spreading Speed	Curing Peak Temperature	Mechanical Properties (Expandable)
Tap Density	Rotational Spreading Speed	Curing Time Schedule (Expandable)	Other Funcional Properties - Biomedical, Electrical, etc. (Expandable)
Flowability	Spreader Characteristics (Expandable)	De-Powdering	Surface Quality
Wettability			Dimensional Accuracy
Compressibility	**Binder Deposition**	**Debinding**	Repeatability (Expandabe)
Internal Porosity	Binder Saturation	Heating Rate	
Chemistry	Binder Jetting Speed (Expandable)	Debinding Peak Temperature	**Print (Expandable)**
Surface Coatings	Binder Set Time	Debinding Time Schedule (Expandable)	Product / Production Cost
Additives (Expandable)	Binder Bleed Reduction	Debinding Atmosphere / Environment	Production Time
Binder (Liquid)	**Other**	**Sintering**	
Viscosity	Print Orientation (Expandable)	Heating Rate	
Wettability	Print Bed Temperature	Sintering Peak Temperature	
Surface Tension		Sintering Time Schedule (Expandable)	
Adhesion Strength		Sintering Atmosphere	
		Cooling Rate	
Binder (Solid)		Sintering Aids (Expandable)	
Chemistry		External Pressure	
PSD			
Morphology (Sphericity)		**Post-Sintering (Expandable)**	
Blend Weight Fraction		Hot Isostatic Pressing (Expandable)	
Wettability		Infiltration (Expandable)	
Surface Area		Surface Treatments (Expandable)	
Design Features (Expandable)			
Thin Feature Dimensions (x, y, z, theta)			
Overhang Dimensions (x,y,z, theta)			
Hole Dimensions (x,y,z, theta)			
Feature Curvature			
Surface Curvature			
Embedded Structures			

Appendix B

Green Sample Analytics

Fe Dataset - Regression

Table B.1: ANOVA table for the effects of process parameters on green density; L: layer thickness; B: binder volume; C: compaction.

Variable	Sum of Sq.	Deg. of Freedom	F	PR(>F)
Intercept	81.482696	1.0	7.833502	9.023760e-03
L	124.595993	1.0	11.978285	1.688873e-03
B	178.620333	1.0	17.172023	2.702992e-04
C	444.296662	1.0	42.713349	3.706958e-07
L:B	50.341927	1.0	4.839722	3.593170e-02
L:C	233.382572	1.0	22.436701	5.270526e-05
B:C	240.640976	1.0	23.134502	4.302659e-05
Residual	301.652841	29.0	NaN	NaN

Table B.2: OLS regression table for the process parameters and green density values; L: layer thickness; B: binder volume; C: compaction.

Dep. Variable:		Density		R^2:		0.913
Model:		OLS		Adj. R^2:		0.895
Method:		Least Squares		F-stat.:		50.99
No. Obs.:		36		Prob(F):		4.23e-14
Df Resid.:		29		Log-Lkhd:		-89.345
Df Model:		6		AIC:		192.7
Cov. Type:		Non-robust		BIC:		203.8
Variable	Coef	Std Err	t	P>t	[0.025	0.975]
Intercept	-35.5853	12.714	-2.799	0.009	-61.589	-9.582
L	0.3995	0.115	3.461	0.002	0.163	0.636
B	0.5522	0.133	4.144	0.000	0.280	0.825
C	77.4527	11.851	6.536	0.000	53.215	101.691
L:B	-0.0031	0.001	-2.200	0.036	-0.006	-0.000
L:C	-0.3558	0.075	-4.737	0.000	-0.509	-0.202
B:C	-0.3122	0.065	-4.810	0.000	-0.445	-0.179
OB:		0.130		DW:		1.031
Prob(OB):		0.937		JB:		0.223
Skew:		0.129		Prob(JB):		0.894
Kurtosis:		2.712		Cond. No.:		2.17e+05

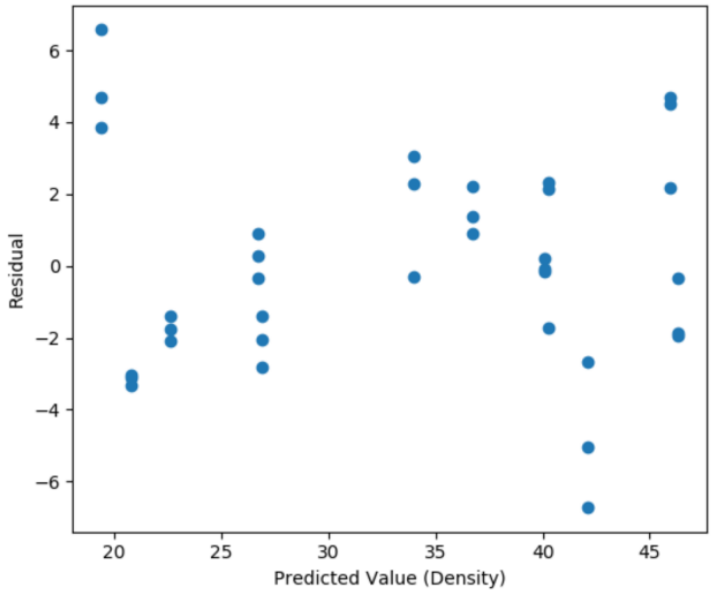


Figure B.1: Residuals plot of the regression model for Fe.

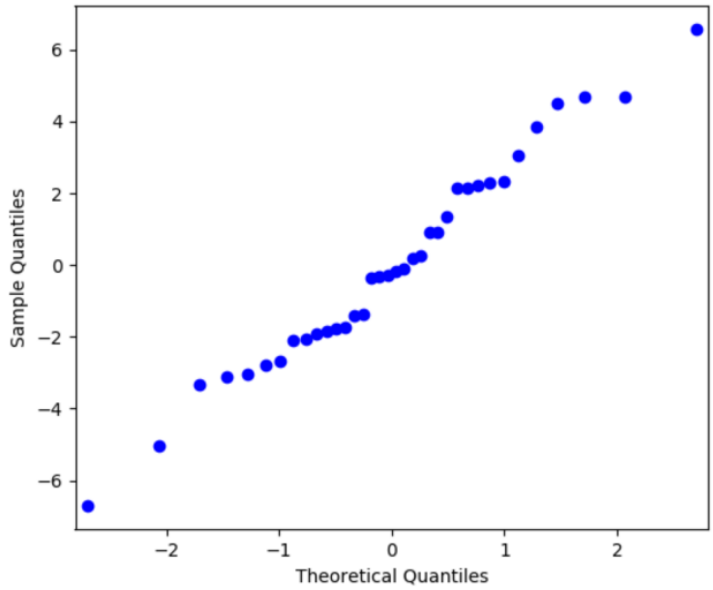


Figure B.2: Q-Q plot of the regression model for Fe.

Fe-Si Dataset - Green Density Plots

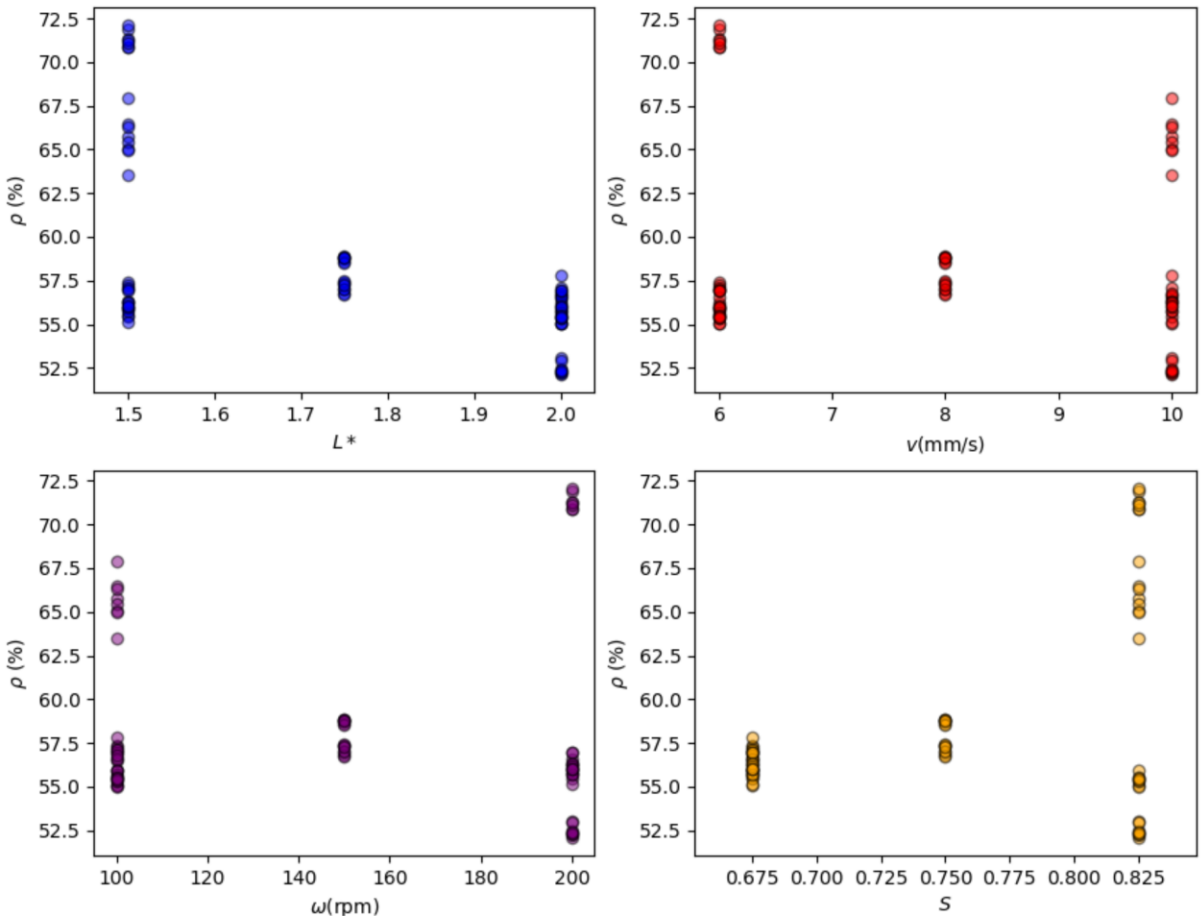


Figure B.3: Individual plots of green density against printing parameters for Fe-Si.

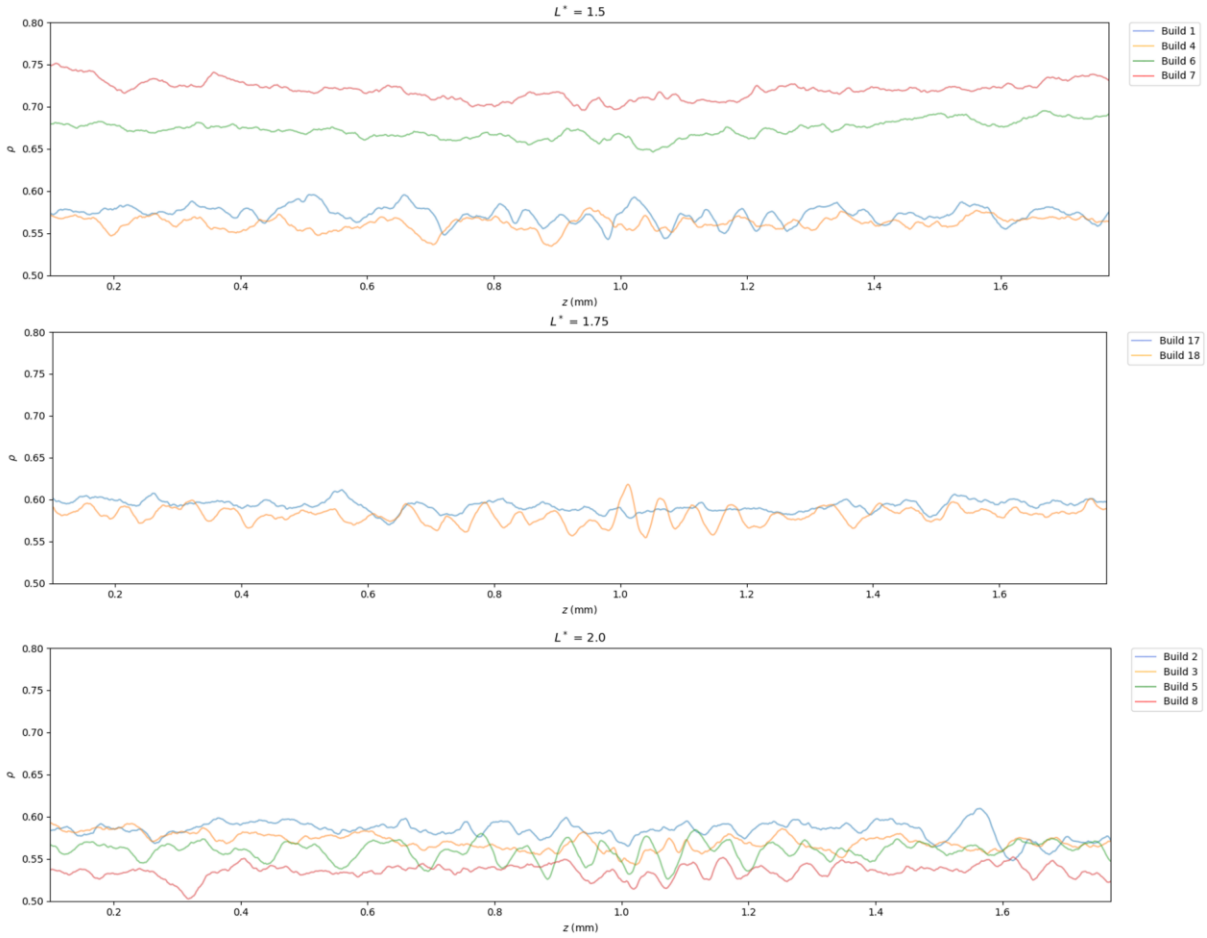


Figure B.4: Density profiles in the z-direction of green samples from various builds for Fe-Si.

Fe-Si Dataset - Regression

Table B.3: ANOVA table for the effects of process parameters on green density; l: normalized layer thickness; v: spreading speed; w: compaction speed; s: binder saturation.

Variable	Sum of Sq.	Deg. of Freedom	F	PR(>F)
Intercept	36.977734	1.0	55.689191	1.779600e-10
l	118.193953	1.0	178.002404	6.606764e-21
v	41.483034	1.0	62.474259	2.743869e-11
w	5.309539	1.0	7.996269	6.107864e-03
s	93.545275	1.0	140.881012	1.993442e-18
l:v	12.582275	1.0	18.949151	4.488141e-05
l:w	10.017414	1.0	15.086421	2.302699e-04
l:s	0.132810	1.0	0.200014	6.560906e-01
v:w	837.269387	1.0	1260.944059	1.667540e-46
v:s	1.897336	1.0	2.857424	9.540181e-02
w:s	18.864516	1.0	28.410329	1.137200e-06
Residual	46.480141	70.0	NaN	NaN

Table B.4: OLS regression table for the process parameters and green density values; l: normalized layer thickness; v: spreading speed; w: compaction speed; s: binder saturation.

Dep. Variable:		Density		R^2:		0.978
Model:		OLS		Adj. R^2:		0.976
Method:		Least Squares		F-stat.:		448.0
No. Obs.:		78		Prob(F):		1.72e-55
Df Resid. :		70		Log-Lkhd:		-90.488
Df Model:		7		AIC:		197.0
Cov. Type:		Non-robust		BIC:		215.8
Variable	Coef	Std Err	t	P>t	[0.025	0.975]
Intercept	8.3129	1.114	7.463	0.000	6.091	10.535
l	4.7237	0.354	13.342	0.000	4.018	5.430
v	8.1254	1.028	7.904	0.000	6.075	10.176
w	0.1982	0.070	2.828	0.006	0.058	0.338
s	3.0759	0.259	11.869	0.000	2.559	3.593
l:v	-1.1786	0.271	-4.353	0.000	-1.719	-0.639
l:w	-0.0631	0.016	-3.884	0.000	-0.096	-0.031
l:s	-0.3435	0.768	-0.447	0.656	-1.875	1.188
v:w	-0.0367	0.001	-35.510	0.000	-0.039	-0.035
v:s	-1.4981	0.886	-1.690	0.095	-3.266	0.269
w:s	0.2802	0.053	5.330	0.000	0.175	0.385
OB:		6.072		DW:		1.376
Prob(OB):		0.048		JB:		6.028
Skew:		-0.432		Prob(JB):		0.0491
Kurtosis:		4.053		Cond. No.:		1.58e+019

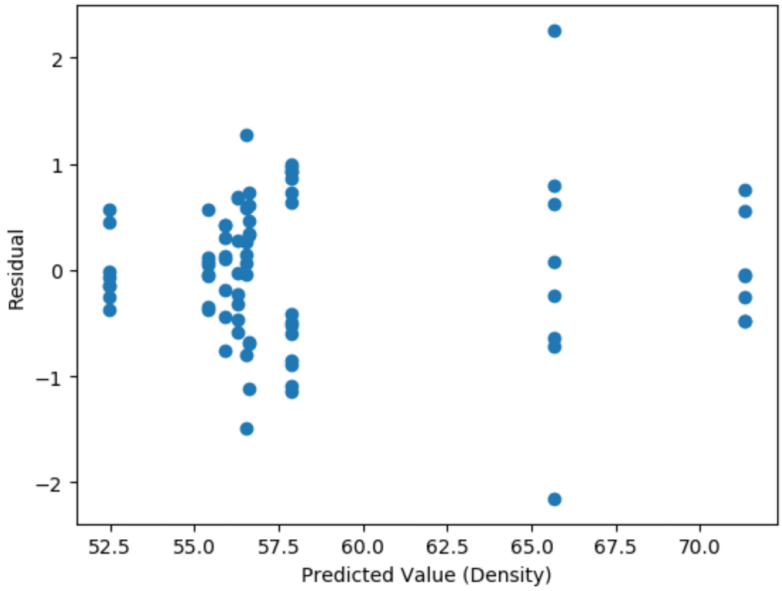


Figure B.5: Residuals plot of the regression model for Fe-Si.

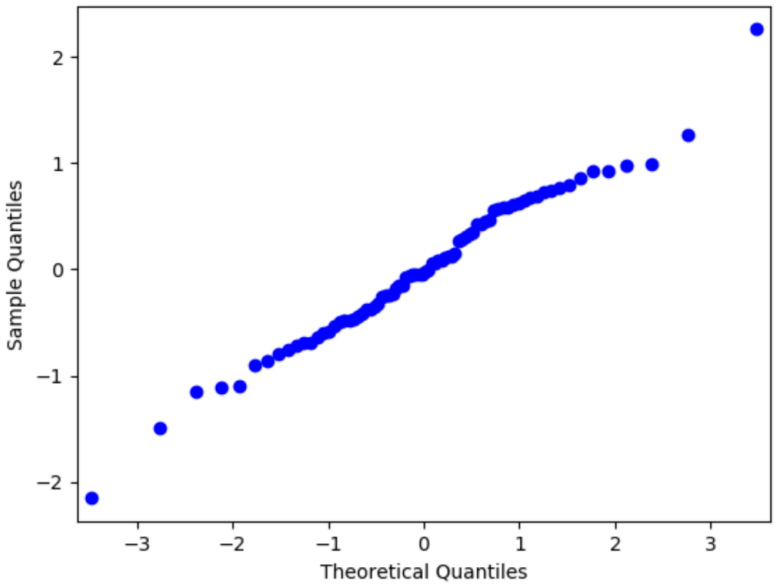


Figure B.6: Q-Q plot of the regression model for Fe-Si.

Fe-Si Dataset - Optimization Equations

$$\frac{\partial \rho}{\partial L^*} = 0 = 4.7237 - 1.1786v - 0.0631\omega \tag{B.1}$$

$$\frac{\partial \rho}{\partial v} = 0 = 8.1254 - 1.1786L^* - 0.0367\omega \tag{B.2}$$

$$\frac{\partial \rho}{\partial \omega} = 0 = 0.1982 - 0.0631L^* - 0.0367v + 0.2802S \tag{B.3}$$

$$\frac{\partial \rho}{\partial S} = 0 = 3.0759 + 0.2802\omega \tag{B.4}$$

Appendix C

Sintered Sample Images

Fe Dataset - SEM

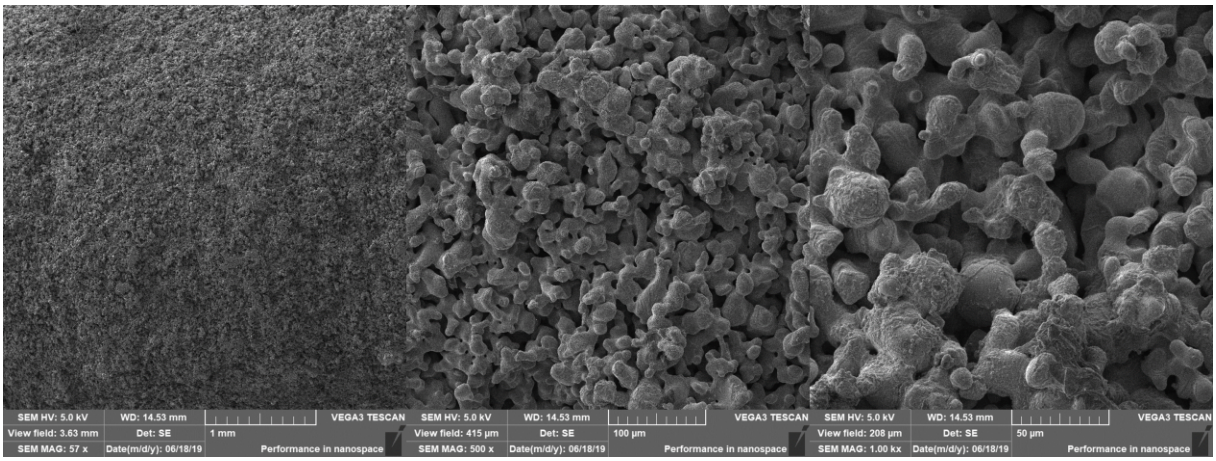


Figure C.1: SEM images of Fe sample A, taken at the sample surface, sintered at 1390°C for 2 hours.

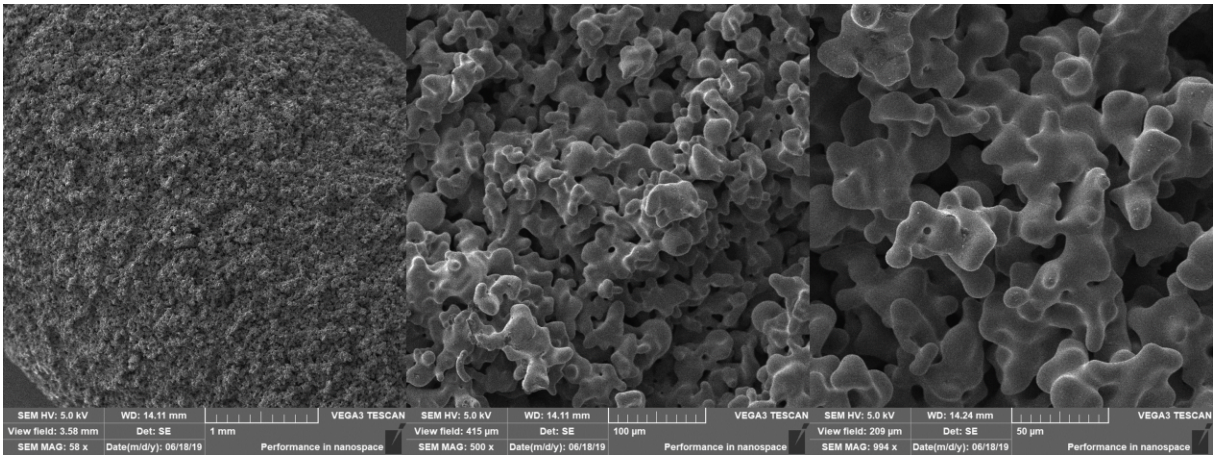


Figure C.2: SEM images of Fe sample A, taken at the sample surface, sintered at 1390°C for 6 hours.

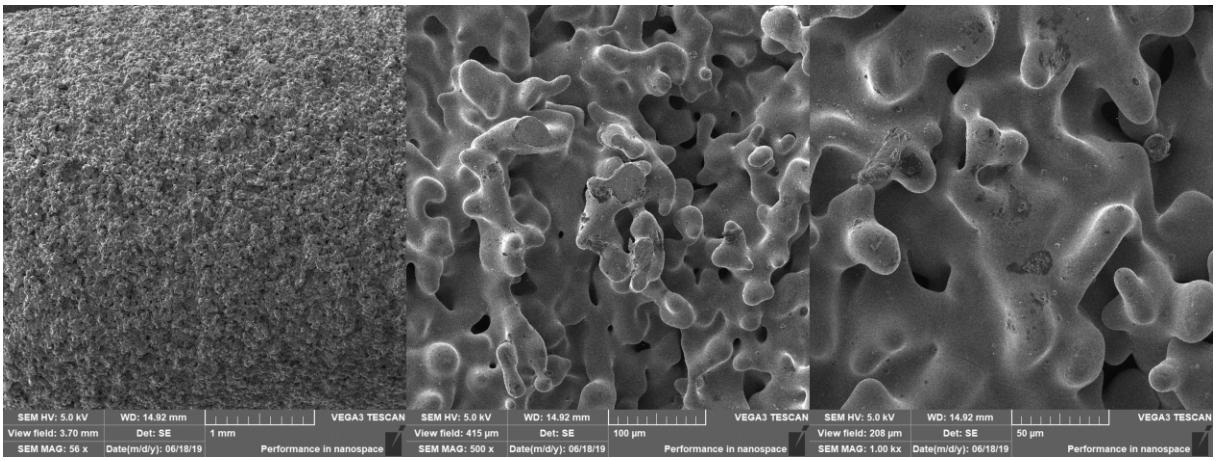


Figure C.3: SEM images of Fe sample A, taken at the sample surface, sintered at 1490°C for 2 hours.

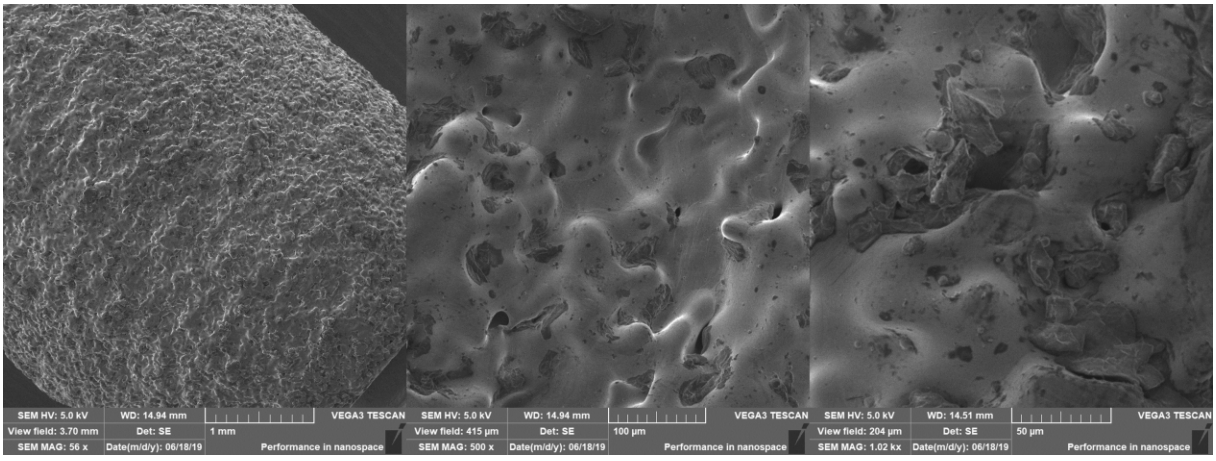


Figure C.4: SEM images of Fe sample A, taken at the sample surface, sintered at 1490°C for 6 hours.

Fe-Si Dataset - LCM

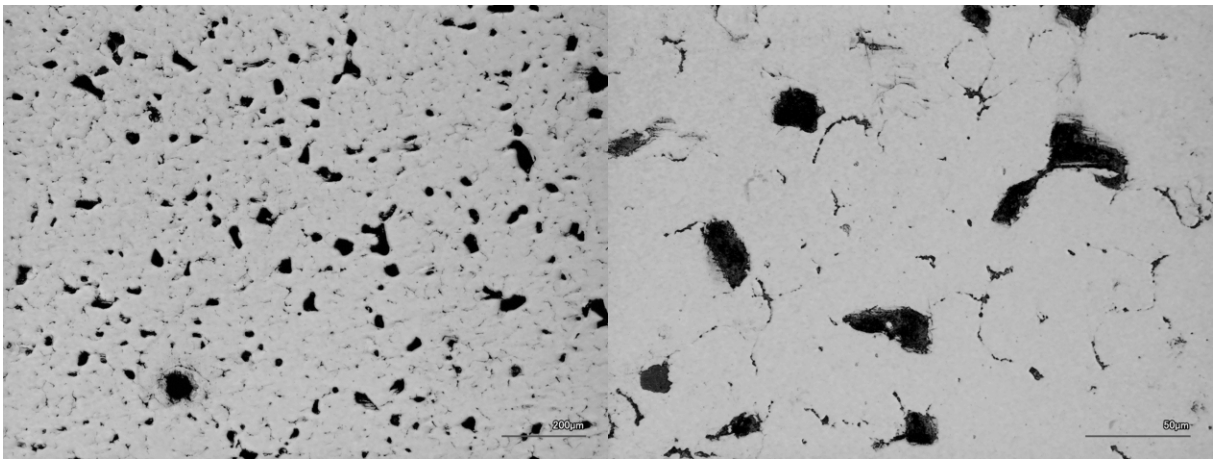


Figure C.5: LCM images of a Fe-Si sample from build 7, sintered at 1470°C for 15 minutes.



Figure C.6: LCM images of a Fe-Si sample from build 7, sintered at 1470°C for 1 hour.

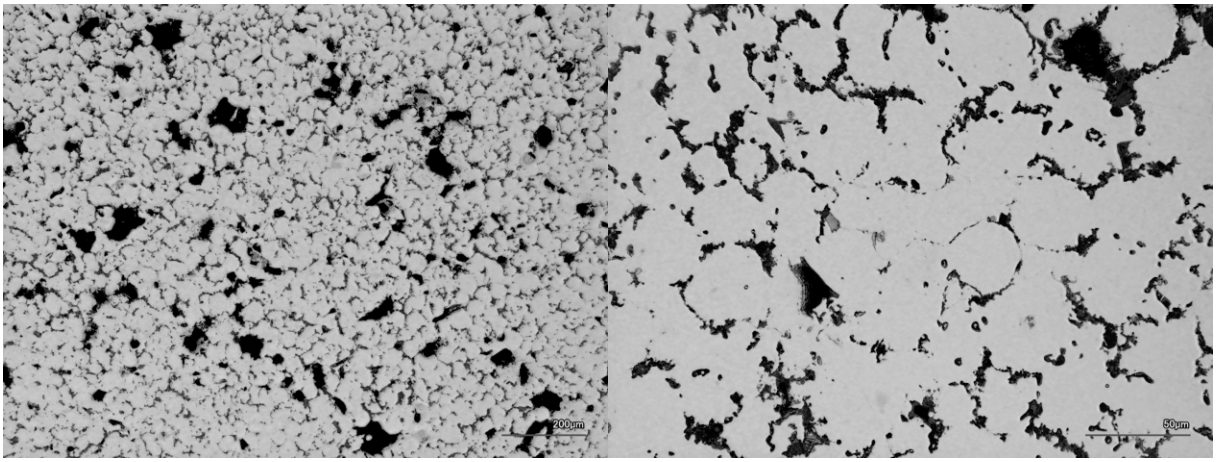


Figure C.7: LCM images of a Fe-Si sample from build 7, sintered at 1482°C for 1 hour.

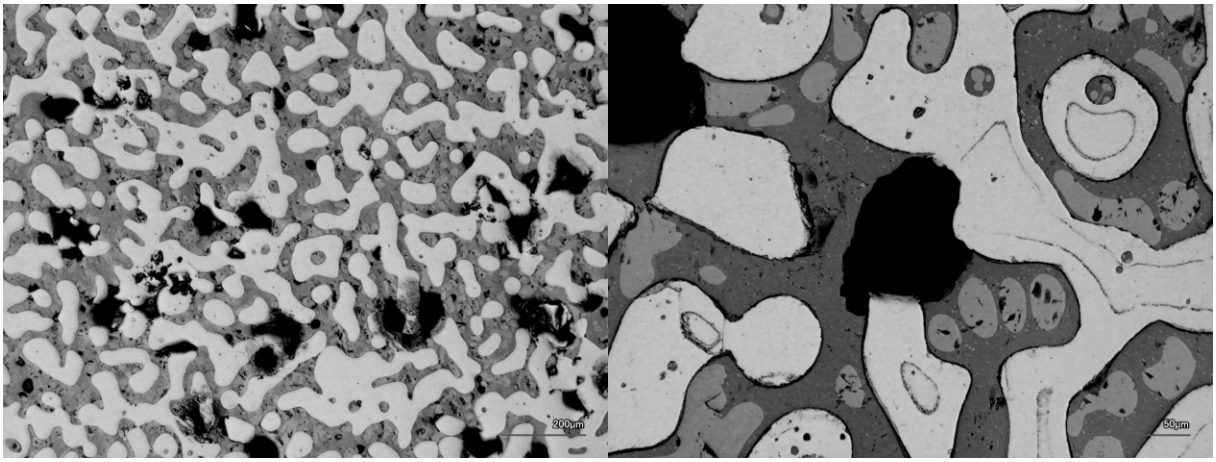


Figure C.8: LCM images of a Fe-Si "anomaly" sample with severe Si segregation, sintered at 1470°C for 1 hour.

Fe-Si Dataset - CT

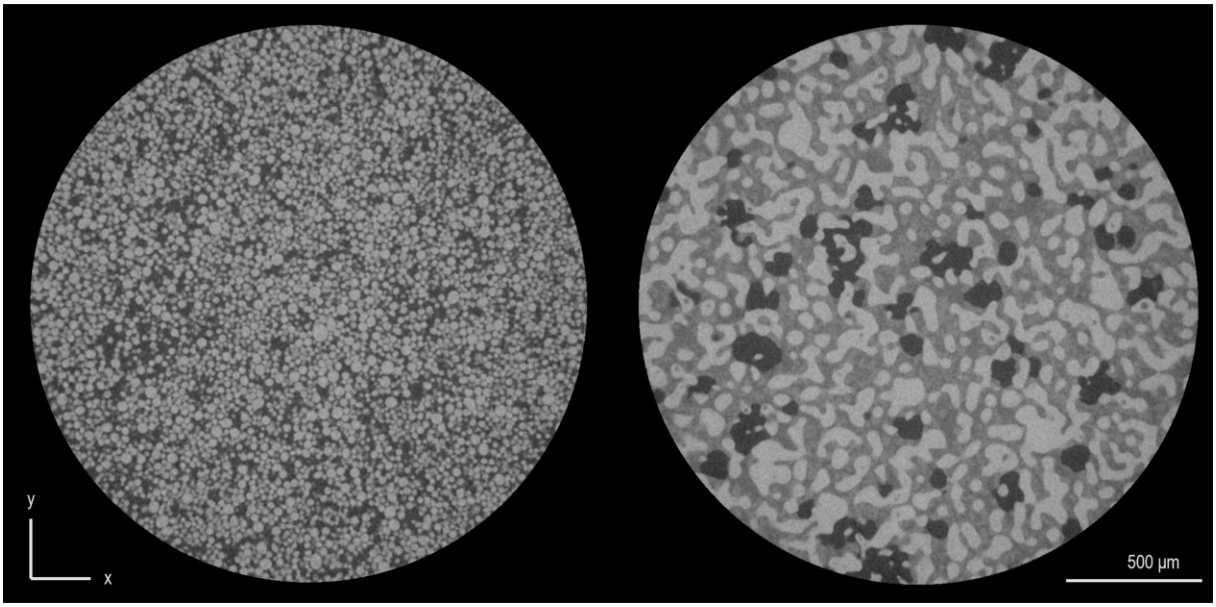


Figure C.9: CT images in the xy plane of the Fe-Si "anomaly" sample from build 7 before and after sintering; the sintered sample showed severe Si segregation.

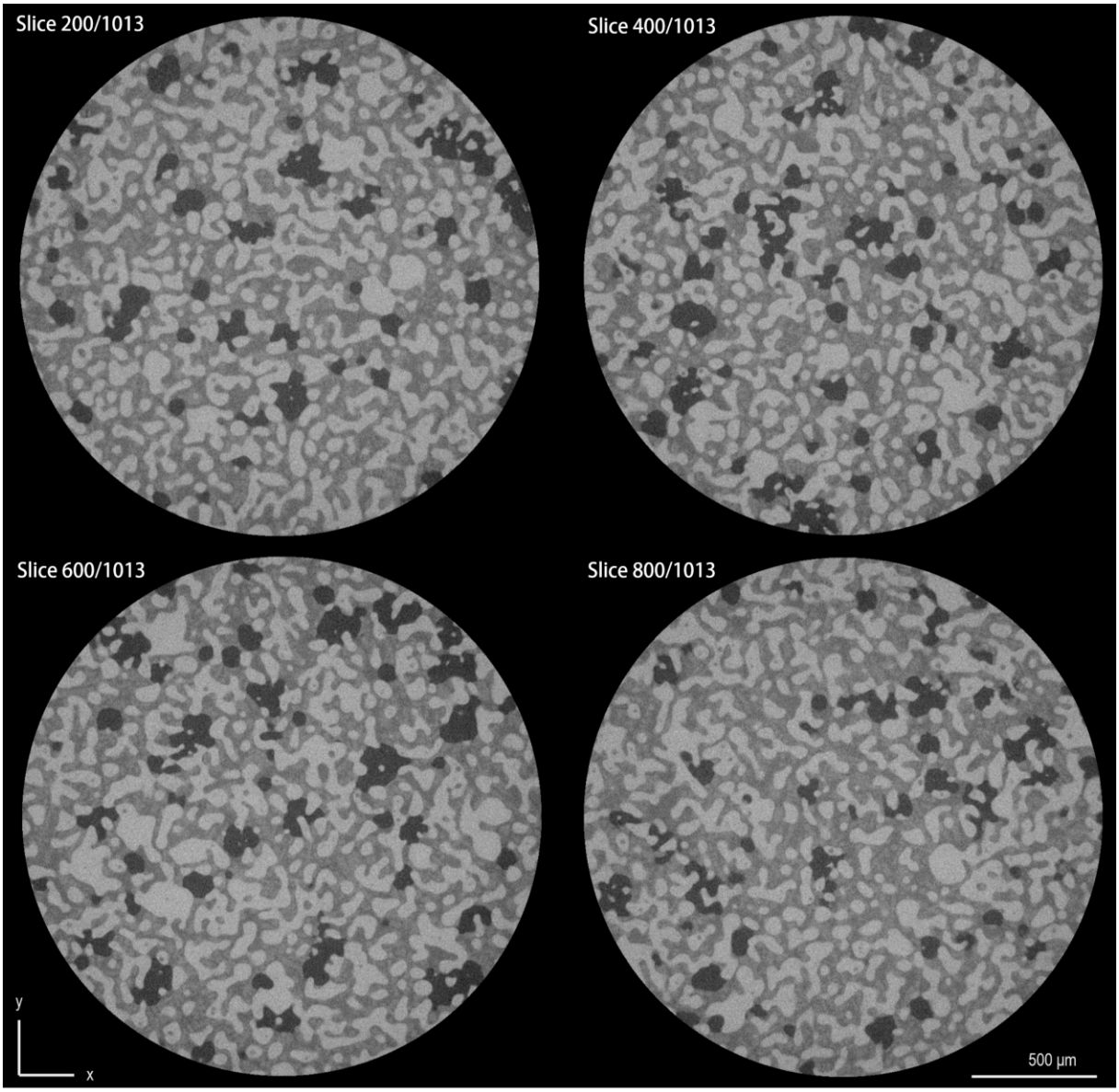


Figure C.10: CT images in the xy plane of the Fe-Si "anomaly" sintered sample from build 7, showing various slices from the reconstructed volume.

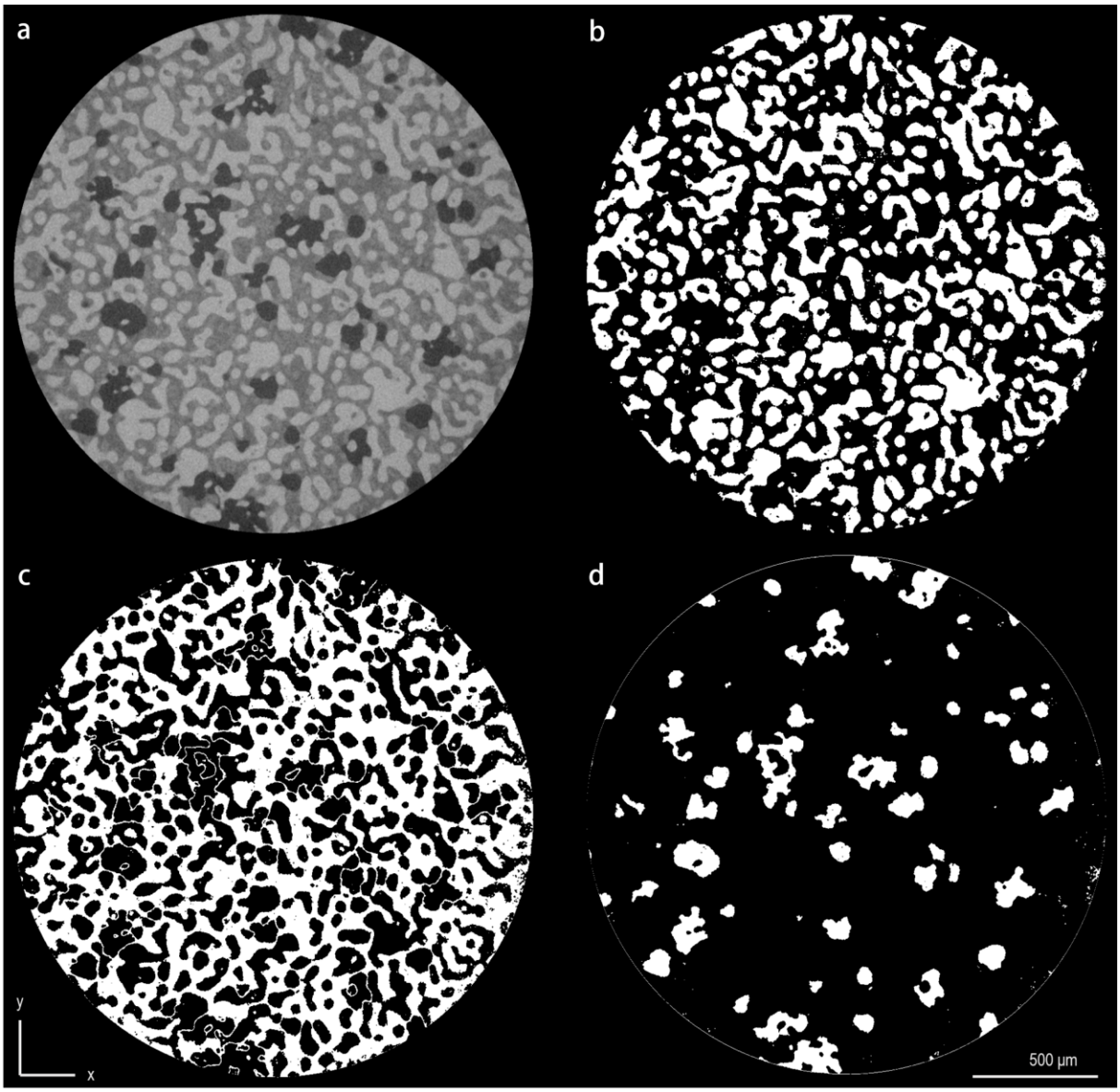


Figure C.11: CT images in the xy plane of the Fe-Si "anomaly" sample from build 7 with image segmentation to corresponding to the three intensity peaks: the Fe segment, the Si segment and the pores segment. Later analysis revealed inaccuracies in the Si and pores intensity peaks.

Fe-Si Dataset - SEM

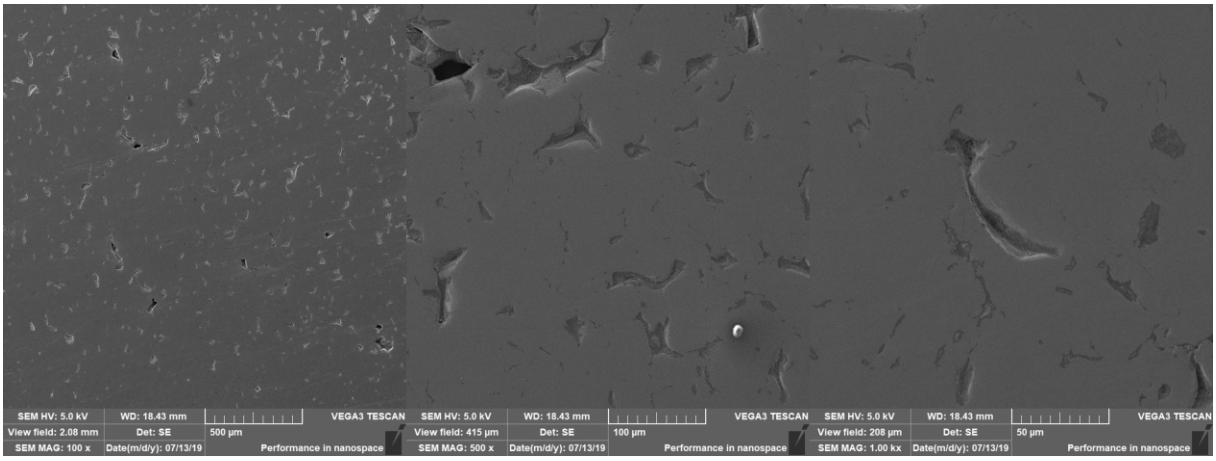


Figure C.12: SEM images of a Fe-Si sample from build 7, sintered at 1470°C for 15 minutes.

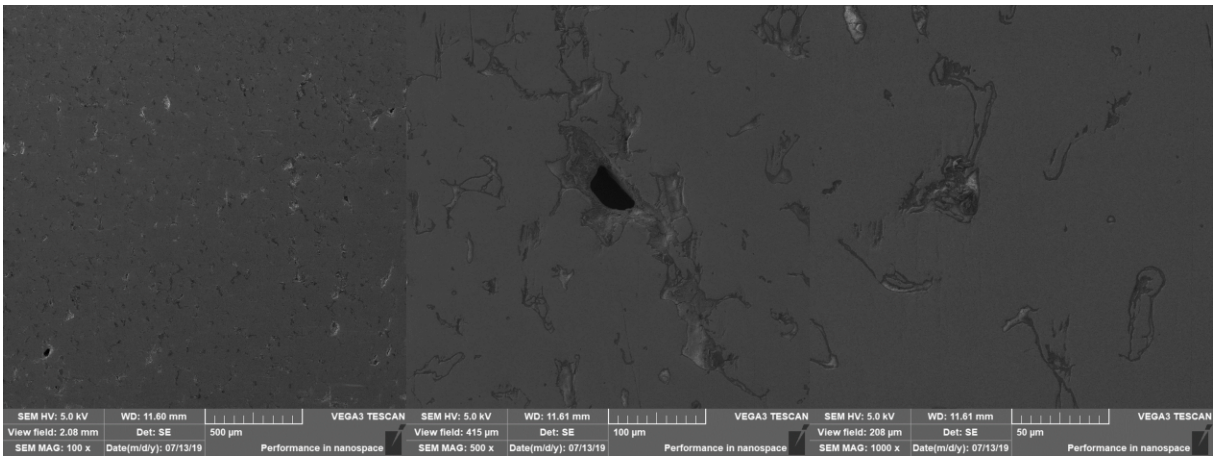


Figure C.13: SEM images of a Fe-Si sample from build 7, sintered at 1470°C for 1 hour.

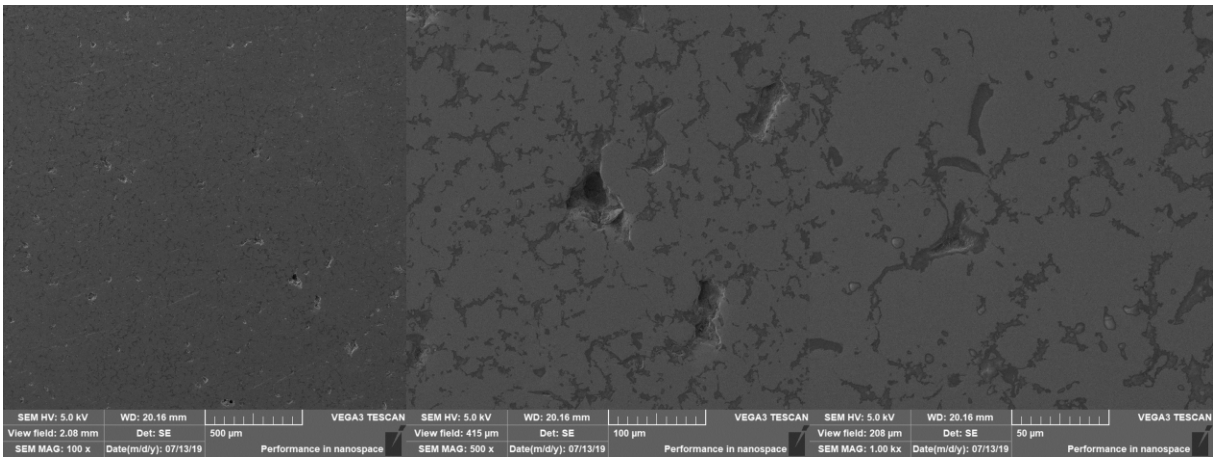


Figure C.14: SEM images of a Fe-Si sample from build 7, sintered at 1482°C for 1 hour.

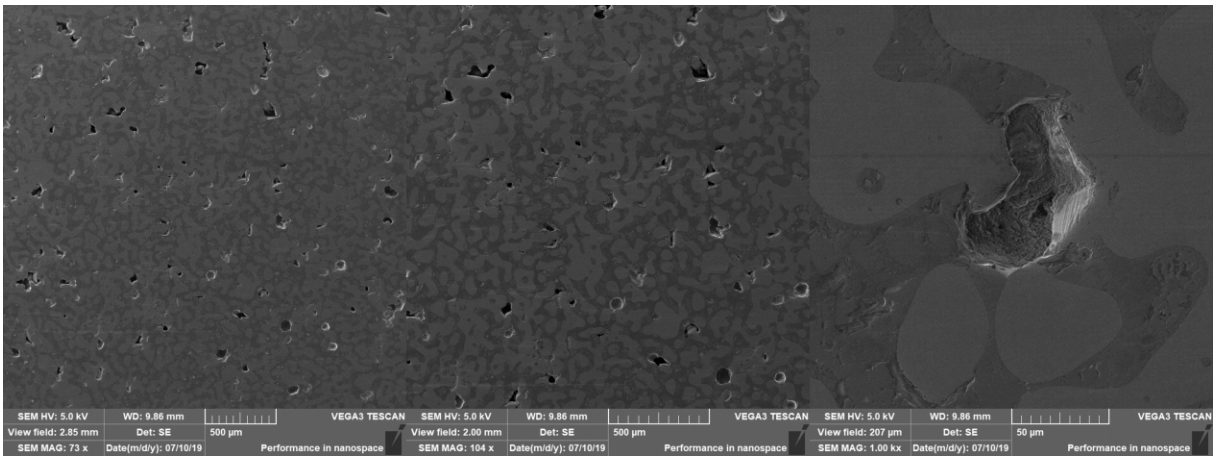


Figure C.15: SEM images of a Fe-Si "anomaly" sample with severe Si segregation, sintered at 1470°C for 1 hour.